Article

Loss and Isotopic Fractionation of Alkali Elements during Diffusion-Limited Evaporation from Molten Silicate: Theory and Experiments

Zhe J. Zhang,* Nicole Xike Nie,▽ Ruslan A. Mendybaev,▽ Ming-Chang Liu, Justin Jingya Hu, Timo Hopp, Esen E. Alp, Barbara Lavina, Emma S. Bullock, Kevin D. McKeegan, and Nicolas Dauphas

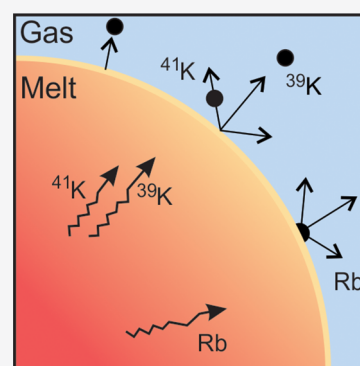Read Online

ACCESS | Metrics & More | Article Recommendations | Supporting Information

ABSTRACT: Moderately volatile elements (MVEs) are variably depleted in planetary bodies, reflecting the imprints of nebular and planetary processes. Among MVEs, Na, K, and Rb are excellent tracers for unraveling the history of MVE depletion in planetary bodies because they have similar geochemical behaviors but can be chemically fractionated by evaporation and condensation processes. Furthermore, K and Rb are amenable to high-precision isotopic analyses, which can help constrain the conditions of evaporation and condensation. To quantitatively understand why Na, K, and Rb are depleted in planetary bodies, we have carried out vacuum evaporation experiments from basaltic melt at 1200 and 1400 °C to study their evaporation kinetics and isotopic fractionations. We chose this composition because it is relevant to evaporation from small differentiated planetesimals. The Rb isotopic compositions of the evaporation residues were measured by multicollector inductively coupled plasma mass spectrometry (MC-ICPMS), and the K isotopic compositions were measured along profiles across the residues by secondary ion mass spectrometry (SIMS). In the 1400 °C run products, we found that the concentrations of both K and Rb in the run products decreased from core to rim, which was accompanied by a heavy K isotope enrichment near the surface. This indicates that, in this run, evaporation was limited by diffusion. To use those data quantitatively, we derive analytical equations that describe the evaporation rate and isotopic fractionation associated with diffusion-limited evaporation from a sphere, slab, and cylinder in transient and quasi-steady state regimes. This model is used to tease out the roles that diffusive transport in the melt and evaporation at the melt/gas interface play in setting the elemental depletion and isotopic composition of the residue. Under our experimental conditions, volatility decreases in the order of Na, Rb, and K. Using our experimental results in a thermodynamic model, we have estimated the product $\gamma\Gamma$ of activity coefficients × evaporation coefficients of Na, Rb, and K. The measured isotopic compositions of the residues are well explained using Rayleigh distillations, whereby the relative volatilities of K and Rb isotopes are given by the square root of their masses. We use our results and previously published data to predict how K and Rb could have been lost as a function of temperature, melt composition, oxygen fugacity, and saturation degree relevant to Vesta's building blocks. We find that the K and Rb depletions, K/Rb elemental fractionation, and $\delta^{41}K$ and $\delta^{87}Rb$ isotopic fractionations of Vesta (as sampled by howardite-eucrite-diogenite (HED) meteorites) are best explained by evaporation of submillimeter size objects for 0.1−10 years at moderate temperatures (∼1050 °C) in a medium ∼98.8% saturated.

KEYWORDS: diffusion, evaporation, K, Rb, isotope fractionation, Vesta

1. INTRODUCTION

Moderately volatile elements (MVEs) are elements with 50% condensation temperatures between ∼390 and 1060 °C under solar nebula conditions.[1,2] These elements are found to be variably depleted in planetary bodies relative to solar composition as defined by CI chondrites.[3,4] This depletion could have taken place (i) in the solar nebula, reflecting its global thermal evolution or more local events,[5−13] or (ii) during planetary accretion through impacts or magma ocean degassing.[14−22]

Potassium (K) and rubidium (Rb) are particularly well suited for tracing the origin of the depletion in MVEs of planetary bodies (asteroids, moons, and planets) and some of their nebular constituents (chondrules) because (i) they have

relatively low 50% condensation temperatures of 733 °C for K and 527 °C for Rb in solar nebula conditions,[1,2] (ii) they both are strong lithophile elements,[22,23] meaning that they partition quantitatively into silicate during core formation, and (iii) they are both highly incompatible elements, so measurement of crustal rocks such as basalts provides a good estimate of the bulk composition of a planetary body. Potassium and rubidium

belong to the group of alkali elements, which comprises several lithophile elements that span a wide range of 50% condensation temperatures: Li (869 °C), Na (685 °C), K (733 °C), Rb (527 °C), Cs (526 °C), and short-lived radioactive Fr (with a half-life of 22 min, ^{223}Fr is the longest-lived isotope of Fr).[1,2] The relative abundances of alkali elements can provide insights into volatile element depletion in planetary bodies.[4,23−25] Significant uncertainties remain, however, with regard to the relative volatilities of these alkali elements,[26−34] the roles played by evaporation and condensation, and whether thermodynamic equilibrium prevailed when these elements were depleted. The latter point can be resolved by measuring isotopic fractionation as evaporation and condensation produce opposite isotopic fractionations that are modulated by the saturation of the surrounding medium.[5,35−37]

In the present contribution, we focus on isotopic fractionation of K and Rb and the kinetics of Na, K, and Rb loss during evaporation. Potassium and rubidium are the two most volatile multi-isotope alkali elements, and they have very similar geochemical behaviors, which facilitates interpretations. Potassium isotope systematics are receiving increasing attention in both low and high temperature geochemistry.[17,38−65] Rubidium isotopic variations have received less attention, not because of lack of scientific interest but because the abundance of Rb is much lower than that of K, which makes it more difficult to analyze its isotopic composition. Several recent studies have shown that Rb isotopic composition could be measured with sufficient precision to detect isotopic variations in natural materials,[17,66,67] and Rb equilibrium isotopic fractionation factors for several minerals have been calculated using density functional theory.[46]

The depletions of K and Rb are usually assessed by normalizing concentrations against those of U and Sr, which are also highly incompatible lithophile elements, but they are highly refractory and are not easily lost by partial evaporation/condensation. CI chondrites have K/U and Rb/Sr weight ratios (e.g., ppm/ppm) of ∼63095 and ∼0.27519, respectively.[2] Most planets and meteorites have K/U and Rb/Sr ratios (both normalized to CI chondrites) that correlate along a slope-one line,[3] meaning that these two elements have similar volatilities, at least to first order. However, in detail, Rb seems to be more depleted in some objects. In particular, howardite-eucrite-diogenite (HED) meteorites (a group of meteorites thought to sample Vesta) have CI-normalized K/U and Rb/Sr ratios of around 0.06 and 0.01, respectively,[68] meaning that Vesta's K/Rb ratio is a factor of ∼6 higher than CI.

Partial evaporation and condensation are the two processes responsible for the fractionation of MVEs in planetary bodies. Carrying out net condensation experiments under well-controlled supersaturated conditions, when the vapor pressure of an element (P_i) is significantly larger than that at equilibrium ($P_{i,eq}$), is challenging. However, one can learn about both evaporation and condensation processes by combining the result of evaporation experiments under low-pressure conditions with independent knowledge of equilibrium vapor pressures of the evaporating species. Indeed, evaporation and condensation are related through the kinetic theory of gases and the Hertz-Knudsen equation to equilibrium thermodynamics.[5,35,36] Evaporation experiments on K and Rb have been performed under a variety of conditions.[26−31] The results of these studies are not all consistent, especially with regard to the relative volatilities of K and Rb, with some studies concluding that the

two elements have similar volatilities[30] while others find that Rb is either more or less volatile than K.[28,31]

Evaporation under low-pressure conditions can also leave its imprint on the isotopic composition of MVEs. This stems from the fact that the light isotopes tend to be more efficiently vaporized than heavy ones.[36,69−72] The degree of fractionation depends on the degree of undersaturation ($P_i < P_{i,eq}$) of the surrounding medium.[5,35,36] Thus, if isotopic fractionation during vacuum evaporation is well calibrated, one can estimate the degree of undersaturation during the evaporation of natural samples on the basis of their measured K and Rb isotopic compositions. For example, the K and Rb isotopic compositions of lunar rocks were used to constrain the degree of undersaturation under which these elements could have been lost from the protolunar disk in the aftermath of the giant impact.[17]

Early studies found uniform potassium isotopic composition in planetary bodies and meteorites, but the isotopic measurements were relatively imprecise.[43,44,55,73−75] These studies only detected K and Rb isotopic variations in lunar soils that presumably reflected vaporization by micrometeorite impact and loss from the lunar exosphere.[44,74,76] More recently, high precision studies found measurable K and Rb isotopic variations in meteorites and planets that can be linked to the depletions in MVEs in these objects. Potassium and rubidium depletions are usually reported relative to CI chondrites. The K and Rb isotopic compositions of chondrites are still uncertain,[52,59,60,66,67] and the bulk silicate Earth provides a more reliable baseline than CI to express K and Rb isotopic fractionations. The Moon is depleted in K and Rb by factors of about 28 and 32, respectively, relative to CI chondrites, and lunar rocks appear to be enriched in the heavy isotopes of K (δ^{41}K up to +0.4 ± 0.05‰[38,51]) and Rb (δ^{87}Rb up to +0.16 ± 0.06‰[66,17]) relative to terrestrial rocks. HED meteorites that are thought to derive from the asteroid Vesta are depleted in K and Rb by factors of ∼17 and 100 relative to CI chondrites, and they are enriched in the heavy isotopes of K and Rb by ∼+0.84‰,[52] and ∼+0.67 to +1.63‰[66] relative to Earth, respectively.

Previous studies have investigated alkali element chemical fractionation either under one-bar or vacuum conditions,[26−32,77] and kinetic isotopic fractionation of potassium from chondritic composition melts in a vacuum.[26,27] As shown by Nie and Dauphas,[17] the characterization of Rb isotopic fractionation during vacuum evaporation is critical for improving our understanding of the origin of MVE depletions in the Moon and other planetary bodies.

In order to develop a quantitative understanding of the depletions and isotopic fractionations of K and Rb in planetary bodies, it is critical to understand their evaporation kinetics as well as the associated isotopic fractionations in both diffusion-free and diffusion-limited regimes. Diffusion, in both the solid/liquid and vapor, can greatly affect evaporation kinetics and isotopic fractionation. Previous work on isotopic fractionation during evaporation in a diffusion-limited regime used numerical models and focused on major elements (e.g., Si, O, Mg), which involves a moving boundary.[35,36,71,78−80] Sossi et al.[81] recently re-evaluated this question for trace elements, also using a numerical model. A good theoretical framework grounded in analytical equations is however still needed to describe evaporation of minor/trace elements in a diffusion-limited regime.

The objectives of the present study are to (i) experimentally characterize the evaporation kinetics of K, Rb, and Na from basaltic melt, (ii) characterize the elemental and isotopic

fractionations of K and Rb during evaporation under low-pressure conditions, and (iii) improve our understanding of diffusion-limited evaporation using an analytical approach apply experimental constraints to natural samples.

2. METHODS

2.1. Sample Preparation. The starting materials for the evaporation experiments were prepared by mixing SiO_2, MgO, $CaCO_3$, TiO_2, Al_2O_3, and FeO powders of >99.9% purity in proportions similar to an average normal mid-ocean ridge basalt (N-MORB) composition[82] that was then doped with extra Na_2CO_3, K_2CO_3, and Rb_2CO_3. This composition is also similar to eucrite (sampled from 4-Vesta) except for a lower FeO content (9.69 vs 17.9 wt %). The rationales for choosing a terrestrial basalt composition are (i) the composition has a relatively low liquidus temperature compared to chondrites, (ii) it is relevant to differentiated planetary bodies, and (iii) thermodynamic models for such silicate melts are relatively well calibrated. The mixture of oxide and carbonate powders was first ground in an agate mortar for at least 1 h under ethanol, dried out, and further homogenized in ethanol in a Retsch MM200 ball mill for at least 5 h. After complete mixing, the sample powder was dried overnight, placed in a platinum crucible, and heated in a muffle furnace at 950 °C for 5 h to decarbonate and dehydrate the starting material. The Pt crucible with the powder was removed from the muffle furnace, cooled, and kept in a desiccator before use. For each individual run, around 25−70 mg of powder mixture was glued using poly(vinyl alcohol) (PVA) on a 2.5 mm diameter iridium wire loop and dried in air at room temperature. The sample loads were then heated at 1000 °C in air for 2 min to remove PVA and water. Each individual sample was then melted at 1200 °C for 5 min in a one-bar gas mixing furnace using a H_2-CO_2 mixture with $\log_{10} fO_2$ set at IW + 2 (two log units above the iron-wüstite buffer; see Mendybaev et al.[83] for details on the calibration of the oxygen sensor). The predicted liquidus temperature of the mixture is ~1203 °C,[84,85] which is close to our experimental temperature of 1200 °C. Based on a scanning electron microscope (SEM) examination of the evaporation residues from 1200 °C experiments (Figure S1), we believe that the samples were completely molten during the runs. Premelting of each individual sample at $\log_{10} fO_2$ = IW + 2 reduced some ferric iron (Fe^{3+}) to ferrous iron (Fe^{2+}), which resulted in a color change of the molten droplets from greenish to completely black. According to thermodynamic calculations using MELTS, a Fe^{3+}/Fe_{total} ratio of ~0.09 is expected under these conditions. We measured the Fe^{3+}/Fe_{total} ratio by Mössbauer spectroscopy in the experimental run products. In the starting glass, we find a value of 0.85, indicating that the 5 min duration was insufficient to equilibrate the oxygen fugacity of the melt with the surrounding gas. The Fe^{3+}/Fe_{total} ratio that we measured corresponds to $\log_{10} fO_2$ = IW + 11.1. A low duration was used to minimize loss (<2%) of alkali elements during this stage. Significant loss of MVEs was however observed when the vacuum furnace temperature was ramped up to the experimental temperature of 1200 or 1400 °C. The surface areas of the quenched glass samples were estimated, assuming an ellipsoid shape with two equal semidiameters, $a = b$, using the approximate equation

$$S \approx 4\pi \sqrt[1.6]{((ab)^{1.6} + (ac)^{1.6} + (bc)^{1.6})/3}$$
$$= 4\pi \sqrt[1.6]{(a^{3.2} + 2(ac)^{1.6})/3}$$

where a, b, and c are half lengths of the principal axes. The value of a is the radius of the iridium loop. The value of c is the length measured perpendicular to the plane of the iridium loop. The lengths of these principal axes and the surface areas are given in Table S1.

2.2. Vacuum Evaporation Experiments. The vacuum evaporation experiments were conducted at the University of Chicago in a vacuum furnace built by Hashimoto,[86] following methods outlined in previous studies.[27,70,87−92] Inside the vacuum chamber, a heating element made of tungsten mesh is mounted vertically. The heater is surrounded by a thermal shield made of seven alternating layers of tungsten and molybdenum to minimize heat loss and to maintain a constant temperature in the vicinity of the sample during the experiments. A premolten sample of known mass and geometry mounted on an Ir wire loop was placed at the center of the heater. The temperature of the furnace was monitored by two $W_{100}/W_{74}Re_{26}$ thermocouples located within one centimeter on two sides of the sample and by a pyrometer that was used occasionally to measure the temperature about 5 mm below the sample. The measured temperatures agreed with each other within 5 °C.

After the sample was loaded into the furnace, the furnace was pumped down to about 10^{-6} mbar. Once the desired vacuum condition was achieved, the furnace was first manually heated to 850 °C and held at this temperature until the pressure inside the furnace dropped to 10^{-6} mbar, after which the programmed heating process started. For 1200 °C runs, the temperature was brought up to 1200 °C from 850 °C at a rate of 40 °C/min and the sample was allowed to evaporate for at least 5 min. For 1400 °C runs, the temperature was first ramped up to 1200 °C and stayed at that temperature for 5 min to let air trapped inside the sample escape, and the furnace temperature was then increased to 1400 °C at a rate of 40 °C/min. To account for the possible elemental and isotopic fractionations of Na, K, and Rb when the furnace temperature was ramped up to 1200 and 1400 °C, "zero-time" samples were prepared. As a "zero-time" sample for the 1200 °C runs, we used a sample that was brought to this temperature following the heating schedule described above, kept at 1200 °C for 5 min, and quenched by cutting the power supply off. As a "zero-time" sample for the 1400 °C runs, we used a sample that was quenched when the furnace temperature reached 1400 °C. The chemical and isotopic compositions of these "zero-time" samples were used as reference compositions when assessing the degree of loss and isotopic fractionation in the evaporation residues. The 1200 °C runs were evaporated for durations of 5 min (zero-time run) and 60, 240, 600, and 2400 min and were labeled as Bas1200C0h, Bas1200C1h, Bas1200C4h, Bas1200C10h, and Bas1200C40h, respectively. The effective duration of the evaporation experiments was relative to the zero-time runs. The 1400 °C runs were evaporated for durations of 0 min (zero-time run) and 15, 30, 60, and 90 min and were labeled as Bas1400C0m, Bas1400C15m, Bas1400C30m, Bas1400C60m, and Bas1400C90m, respectively (Table 1).

After the furnace heater was turned off and the furnace temperature dropped to ~25 °C, the vacuum pumps were turned off; the furnace was vented, and the sample was removed and measured for its surface area. The samples were then cut using a slow-speed saw with a very thin diamond wafering blade (0.15 mm thickness). The position of each sample was carefully adjusted to make sure it was cut through the center. One half was mounted into epoxy, polished carefully, and coated with carbon/gold for SEM, electron microprobe analyzer (EPMA), and

Table 1. Chemical and Isotopic Compositions of Evaporation Residues

sample	T (°C)	time (min)	EPMA (wt %) Na_2O	MgO	CaO	TiO_2	SiO_2	Al_2O_3	FeO	K_2O	Rb_2O	MC-ICPMS Na/Al^a	Rb/Al^a	$\delta'^{87}Rb$ (‰)	95% c.i.	SIMS $\delta'^{41}K$ (‰)	95% c.i.	Fe^{3+}/Fe_{total}
mixed powder												0.210	0.260					
initial glass			2.27	7.09	11.21	1.79	45.94	16.00	10.67	2.49	1.86	0.208	0.259					0.85
Bas1400C0m1	1400	0	1.90	7.11	10.88	1.54	48.89	15.29	10.00	2.50	1.89	0.167	0.233	0.76	0.03	0.9	0.3	0.31
Bas1400C0m2	1400	0	1.82	7.08	10.90	1.58	48.99	15.33	9.98	2.46	1.86	0.163	0.231					0.37
Bas1400C15m	1400	15	0.66	7.38	11.25	1.60	50.31	15.86	10.15	1.63	1.12	0.055	0.137	6.24	0.03	12.2	0.5	
Bas1400C30m	1400	30	0.29	7.45	11.41	1.61	51.20	16.16	10.21	1.19	0.74	0.026	0.097	9.71	0.03	19.9	0.3	
Bas1400C60m	1400	60	0.01	7.61	11.46	1.63	52.55	16.10	10.28	0.28	0.10	0.001	0.021	25.75	0.03	49.0	1.4	
Bas1400C90m	1400	90	b.d.l.^{b}	7.65	11.50	1.65	52.55	16.29	10.30	0.05	b.d.l.	0.001	0.003	43.78	0.05	71.5	2.6	
Bas1200C0h1	1200	0	2.00	6.63	10.88	1.52	47.67	15.24	9.66	2.56	1.98	0.181	0.241	0	0.06	0	0.2	
Bas1200C0h2	1200	0	2.30	6.46	11.09	1.57	49.03	15.41	9.69	2.58	1.87	0.192	0.250					0.43
Bas1200C1h	1200	55	1.99	7.00	10.98	1.55	48.43	15.54	10.05	2.53	1.93	0.173	0.238	0.58	0.04	1.1	0.2	
Bas1200C4h	1200	235	1.08	7.19	10.99	1.57	49.87	15.54	10.05	2.15	1.56	0.088	0.182	3.11	0.06	5.6	0.4	
Bas1200C10h	1200	595	0.69	7.33	11.13	1.59	50.27	15.71	10.17	1.84	1.27	0.059	0.160			9.7	0.2	0.49
Bas1200C40h	1200	2395	0.10	7.61	11.18	1.64	51.61	15.74	10.35	1.09	0.67	0.009	0.088	11.16	0.06	21.8	0.3	0.36

^{a}Weight ratio measured by ICPMS. ^{b}b.d.l. means below detection limits.

secondary ion mass spectrometry (SIMS) analyses. The center of the mounted residues may be slightly offset relative to the center of the sample spheroid, but as discussed above, care was taken to minimize this offset. The other half was cut into two quarters. One quarter was dissolved in acid and analyzed by multicollector inductively coupled plasma mass spectrometry (MC-ICPMS), and the other quarter was ground for Mössbauer analyses.

2.3. Chemical Characterization. The elemental compositions of the evaporation residues were measured by MC-ICPMS at the University of Chicago and by EPMA at the Geophysical Laboratory, Carnegie Institution for Science. The EPMA used a defocused electron beam of 20 μm, accelerating voltage of 15 kV, and beam current of 10 nA. To minimize volatilization during analysis, Na and K were measured first on the spectrometers with a counting time of 10 s for Na and 20 s for K. The other elements (Ca, Si, Fe, Mg, Ti, Al, and Rb) were analyzed for 20 s. Background was corrected by off-peak measurements (10 s on either side of the peak). The following standards were used: an RTP ($RbTiPO_5$) standard for Rb, an orthoclase for K, and basaltic glass (basalt 812) for all other elements. Peak overlap between Rb and Si was corrected by analyzing a Si-free Rb standard (RTP) and by measuring the count rate at the location of the Si peak. A correction factor was then applied to the unknown materials. Standards were measured regularly to check for spectrometer drift, especially for Si, which has a narrow peak. For each evaporation residue, at least two transverse line analyses across the entire sample were performed with 100 μm spacing between adjacent points.

The elemental concentrations of Na, K, and Rb and other major elements in the bulk evaporation residues were also measured by MC-ICPMS. SPEX certified reference materials and Alfa Aesar plasma standard solution were mixed and analyzed as standards. We measured the blank nitric acid solution used for diluting the sample between each sample measurement to correct for the blank contribution. For Na, the blank contributions were all below 2%, except for the most Na-depleted samples Bas1400C60m and Bas1400C90m, where the Na blank represents ∼11% and 15% of Na in these samples, respectively. The Rb blank is very low, representing a contribution of less than 2%. The most depleted sample Bas1400C90m has a Rb signal intensity about 70 times higher than the blank.

Since some evaporation residues analyzed are somewhat chemically heterogeneous (see Section 4.1 for details), the bulk composition of the samples obtained by MC-ICPMS is more representative than the ones obtained by the in situ analyses. However, it is difficult to obtain precise K concentration data by MC-ICPMS due to Ar interferences. To quantify the bulk composition, we therefore combine the two methods by taking the K concentration from EPMA (integrated along a profile by calculating the integral $\int r^2 C(r)\, dr / \int r^2\, dr$, with r being the distance from the center of the quenched glass spherule and C being the K concentration) and taking the Na and Rb concentrations measured by ICPMS. For major elements that can be measured using both methods, the results agree with each other within uncertainty (Figure S2).

2.4. Potassium Isotopic Analyses. Potassium isotopic analyses of the run products from the evaporation experiments were conducted on the CAMECA ims-1290 ion microprobe at UCLA. Samples were mounted in epoxy and polished flat. A 23 keV 3 nA O_2^- primary ion beam, generated by a Hyperion-II plasma source, was used to raster areas of 25 × 25 μm^2 on the

samples, yielding sufficient and stable signals ($^{41}K^+ > 2 \times 10^6$ counts per second) for the simultaneous collection of secondary ions ($^{39}K^+$, $^{40}Ca^+$, and $^{41}K^+$) by three Faraday cups. For the more K-depleted glasses, the primary beam intensity was adjusted to 9 nA to maintain the required signal levels for high precision measurements. Mass resolution ($M/\Delta M$) was set at 7500 (10% peak height) to fully resolve $^{41}K^+$ from $^{40}CaH^+$. The backgrounds of the Faraday cups were measured during 1 min of presputtering and were corrected for. Automated beam centering and mass calibration were performed prior to data acquisition. Each analysis was composed of 20 cycles of 10 s each. The K isotopic compositions of the evaporated residues are expressed relative to the ratio measured in the zero-time run quenched at 1200 °C (Bas1200C0h2)

$$\delta'^{41}K(\text{‰}) = 1000 \times \ln\left[\frac{(^{41}K/^{39}K)_{\text{sample}}}{(^{41}K/^{39}K)_{\text{zero-time run}}}\right]$$

The internal error of the measured $^{41}K/^{39}K$ ratio under the aforementioned analytical setting was <0.2‰ (2σ), and the external reproducibility of 10 spot measurements on a glass was normally ~0.4–0.6‰ (2σ standard deviation). The more depleted samples have larger uncertainties (2σ = 3.4‰ for the Bas1400C60m sample with K_2O ~ 0.3 wt %; 2σ = 8.6‰ for the Bas1400C90m sample with K_2O ~ 0.1 wt %). This relatively poor external error does not hinder our ability to constrain the isotopic fractionation factor imparted by evaporation as the variations in the evaporation residues are large (up to 70‰).

2.5. Rubidium Isotopic Analyses. Rubidium isotopic compositions were analyzed in the Origins Lab at the University of Chicago. The column chemistry for Rb purification follows Nie and Dauphas,[17] albeit with a few simplifications. The evaporation residues were first dissolved in 4 mL of 28 M HF + 2 mL of 15 M HNO_3 in PFA fluoropolymer vials on a hot plate at 130 °C for 5 days. After full dissolution, the sample solutions were converted to nitric acid solutions by repeated evaporation and dissolution in concentrated HNO_3 and were finally dissolved in 4 mL of 1 M HNO_3 for column chemistry. To purify Rb from matrix elements, the samples were loaded on a 20 mL column (14 cm height and 15 mm diameter) containing 15 mL of AG50W-X8 resin (200–400 mesh), and Rb was eluted with 160 mL of 1 M HNO_3 to prepurify Rb from most matrix elements. The second column used the same resin type (AG5W0-X8), but a lower HNO_3 molarity of 0.5 M was used. Rubidium was collected in a 130–360 mL elution volume, which allowed us to further separate Rb from Na and Ti. The Rb isotopic compositions were measured with a Neptune MC-ICPMS at the University of Chicago using the method described by Nie and Dauphas.[17] The sample was injected in the plasma torch using a 100 μL/min nebulizer. Normal H sampler and skimmer cones were used. Isotopes ^{85}Rb and ^{87}Rb were analyzed on Faraday cups L2 and axial (A). The possible interference from Sr was monitored at mass 88 on the H1 cup and corrected for by assuming a constant $^{87}Sr/^{88}Sr$ ratio of 0.085. The analytical uncertainty of Rb isotopic analyses is about ±0.03‰ (95% confidence interval). The Rb isotopic compositions of the evaporation residues are reported relative to the zero-time run quenched at 1200 °C (Bas1200C0h2),

$$\delta'^{87}Rb(\text{‰}) = 1000 \ln\left[\frac{(^{87}Rb/^{85}Rb)_{\text{sample}}}{(^{87}Rb/^{85}Rb)_{\text{zero-time run}}}\right]$$

2.6. Mössbauer Analysis of Fe Redox State. The evaporation residues were measured for their Fe redox state by conventional Mössbauer spectroscopy at the Advanced Photon Source, Argonne National Laboratory. All Mössbauer absorption spectra were collected at room temperature with acquisition times of 1–2 days. The obtained absorption spectra were fitted using a commercial software, providing as outputs the isomer shift, quadrupole splitting, and hyperfine field (Figure S3). The relative Fe^{2+} and Fe^{3+} proportions were determined on the relative areas of doublets and sextet (Figure S4A), and the results are reported in Table 1.

3. THEORETICAL FRAMEWORK

The net evaporative flux from a condensate (solid or liquid) is a balance between the flux of atoms that leave the solid/liquid interface and those that are recondensed. This flux is expressed by the Hertz-Knudsen equation,[36,93–95]

$$J_i = J_{e,i} - J_{c,i} = \frac{n_i \gamma_i (P_{i,\text{eq}} - P_i)}{\sqrt{2\pi M_i RT}} \tag{1}$$

where J_i is the net evaporative flux of component i, $J_{e,i}$ is the evaporative flux, $J_{c,i}$ is the condensation flux, n_i is the number of atoms of i in the gas species containing i (e.g., one for monatomic K), $P_{i,\text{eq}}$ is the equilibrium vapor pressure of i, P_i is the partial vapor pressure above the evaporating surface, M_i is the molar mass of the gas species containing i, R is the gas constant, and T is the absolute temperature in Kelvin. At equilibrium, the evaporative flux $J_{e,i}$ is equal to the condensation flux $J_{c,i}$, meaning that there is no net flux across the surface.

We carried out evaporation experiments in vacuum conditions (free evaporation), meaning that there is no recondensation flux (i.e., P_i = 0 in eq 1). Equilibrium thermodynamics and Knudsen cell mass spectrometry measurements[96–99] indicate that Na_2O, K_2O, and Rb_2O should be mainly vaporized from multicomponent silicate melts as monatomic Na(g), K(g), and Rb(g);[100,101] thus, n_i = 1 in eq 1. Equation 1 then can be simplified as

$$J_i = \frac{\gamma_i P_{i,\text{eq}}}{\sqrt{2\pi M_i RT}} \tag{2}$$

where γ_i is the evaporation coefficient of Na, K, and Rb.

The equilibrium vapor pressure over silicate melts can be estimated using thermodynamic databases or measured directly using Knudsen effusion mass spectrometry. If $P_{i,\text{eq}}$ is accurately known, one can use the measured free evaporation rate J_i from vacuum experiments to calculate the evaporation coefficient γ_i. The evaporation coefficient is a physical parameter that is defined as a ratio of free evaporation and equilibrium fluxes[102] and describes the kinetic energy barrier to evaporation. In liquid metals, the value of γ_i is close to 1.[103–105] However, in silicate melts, γ_i is often less than one, as was measured for Si evaporating from molten SiO_2.[86,106]

The kinetic theory of isotopic fractionation during evaporation was first considered by Kohlweiler[107] and later applied in mercury evaporation experiments by Mulliken and Harkins.[108] It follows from the Hertz-Knudsen equation (eq 2) that the ratio of two isotopes (heavy and light; h and l) in the evaporated gas is given by

$$\frac{J_{h,i}}{J_{l,i}} = \frac{\gamma_{h,i} P_{h,i,\text{eq}}}{\gamma_{l,i} P_{l,i,\text{eq}}} \sqrt{\frac{M_{l,i}}{M_{h,i}}} \tag{3}$$
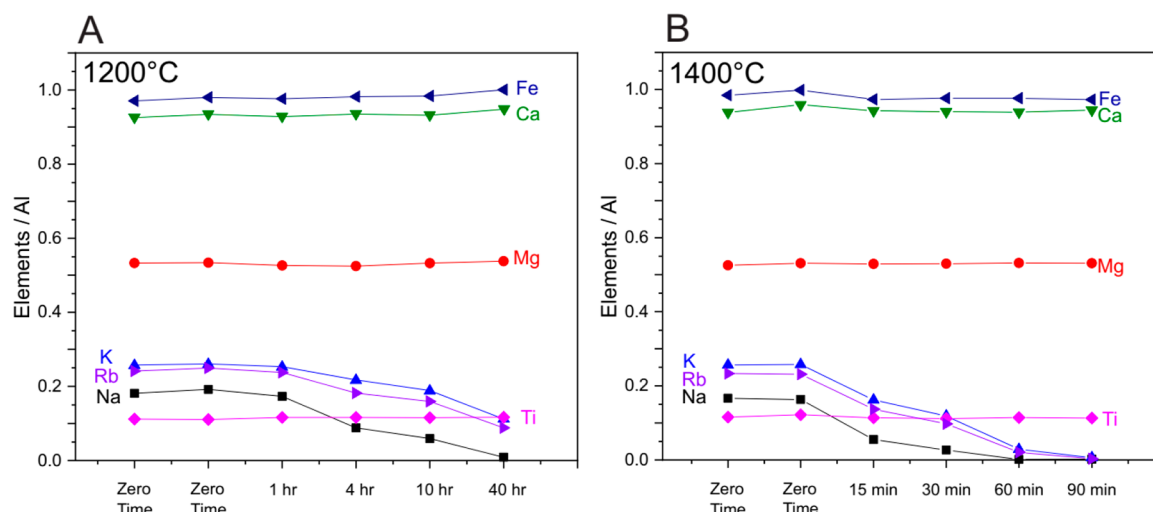
Figure 1. Bulk elemental compositions of evaporation residues at 1200 °C (A) and 1400 °C (B) for different durations (Table 1).
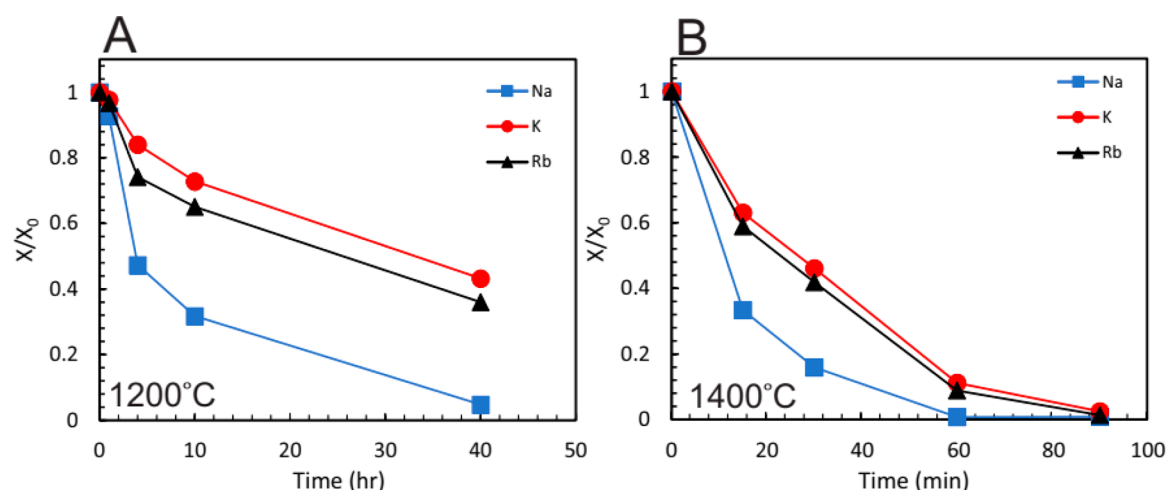
Figure 2. Fractions of Na, K, and Rb remaining in the bulk residues (X/X_0) as a function of time for the 1200 °C (A) and 1400 °C (B) experiments.

At the high temperatures relevant to K and Rb evaporation from silicate melts, Zeng et al.[46] showed that little equilibrium isotopic fractionation is expected between the vapor and melt (~ 0.05–$0.07‰$ for $\delta^{41}K$ and $\sim 0.02‰$ for $\delta^{87}Rb$ at 1200 to 1400 °C), so $P_{h,i,eq}/P_{l,i,eq} \simeq N_{h,i}/N_{l,i}$ with N being the molar density. The condensation/evaporation coefficients can differ between the two isotopes, so the ratio $\gamma_{h,i}/\gamma_{l,i}$ is not always equal to unity and can depend on the isotopic mass. Therefore, eq 3 is often written as

$$J_{h,i}/J_{l,i} = (N_{h,i}/N_{l,i})(M_{l,i}/M_{h,i})^{\beta} \qquad (4)$$

where β is an empirical parameter that should be smaller than 0.5.[36,69,70,87,90,91] Accordingly, the isotopic fractionation between the escaping vapor and the surface of the condensate (liquid or solid) can be expressed as $\alpha = (M_{l,i}/M_{h,i})^{\beta}$. The value of β depends on the element and system considered. Previous studies on evaporation of silicate melts have reported β values between 0.28 and 0.5 for Mg, Si, Fe, Ca, K, and Ti.[69,87,90–92] The β value for K free evaporation was estimated by Richter et al.[27] and Yu et al.[26] to be 0.45 and 0.58, respectively. One of the objectives of the present study is to evaluate the β values for both K and Rb as no datum is available for Rb.

4. RESULTS

4.1. Elemental and Isotopic Compositions of Evaporation Residues. For short runs at 1200 °C (zero-time and 1 h run), the samples had a leaf-like texture resulting most likely from olivine crystallization; the least evaporated evaporation residues also contained some aggregates of iron oxides (Figure S1A), which are chemically close to Fe_2O_3. In long duration runs at 1200 °C and in all runs at 1400 °C (including the zero-time run), no crystalline phase or texture was observed. The run products appear to be a pure glass (Figure S1B–D).

After melting in the gas-mixing furnace, the glass has a Fe^{3+}/Fe_{total} ratio of 0.85 (Figure S4A). The zero-time samples quenched after ramping up the temperature to 1200 or 1400 °C have Fe^{3+}/Fe_{total} ratios of 0.43 and 0.31, respectively. The Fe^{3+}/Fe_{total} ratio does not change much in the course of the evaporation at 1200 °C (0.49 after 8 h and 0.36 after 40 h) and 1400 °C (0.37 after 15 min). Given the high initial Fe^{3+}/Fe_{total} ratio, the oxygen fugacity must be high, and we would expect O_2 to rapidly leave the system, driving the Fe^{3+}/Fe_{total} ratio to lower values. There is however no clear time-dependence of the Fe redox ratio. As discussed below, the reason is that O_2 loss is not limited by evaporation kinetics but rather by reduction kinetics
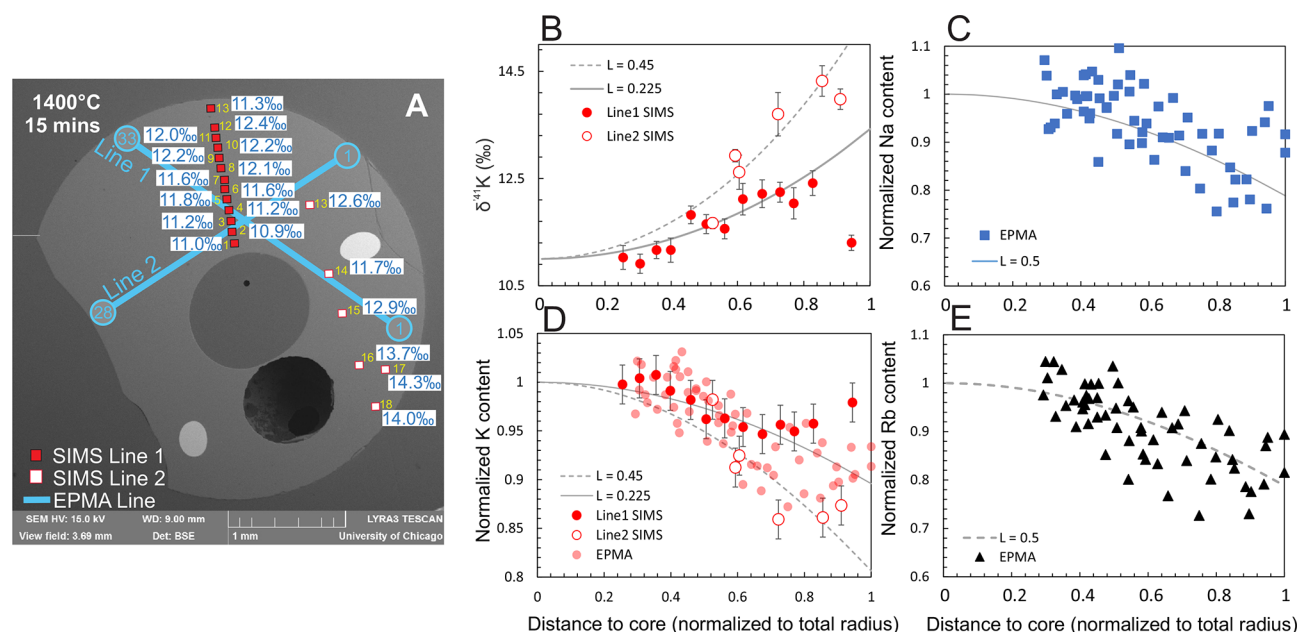
Figure 3. Measurements of isotopic and elemental profiles of Bas1400C15m. (A) Backscattered electron image of the residue. Two series of SIMS analyses were performed: along line 1 (red squares) and along line 2 (white squares). The K isotopic composition is shown for each SIMS spot (Table S3). The chemical composition of the residue was measured by EPMA along two profiles shown as blue lines. (B) K isotopic composition (δ'^{41}K relative to the zero-time sample at 1200 °C). Panels (C−E) show Na, K, and Rb concentration profiles (all normalized to their concentration in the central parts of the sample) from the center to the evaporating surface (Table S3). The K content from SIMS was evaluated by using the ^{39}K/^{40}Ca ratio, assuming that ^{40}Ca remains constant within the sample. The chemical and isotopic composition in the center of the sample was estimated by averaging data from the first 3 SIMS spots along line 1 and several random spots in the central part. Also shown are curves obtained from our model calculations of diffusion-limited evaporation with L values of 0.225 (line 1) and 0.45 (line 2) for potassium, L = 0.5 for rubidium, and L = 0.5 for sodium (see Section 5.2 for details).
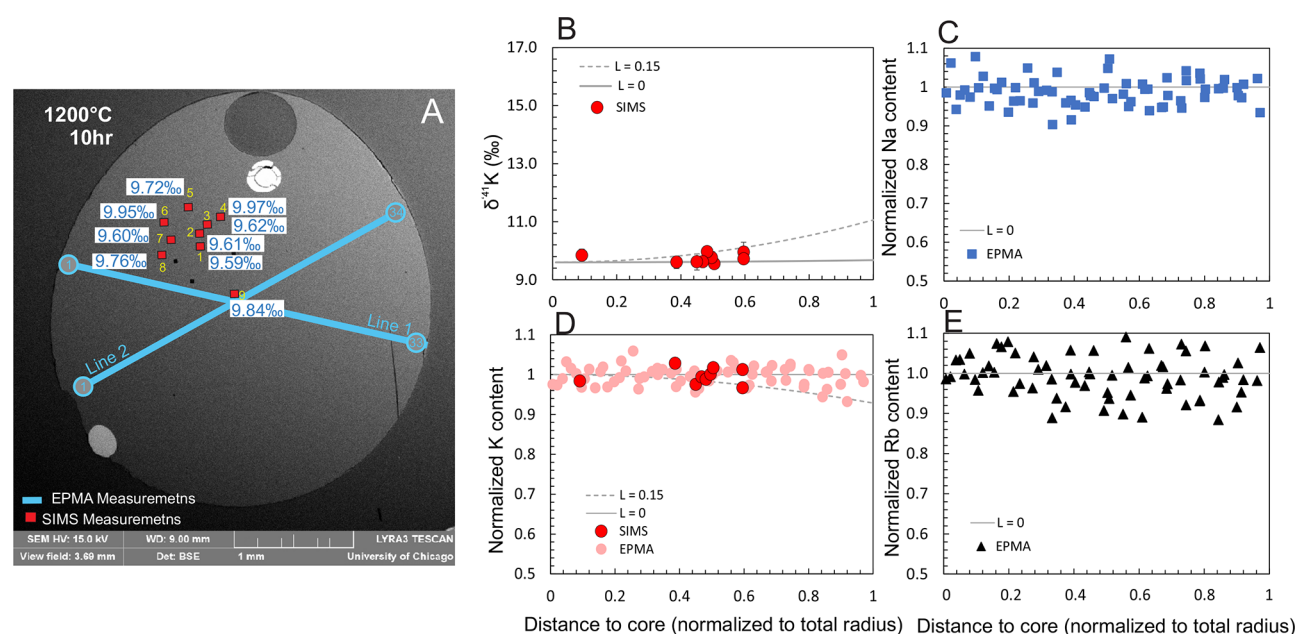
Figure 4. Isotopic and elemental profiles in Bas1200C10h. (A) Backscattered electron image of the sample. (B) K isotopic composition (δ'^{41}K relative to the zero-time sample at 1200 °C). The chemical composition of the residue was measured by EPMA along two profiles shown as blue lines. Panels (C−E) show Na, K, and Rb concentration profiles (all normalized to their concentrations in the central parts of the sample) from the center to the evaporating surface. No chemical and isotopic zonings were observed in this sample, consistent with the fact that the loss of Na, K, and Rb is controlled by evaporation, not diffusion as was the case in the 1400 °C experiments. Also shown are curves that represent the upper limits for L estimated for K (L = 0.15) evaporation (see Section 5.2 for details).

in the melt, notably diffusive replenishment of Fe^{3+} at the melt surface.

Among major and minor elements, only Na, K, and Rb were lost in the experiments (Figure 1). To evaluate the percentage of alkali loss, the alkali concentrations were normalized to Al,

which is a highly refractory element that does not evaporate under the experimental conditions. On the basis of a comparison of the Na/Al, K/Al, and Rb/Al ratios in the zero-time runs with their ratios in the initial mixed powder, we estimate that 11.2%, 8.1%, and 5.5% of Na, K, and Rb, respectively, were lost during ramping up the furnace temperature to 1200 °C and 21.4%, 8.9%, and 10.8% of Na, K, and Rb, respectively, were lost when the furnace was heated to 1400 °C. As discussed in Section 2.2, the chemical compositions of the run products were normalized to the compositions of the zero-time runs to quantify the extent of alkali loss during vacuum evaporation (Figure 2).

Figure 3 shows the chemical and isotopic compositions of the evaporation residue Bas1400C15m that was evaporated for 15 min at 1400 °C. Figure 3A is a backscattered electron image of the sample that shows the locations of the spots where the chemical and isotopic compositions of K were measured. Two linear transverse analyses were carried out on Bas1400C15m by SIMS. The detailed profile (red squares; referred to below as line 1) shows a zoning profile in terms of potassium concentration with a difference (5−15%) between the center and rim. A center-to-surface trend is clearly resolved for K isotopes with the spots near the surface ∼+1.4‰ heavier in $\delta'^{41}K$ compared to those near the center. Line 2 shows much steeper concentration and isotopic profiles with K content around 15% lower near the surface compared to the center. The rim is up to 3‰ heavier in $\delta'^{41}K$ than the center. The major elements are homogeneous within the residues (Table S3). The reason for such different behavior of K along these two lines is unknown. The Rb distribution appears to be heterogeneous with Rb concentration decreasing from the sample center to the rim by ∼20% (Figure 3E). The Na content in evaporation residues measured by EPMA also showed a zoning profile with lower Na content at the rim and higher at the center (∼20% difference; Figure 3C). For longer runs at 1400 °C, the alkali element contents are quite low and uniform without any concentration gradient within the samples. Similarly, no zoning was detected in residues from the 1200 °C runs, where $\delta'^{41}K$ and Na, K, and Rb contents were homogeneous throughout the sample within 5% (Figure 4; Tables S7−S11).

Due to the chemical heterogeneity of some samples, MC-ICPMS data provide a more reliable estimate of the bulk composition of the evaporation residues for Na and Rb. The quality of potassium data obtained by EPMA is significantly better than the data obtained by the MC-ICPMS. Therefore, EPMA data were used to estimate the K content in the bulk samples. The elemental compositions are given in Table 1 (wt % oxide from EPMA as well as Na and Rb normalized to Al from ICPMS). The percentage of alkali elemental loss normalized to zero-time runs are plotted in Figure 2 as a function of time. Figure 2 shows that 96% Na, 60% K, and 66% Rb were evaporated after 40 h long experiments at 1200 °C. Expectedly, the evaporation is much faster at 1400 °C, where 87% Na, 62% K, and 63% Rb were evaporated within 30 min.

4.2. K and Rb Isotopic Fractionation during Evaporation. The K and Rb isotopic compositions of the bulk residues are given in Table 1 and plotted in Figures 5 and 6. The bulk Rb isotopic compositions were measured by MC-ICPMS after digestion of 1/4 of the whole sample (Section 2.3), while the bulk K isotopic values were determined using SIMS profiles either by averaging all in situ analyses for the samples that are homogeneous or by taking the integral $\int C_K(r)\delta'K(r)r^2 \, dr/ \int C_K(r)r^2 \, dr$ for those that are zoned in their K isotopic compositions, where r is the distance to the center (Section 4.1;
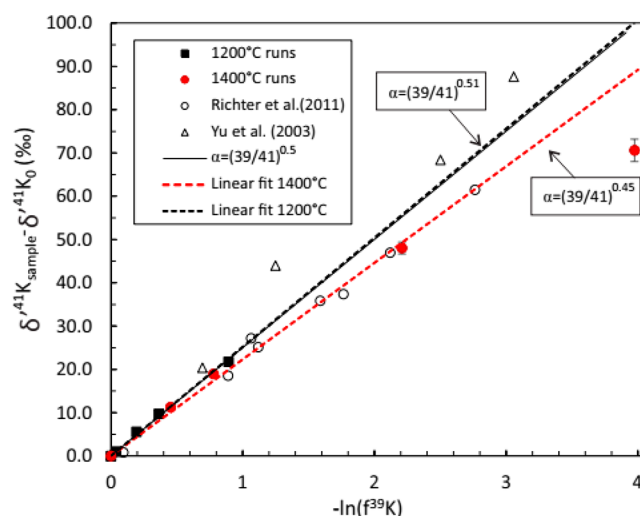
Figure 5. K isotopic compositions of the bulk residues measured by SIMS plotted as a function of −ln f, where f is the fraction of ^{39}K remaining in the residues calculated using EPMA and the abundances of potassium isotopes (Table 1). The open triangles are data from Yu et al.,[26] and the open circles are data from Richter et al.[27] The best-fit line through our data was calculated using Isoplot by forcing the regression through the origin.[109,110]
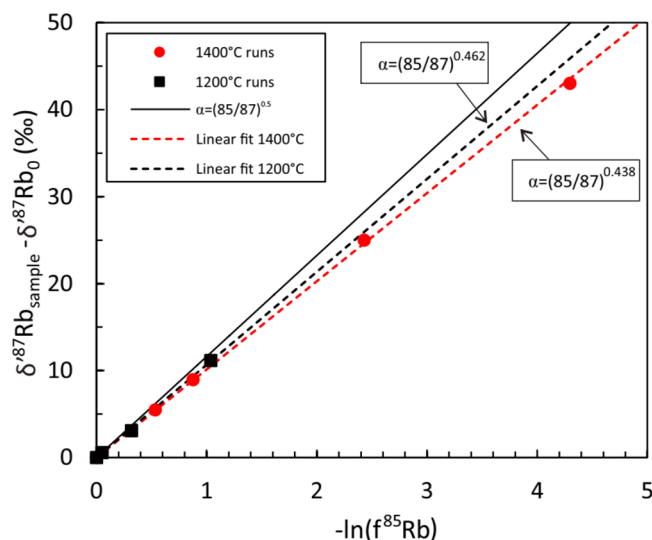
Figure 6. Rb isotopic compositions of bulk residues as a function of −ln f, where f is the fraction of remaining ^{85}Rb in the residues. The error bars for Rb isotopic analyses are smaller than the symbols. The best-fit line through our data was calculated using Isoplot by forcing the regression through the origin.[109,110]

Tables S2−S6). The center of the spherules was determined by fitting the polished section with a circle or ellipse. The distance was then calculated by normalizing the distance "center-SIMS spot" by the distance "center-surface", where the surface is defined as the intersection between the surface and the line running between the center and SIMS spot. The chemically zoned residues also show elevated $\delta'^{41}K$ values at the evaporating surface relative to the center by up to +4‰ (samples Bas1400C0m and Bas1400C15m; Figure 3 and Tables S2 and S3). For the isotopically zoned sample Bas1400C15m, the bulk potassium isotopic composition was calculated using line 1 (closed circles in Figure 3A) and line 2 (open circles in Figure 3A), resulting in bulk $\delta'^{41}K$ values of +11.6‰ and

+12.8‰, respectively. The average of the integrations for both line 1 and line 2 (+12.2‰) is taken as the bulk potassium isotopic composition for Bas1400C15m.

The fractions of remaining ^{39}K or ^{85}Rb (f) were determined using ^{39}K/Al and ^{85}Rb/Al ratios in the bulk residues and zero-time runs (^{85}Rb was directly measured by ICPMS; ^{39}K was calculated using the K content in the sample and relative abundances of its isotopes). Shown in Figure 5 is a weighted linear fit using a modified method from Isoplot model 3[109] outlined in McIntyre[110] that describes the linear relationship between δ'^{41}K and $-\ln f$ for the bulk 1400 °C residues. The calculated slope is 22.3 ± 1.8 (95% confidence interval for the best weighted fit line forced to pass through the origin). Such a linear relationship is expected for a Rayleigh distillation, $\delta' = -1000(\alpha - 1) \ln f$, where α is the instantaneous isotopic fractionation factor between the vapor and bulk residue. From the slope of the correlation, we calculate $\alpha = 0.9770 \pm 0.0022$ (95% confidence interval). As discussed in Section 3, kinetic isotopic fractionation during evaporation can be parametrized as $\alpha = (38.964/40.962)^{\beta}$ for K and $(84.912/86.909)^{\beta}$ for Rb. The calculated β-exponent for K is 0.45 ± 0.05 in the 1400 °C evaporation series, which is close to the β value of 0.43 ± 0.03 obtained by Richter et al.[27] for evaporation of K from chondritic melt at 1470 °C and slightly smaller than $\beta = 0.54 \pm 0.02$ obtained by Yu et al.[26] for chondritic melt evaporation at 1450 °C. The linear relationship between δ'^{41}K and $-\ln f$ for the 1200 °C evaporation series yields a slope of 25.2 ± 1.2, corresponding to $\alpha = 0.9748 \pm 0.0012$. The apparent β-exponent for K in the 1200 °C run is 0.51 ± 0.03, slightly larger than the values of Richter et al.[27] and slighter smaller than Yu et al.[26] The data from the 1200 °C evaporation series span a limited range of depletion, and the value of the slope is relatively uncertain and possibly less accurate than the 1400 °C run because δ'^{41}K depends more sensitively on the value of the zero-time run. We also ran a best fit line without forcing it to pass through the origin to try to assess the influence that the zero-time run could have, and we find β-exponents of 0.51 ± 0.01 and 0.45 ± 0.05 for the 1200 and 1400 °C runs, respectively. Overall, all K evaporation experiments done to date yield a β-exponent close to the ideal limit of 0.5 (this study; Richter et al.;[27] Yu et al.[26]).

The correlations between δ'^{87}Rb and $-\ln f$ for the 1200 and 1400 °C evaporation runs are shown in Figure 6. The correlations are linear, indicating that evaporation follows a Rayleigh distillation. The slopes of the correlations are 10.1376 ± 0.1348 and 10.6797 ± 0.3027 (using a weighted fitting with uncertainty under a 95% confidence level) for the 1400 and 1200 °C runs, respectively. The corresponding β-exponents for Rb in the 1400 and 1200 °C runs are 0.438 ± 0.006 and 0.462 ± 0.013, respectively. The β-exponents for Rb are all slightly smaller than the ideal limit of 0.5.

5. DISCUSSION

5.1. Modeling Chemical and Isotopic Fractionation in a Diffusion-Limited Regime.
The concentration and isotopic profiles of K at 1400 °C are most likely due to diffusion-limited transport in a molten sphere, as we would indeed expect potassium near the surface to be more depleted and isotopically fractionated than the center. Diffusion-limited evaporation was investigated in several studies using numerical and analytical methods.[36,71,78,80,81] Most studies focused on the evaporation of a major component, which would involve a moving boundary.[35,36,78–80,111] Sossi et al.[81] modeled diffusion-limited evaporation of minor and trace elements numerically. Below, we

derive analytical equations that describe evaporation kinetics and isotopic fractionation for minor and trace elements. We are concerned with evaporation of a minor melt component, which has a negligible effect on the sample size. For example, the total alkali element content in the starting composition is around 6.4 wt % (Na, K, and Rb content in Bas1400C0m1). Even if all alkali elements had been completely evaporated, such loss would have only shifted the radius of the sample sphere from 1.50 to 1.47 mm. If the diffusion rate was smaller than the boundary moving rate, the formulas given below would not be applicable.

The differential equation that governs diffusion in a sphere is

$$\frac{\partial C}{\partial t} = D \frac{\partial^2 C}{\partial r^2} + \frac{2D}{r} \frac{\partial C}{\partial r} \tag{5}$$

where C stands for molar density of the investigated element and D, r, and t stand for diffusivity, radius, and time. The initial and boundary conditions take into account the following considerations: (i) the initial concentration is uniform, (ii) the concentration profile is symmetric, and we have a no-flux boundary condition at the center, and (iii) at the liquid−vapor interface, the evaporative flux is equal to the diffusive flux. These conditions translate into the following equations

$$C = C_0 \quad r > 0, \ t = 0$$

$$-D \frac{\partial C}{\partial r} = 0 \quad r = 0, \ t > 0$$

$$-D \frac{\partial C}{\partial r} = J = \nu C \quad r = R_0, \ t > 0 \tag{6}$$

where R_0 is the sphere radius, J is the evaporation rate, and ν is a coefficient defined as the evaporation rate (molar per unit surface area per second) divided by the molar density (molar per volume) of the element under consideration. The analytical solution to this differential equation with these boundary and initial conditions was given by Crank[112] and later used by Hashimoto[113] for interpreting variations in the Fe content of evaporative residues. It takes the form

$$\frac{C(r, t)}{C_0} = \frac{2LR_0}{r} \sum_{l=1}^{\infty} \frac{e^{-(\theta_l \sqrt{Dt}/R_0)^2}}{\theta_l^2 + L(L-1)} \frac{\sin(\theta_l r/R_0)}{\sin \theta_l} \tag{7}$$

where $L = \nu R_0/D$ is a dimensionless parameter, which as shown below is proportional to the ratio of the diffusion time scale (τ_{Diff}) to the evaporation time scale (τ_{Evap}). A higher L means that the sample is more likely to be diffusion limited and vice versa; L takes its values between 0 and $+\infty$. The evaporation timescale is commonly defined on the basis of the initial concentration and evaporative flux as

$$\tau_{\text{Evap}} = \frac{C_0 V}{J_0 A} = \left(\frac{4}{3}\pi R_0^3 C_0\right)/(4\pi R_0^2 J_0) = R_0 C_0/3J_0 \tag{8}$$

where C_0 is the initial molar density in mol/cm^3, J_0 is the evaporation rate for the starting composition in mol/cm^2/s, and R_0 is the initial radius of the sphere in cm. The evaporation timescale can be simplified as $\tau_{\text{Evap}} = R_0/3\nu$, using $J = \nu C$.

The diffusion timescale is defined following Richter[35] as

$$\tau_{\text{Diff}} = R_0^2/D \tag{9}$$

where D is diffusion coefficient in cm^2/s. Combining eqs 8 and 9, we find that L is proportional to the ratio of the timescales of diffusion and evaporation
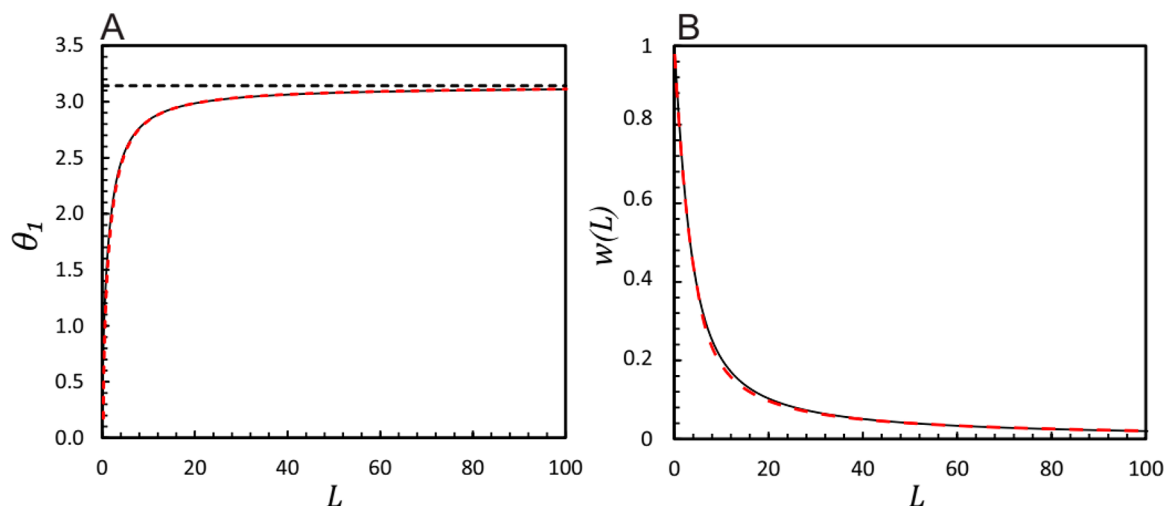
Figure 7. (A) θ_1 values as a function of $L = 1 - \theta_1 \cot \theta_1$. (B) Weight function $w(L)$ as a function of L. The continuous black lines are exact values (eqs 11 and 29) while red dashed lines are approximate expressions (eqs 12 and 30).

$$\tau_{\text{Diff}}/\tau_{\text{Evap}} = 3\nu R_0/D = 3L \tag{10}$$

In eq 7, the θ_l values are the positive roots of the transcendental equation

$$\theta_l \cot \theta_l - 1 + L = 0 \tag{11}$$

This equation has an infinite number of solutions as cot is a periodic function. The higher θ_l values are separated by π, and the higher-order terms ($l > 1$) in eq 7 rapidly become negligible after a characteristic time $t_{\text{SS}} = R_0^2/D \times 0.09L^{-0.06}$ has passed. We call this regime when the higher-order terms can be neglected "quasi-steady state". In our case, this quasi-steady state time is estimated to be reached after 4 and 6 min for K and Rb at 1400 °C, respectively (Figure S5). As discussed below, truncating the formula to the first θ_1 term (θ_1 takes its values between 0 and π) gives a good approximation in most cases. In Figure 7A, we plot the values of θ_1 as a function of L. An approximation for θ_1 as a function of L is given by Padé approximants,

$$\theta_1 \simeq \begin{cases} \sqrt{\dfrac{15}{L+5}} & 0 \le L < 0.57782 \\[2ex] \dfrac{\pi}{2} + \dfrac{2(L-1)\pi}{4(L-1) + \pi^2} & 0.57782 \le L < 5 \\[2ex] \dfrac{\pi(9L - 3 + 2\pi^2 - \sqrt{9(L+1)^2 + 12\pi^2})}{2(3L + \pi^2)} & L \ge 5 \end{cases} \tag{12}$$

Having established a relationship between the concentration profile and time through eq 7, we can derive several other quantities that relate to observables. The fraction of an element remaining after evaporation $f = N(t)/N(0)$ can be calculated by integrating the concentration in eq 7 between $r = 0$ and R_0 (details are given in the Supporting Information).

$$f = 6L^2 \sum_{l=1}^{\infty} \frac{e^{-(\theta_l \sqrt{Dt}/R_0)^2}}{\theta_l^2[\theta_l^2 + L(L-1)]} \tag{13}$$

which at quasi-steady state can be approximated by

$$f \simeq \frac{6L^2 e^{-(\theta_1 \sqrt{Dt}/R_0)^2}}{\theta_1^2[\theta_1^2 + L(L-1)]} \tag{14}$$

In a Rayleigh distillation, $\ln f$ is used to calculate instantaneous isotopic fractionation are

$$\ln f \simeq -\left(\frac{\theta_1 \sqrt{Dt}}{R_0}\right)^2 + \ln \frac{6L^2}{\theta_1^2[\theta_1^2 + L(L-1)]} \tag{15}$$

The second term takes a value of 0 for $L = 0$ and decreases with increasing L to reach a minimum value of $-1/2$ for $L \to +\infty$. The first term on the other hand takes a value of -1 at quasi-steady state time (t_{SS}), and its absolute value rapidly decreases to approach zero after that. At quasi-steady state, the first term therefore dominates, and to a good approximation, we have

$$\ln f \simeq -\left(\frac{\theta_1 \sqrt{Dt}}{R_0}\right)^2 \tag{16}$$

The evaporative flux is related to the concentration at the liquid/vapor interface $C(R_0, t)$ through the Hertz-Knudsen equation. At quasi-steady state, the profile normalized to the concentration at the center assumes a form that does not depend on time

$$\frac{C(r, t)}{C(r = 0, t)} \simeq \frac{\sin(\theta_1 r/R_0)}{\theta_1 r/R_0} \tag{17}$$

Measurement of the concentration at the interface can be difficult, but we can relate the surface concentration to that of the bulk residue by integrating eq 17 from the center to the surface, which gives (see the Supporting Information for more details)

$$C(R_0, t) \simeq \frac{\theta_1^2}{3L} C_{\text{bulk}}(t) \tag{18}$$

We use eq 18 in our modeling of evaporation as it allows us to relate the surface concentration in the liquid, which we only measured for K and Rb in a few samples, to the bulk concentrations that we measured precisely for Na, K, and Rb in all samples.

Equation 7 can also be used to calculate isotopic fractionation during evaporation

$$\delta'_{i/j}(r, t) = 1000 \ln\left(\frac{R_{i,j}}{R_{i,j,0}}\right)$$

$$= 1000 \ln \frac{L_i \sum_{l=1}^{\infty} \frac{e^{-(\theta_{l,i}\sqrt{D_i t}/R_0)^2}}{\theta_{l,i}^2 + L_i(L_i - 1)} \frac{\sin(\theta_{l,i}r/R_0)}{\sin\theta_{l,i}}}{L_j \sum_{l=1}^{\infty} \frac{e^{-(\theta_{l,j}\sqrt{D_j t}/R_0)^2}}{\theta_{l,j}^2 + L_j(L_j - 1)} \frac{\sin(\theta_{l,j}r/R_0)}{\sin\theta_{l,j}}} \tag{19}$$

which truncated to the first order for the isotopic composition of the residue gives

$$\delta'_{i/j}(r, t) = 1000(\theta_{1,j}^2 D_j - \theta_{1,i}^2 D_i)\frac{t}{R_0^2}$$

$$+ 1000 \ln \frac{L_i \sin(\theta_{l,i}r/R_0)[\theta_{l,j}^2 + L_j(L_j - 1)]\sin\theta_{l,j}}{L_j \sin(\theta_{l,j}r/R_0)[\theta_{l,i}^2 + L_i(L_i - 1)]\sin\theta_{l,i}} \tag{20}$$

The second term is constant while the first term increases in magnitude with time. At quasi-steady state, the first term dominates and we have

$$\delta'_{i/j,\text{bulk}}(t) \simeq 1000(\theta_{1,j}^2 D_j - \theta_{1,i}^2 D_i)\frac{t}{R_0^2} \tag{21}$$

When the expression for $\ln f$ from eq 16 is introduced, we have

$$\delta'_{i/j,\text{bulk}}(t) \simeq 1000\left(\frac{\theta_{1,j}^2 D_j}{\theta_{1,i}^2 D_i} - 1\right)(-\ln f) \tag{22}$$

We recognize the equation of a Rayleigh distillation whereby the instantaneous fractionation between the evaporating flux and the bulk residue is

$$\alpha_{\text{vapor-residue}}^{i/j} = \frac{\theta_{1,j}^2 D_j}{\theta_{1,i}^2 D_i} \tag{23}$$

When L approaches 0 (diffusion-free regime), $\theta_1^2 \simeq 3L \simeq 3\nu R_0/D$. We therefore recover $\alpha_{\text{vapor-residue}}^{i/j} \simeq \nu_j/\nu_i$, meaning that isotopic fractionation in the bulk residue during evaporation is entirely set by differences in volatilities of the isotopes. Conversely, when L is large (highly diffusion-limited regime), $\theta_1^2 \simeq \pi^2$ and $\alpha_{\text{vapor-residue}}^{i/j} \simeq D_j/D_i$, meaning that isotopic fractionation in the bulk residue is entirely set by differences in diffusivities of the isotopes. When evaporation is partially diffusion limited, the Rayleigh isotopic fractionation factor will assume values intermediate between these two endmembers. Below, we modify eq 23 to more explicitly express the dependence of the Rayleigh isotopic fractionation factor on L.

If we note that $L = g(\theta_1) = 1 - \theta_1 \cot \theta_1$, the inverse function of $g(\theta_1)$ can be written as $\theta_1 = g^{-1}(L)$. With this function, the

instantaneous isotopic fractionation factor between vapor and bulk residue is $\alpha_{\text{vapor-residue}}^{i/j} = \frac{D_j}{D_i}\left(\frac{g^{-1}(L_j)}{g^{-1}(L_i)}\right)^2$. This can be approximated using a Taylor-series expansion

$$\alpha_{\text{vapor-residue}}^{i/j} \simeq$$

$$\frac{D_j}{D_i}\left\{\frac{1}{g^{-1}(L_i)}\left[g^{-1}(L_i) + \frac{\partial g^{-1}(L)}{\partial L}(L_j - L_i)\right]\right\}^2 \tag{24}$$

When the inverse function theorem is applied $\left(\frac{\partial g^{-1}(L)}{\partial L} = \frac{1}{g'(\theta_1)}\right)$, the equation above can be simplified as

$$\alpha_{\text{vapor-residue}}^{i/j} \simeq \frac{D_j}{D_i}\left[1 + \frac{1}{g^{-1}(L_i)}\frac{1}{g'(\theta_1)}(L_j - L_i)\right]^2 \tag{25}$$

With the relationships $L = g(\theta_1) = 1 - \theta_1 \cot\theta_1$ and $g^{-1}(L_i) = \theta_1$, eq 25 can be written as

$$\alpha_{\text{vapor-residue}}^{i/j} \simeq \frac{D_j}{D_i}\left[1 + \frac{L_j - L_i}{\frac{(L-1)^2}{\cos^2\theta_1} + L - 1}\right]^2 \simeq \frac{D_j}{D_i}$$

$$\left[1 + \frac{2(L_j - L_i)}{\frac{(L-1)^2}{\cos^2\theta_1} + L - 1}\right] \tag{26}$$

Rearranging the equation above, we therefore have

$$\alpha_{\text{vapor-residue}}^{i/j} \simeq \frac{D_j}{D_i}\left[1 - \frac{2(L_i)}{\frac{(L-1)^2}{\cos^2\theta_1} + L - 1}\right]$$

$$+ \left[\frac{2L_i}{\frac{(L-1)^2}{\cos^2\theta_1} + L - 1}\right]\left(\frac{L_j D_j}{L_i D_i}\right) \tag{27}$$

which can be simplified as

$$\alpha_{\text{vapor-residue}}^{i/j} = [1 - w(L)]\frac{D_j}{D_i} + w(L)\frac{\nu_j}{\nu_i} \tag{28}$$

where the weight function is defined as

$$w(L) = \frac{2L}{L - 1 + (L - 1)^2/\cos^2(\theta_1)} \tag{29}$$

This function can be approximated using Padé approximants as

$$w(L) \simeq \begin{cases} \dfrac{2L + 10}{L^2 + 4L + 10} & 0 \le L < 0.57782 \\[2ex] \dfrac{8L(4L - 4 + \pi^2)^2}{64(L-1)^3 L + 32(L-1)^2(L+2)\pi^2 + 4(L-1)(L+4)\pi^4 + \pi^6} & 0.57782 \le L < 5 \\[2ex] \dfrac{4L(3L + \pi^2)^2}{18L^4 + 6(2\pi^2 + 3)L^3 + \pi^2(2\pi^2 + 33)L^2 + 2\pi^2(8\pi^2 - 9)L + 2\pi^6 + 9\pi^2 - \pi^2(9L + 2\pi^2 - 3)\sqrt{9(L+1)^2 + 12\pi^2}} & L \ge 5 \end{cases} \tag{30}$$

If we write (i) $\alpha_{\text{vapor-residue}}^{i/j} = (m_j/m_i)^\beta$ with β being the measured isotopic fractionation exponent relevant to the bulk residue resulting from a combination of differences in evaporation rates and melt diffusivities of the isotopes, (ii) $\nu_j/$

$\nu_i = (m_i/m_j)^{\beta*}$ with $\beta*$ being the isotopic fractionation exponent describing kinetic isotopic fractionation at the liquid/vapor interface, and (iii) $D_j/D_i = (m_i/m_j)^\zeta$ with ζ being the isotopic fractionation exponent for diffusion, we can rewrite eq 28 as
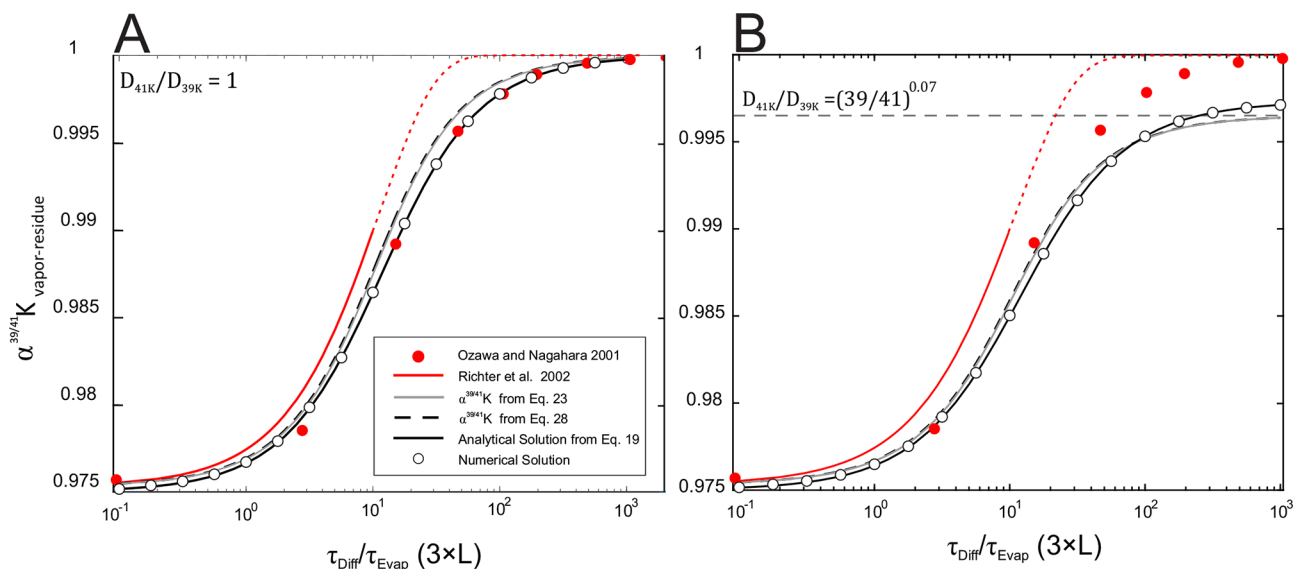
Figure 8. K isotopic fractionation factors between vapor and bulk residues plotted as a function of ratios of diffusion time scale (τ_{Diff}) over evaporation time scale (τ_{Evap}). (A) Using $D_{41K}/D_{39K} = 1$, which is the condition used by Richter et al.[36] and Ozawa and Nagahara.[80] (B) Using $D_{41K}/D_{39K} = (39/41)^{0.07}$ (see the text for details). In the highly diffusion-limited regime ($\tau_{\text{Diff}}/\tau_{\text{Evap}} > 1000$), the bulk isotopic fractionation is determined by diffusivities of isotopes in the liquid ($\alpha^{39/41}K = (39/41)^{0.07}$ in this study). In the diffusion-free regime ($\tau_{\text{Diff}}/\tau_{\text{Evap}} < 0.1$), the bulk isotopic fractionation is set by the volatilities of the isotopes ($\alpha^{39/41}K = (39/41)^{0.5}$ in this study). The red solid line is an empirical fit to numerical simulation given by Richter et al.[36] for L below 10, and the red dashed line is using the same parametric formula for larger L values. The gray line is calculated using eq 23. The dashed black line is the approximate formula given by eq 28. The solid black line is calculated analytically using eq 19 by taking the first ten θ_l roots of eq 11 ($l = 1-10$). The open circles are numerical solutions by solving eq 5 with the Crank-Nicolson finite difference method. As shown, the equation given by Richter et al.[36] (for L below ~10) and numerical results by Ozawa and Nagahara[80] adequately describe the behavior of the system.

$$(m_i/m_j)^\beta = w(L)(m_i/m_j)^{\beta*} + [1 - w(L)](m_i/m_j)^\zeta \quad (31)$$

Using the approximation $(1 + x)^k \simeq 1 + kx$ for x close to zero, we have

$$\beta \simeq w(L)\beta* + [1 - w(L)]\zeta \quad (32)$$

In Figure 7B, we plot the weight function w as a function of L. As expected, in the diffusion-free regime with $L = 0$, w is close to 1 and the isotopic fractionation is entirely dominated by the kinetic evaporation term $\nu_j/\nu_i = (m_i/m_j)^{\beta*}$ (Figure 8). In the diffusion-limited regime with larger L, w decreases toward 0 and the isotopic fractionation becomes dominated by the term corresponding to diffusion in the liquid $D_j/D_i = (m_i/m_j)^\zeta$ (Figure 8). Richter et al.[36] recognized that the presence of diffusive effects in the melt would reduce the apparent isotopic fractionation factor associated with evaporation, and they were able to fit their numerical results for Mg using an empirical equation. Ozawa and Nagahara[80] studied diffusion-limited evaporation using a numerical simulation with a moving boundary condition. Sossi et al.[81] also performed a numerical simulation to model diffusion-limited isotopic fractionation and provided an empirical fit to their results. We show here that diffusion-limited evaporation of a minor element from a sphere can be formalized using an analytical equation for the quasi-steady state regime (eq 28). As shown in Figure 8A,B, our approximate solution (eqs 26−30) agrees well with the exact analytical solution (eq 19) and a numerical calculation that we performed. The models from Richter et al.[36] and Ozawa and Nagahara[80] assumed identical diffusivities for different isotopes. When the same condition ($D_{39K}/D_{41K} = 1$) is applied, our result agrees well with the empirical fit of Richter et al.[36] for values of L below 10, but the departure becomes significant when the regime is highly diffusion limited. Our results also agree well with the numerical results of Ozawa and Nagahara[80] for all L

values (Figure 8A). If we take into account isotopic fractionation by diffusion in liquid, our results expectedly further depart from those of Richter et al.[36] and Ozawa and Nagahara[80] in the most diffusion-limited regime (Figure 8B). Sossi et al.[81] used an unusual definition of evaporation timescale, and we are unable to compare their numerical results with our analytical equation.

Using eq 20, we can also express the isotopic composition at quasi-steady state along a profile relative to the isotopic composition at the center

$$\delta'_{i/j}(r, t) - \delta'_{i/j}(r = 0, t) \simeq 1000 \times \ln\left[\frac{\sin(\theta_{1,i}r/R_0)}{\sin(\theta_{1,j}r/R_0)}\frac{\theta_{1,j}}{\theta_{1,i}}\right] \quad (33)$$

The analytical formulas described above have been compared with numerical results using the Crank-Nicolson finite difference method. The two methods produce consistent results (Figure S5), which further validates the derivations.

For completeness, we have calculated analytically how diffusion-limited transport would affect evaporation kinetics and isotopic fractionation in cylinder and planar sheet geometries.[112] The derivations are similar to those for a sphere. For brevity, these steps are not repeated below.

For diffusion-limited evaporation in a planar sheet, the boundary conditions are similar to eq 6. The function describing the concentration $C(r, t)$ at any given time and position is given by Crank[112]

$$\frac{C(r, t)}{C_0} = \sum_{m=1}^{\infty} \frac{2L\cos(\theta_m x/l)e^{-(\theta_m/l)^2 Dt}}{(\theta_m^2 + L^2 + L)\cos\theta_m} \quad (34)$$

where C_0 is initial concentration, l is the half length of the plane sheet with $-l < x < +l$, D is the diffusion coefficient, θ_m are the positive roots of

$$\theta \tan \theta = L \tag{35}$$

and L is the diffusion time scale over the evaporation time scale

$$L = \nu l / D \tag{36}$$

The dependence of θ_1 on L can be approximated as

$$\theta_1 = \begin{cases} \sqrt{\dfrac{3L}{L+3}} & L < 1 \\[2ex] \dfrac{1.34L + 0.36}{0.85L + 1.12} & L > 1 \end{cases} \tag{37}$$

The fraction of an element remaining $f = N(t)/N(0)$ after evaporation is obtained by integrating eq 34 over the sheet thickness

$$f = \sum_{m=1}^{\infty} \frac{2L^2 e^{-(\theta_m/l)^2 Dt}}{\theta_m^2 (\theta_m^2 + L^2 + L)} \tag{38}$$

At quasi-steady state, the chemical profile is thus

$$\frac{C(x, t)}{C(x = 0, t)} \simeq \cos(\theta_1 x/l) \tag{39}$$

The surface molar density is

$$C(l, t) \simeq \frac{\theta_1^2}{L} C_{\text{bulk}}(t) \tag{40}$$

The quasi-steady state isotopic profile is

$$\delta'_{i,j}(x) - \delta'_{i,j}(x = 0) \simeq 1000 \times \ln\left[\frac{\cos\left(\theta_{i,1}\frac{x}{l}\right)}{\cos\left(\theta_{j,1}\frac{x}{l}\right)} \right] \tag{41}$$

The bulk isotopic composition is

$$\delta'_{i,j,\text{bulk}} \simeq 1000 \times \left(\frac{\theta_{j,1}^2 D_j}{\theta_{i,1}^2 D_i} - 1 \right) \times (-\ln f) \tag{42}$$

The isotopic fractionation factor between the vapor and bulk residue can be written as

$$\alpha^{i/j}_{\text{vapor-residue}} = [1 - w(L)]\frac{D_j}{D_i} + w(L)\frac{\nu_j}{\nu_i} \tag{43}$$

where the weight function is

$$w(L) = \frac{2L}{\theta_1^2 \sec^2 \theta_1 + L} \tag{44}$$

The weight function can be approximated as

$$w(L) = \begin{cases} \dfrac{2}{\frac{3}{L+3} / \left(\cos^2 \sqrt{\frac{3L}{L+3}}\right) + 1} & L < 1 \\[3ex] \dfrac{2}{\left(\frac{1.34L + 0.36}{0.85L + 1.12}\right)^2 / \left(\cos \frac{1.34L + 0.36}{0.85L + 1.12}\right)^2 + 1} & L > 1 \end{cases} \tag{45}$$

For diffusion-limited evaporation in a cylinder, the elemental concentration for different times and positions is given by Crank[112]

$$\frac{C(r, t)}{C_0} = \sum_{m=1}^{\infty} \frac{2LJ_0(r\theta_m/a)}{(\theta_m^2 + L^2)J_0(\theta_m)} e^{-(\theta_m/a)^2 Dt} \tag{46}$$

where a is radius of the cylinder and θ is a series of roots of the Bessel functions

$$\theta J_1(\theta) - L J_0(\theta) = 0 \tag{47}$$

with $J_0(\theta)$ and $J_1(\theta)$ the Bessel functions of orders zero and one, respectively, and L defined as

$$L = \nu a / D \tag{48}$$

θ_1 is a function of L that can be approximated as

$$\theta_1 \simeq \begin{cases} \sqrt{\dfrac{8L}{L+4}} & 0 \le L < 1 \\[2ex] \dfrac{7.14L + 0.92}{2.95L + 3.64} & L > 1 \end{cases} \tag{49}$$

The fraction of an element remaining $f = N(t)/N(0)$ after evaporation is

$$f = \sum_{m=1}^{\infty} \frac{4L^2 e^{-\left(\frac{\theta_m}{a}\right)^2 Dt}}{\theta_m^2 (\theta_m^2 + L^2)} \tag{50}$$

At quasi-steady state, the concentration profile normalized to the center can be approximated as

$$\frac{C(r, t)}{C(r = 0, t)} \simeq J_0(r\theta_1/a) \tag{51}$$

The bulk composition is related to the surface concentration through the following approximation

$$C(R_0, t) \simeq \frac{\theta_1^2}{2L} C_{\text{bulk}}(t) \tag{52}$$

The isotopic profile at quasi-steady state is

$$\delta'_{i,j}(r) - \delta'_{i,j}(r = 0) = 1000 \times \ln\left[\frac{J_0(r\theta_{i,1}/a)}{J_0(r\theta_{j,1}/a)} \right] \tag{53}$$

The bulk isotopic composition of the residue can be written as

$$\delta'_{i,j,\text{bulk}} \simeq 1000 \times \left(\frac{\theta_{j,1}^2 D_j}{\theta_{i,1}^2 D_i} - 1 \right)(-\ln f) \tag{54}$$

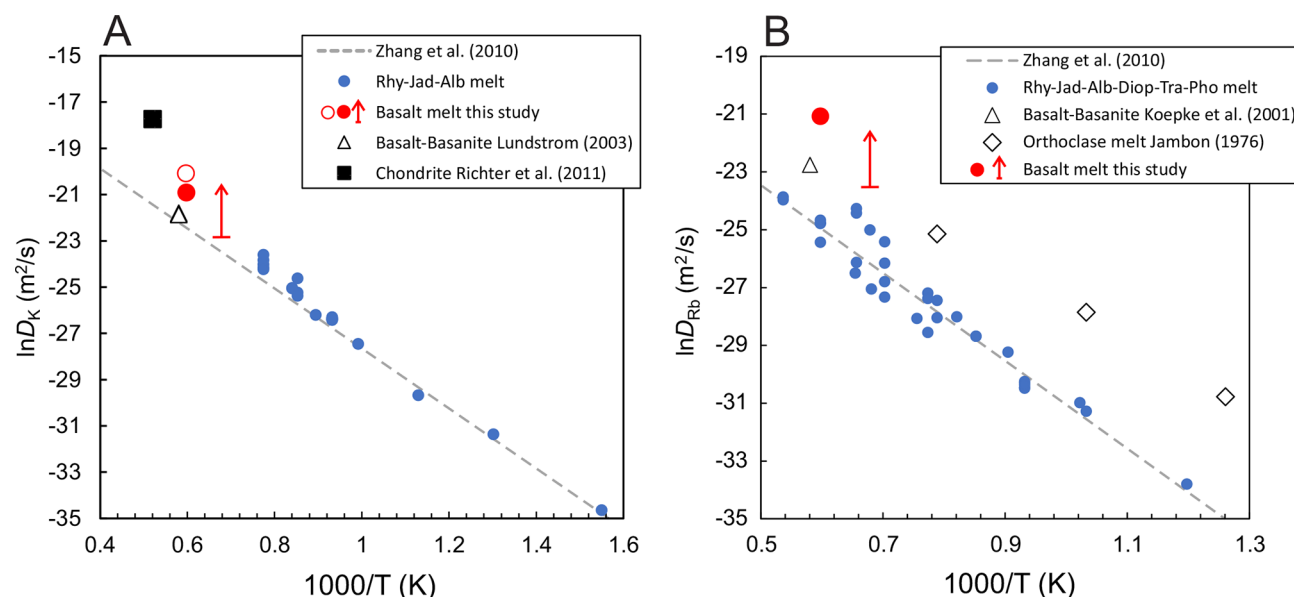The isotopic fractionation factor between vapor and bulk residue is thus

$$\alpha^{i/j}_{\text{vapor-residue}} = [1 - w(L)]\frac{D_j}{D_i} + w(L)\frac{\nu_j}{\nu_i} \tag{55}$$

with the weight function defined as

$$w(L) = \frac{2L}{(L^2 + \theta^2)} \tag{56}$$

The weight function can be approximated as

$$w(L) \simeq \begin{cases} \dfrac{2}{L + \frac{8}{L+4}} & L < 1 \\[3ex] \dfrac{2L}{L^2 + \left(\frac{7.14L + 0.92}{2.95L + 3.64}\right)^2} & L > 1 \end{cases} \tag{57}$$

Figure 9. Estimated diffusion coefficients for (A) K and (B) Rb from this study and from the literature. The dotted gray lines are linear fits as described by Zhang et al.[118] The diffusion coefficients for the 1400 °C runs were estimated from two trends for zoning profiles of K isotopic and concentration (red-filled circle for line 2 and red-unfilled circle for line 1). The 1200 °C runs are not diffusion limited, so we can only estimate the lowest diffusion coefficients, shown as the end of the red arrow. The data compiled by Zhang et al.[118] (blue circles) are felsic compositions (e.g., rhyolite, albite, diopside, trachyte, orthoclase, phonolite, and jadeite melt). The data for basaltic composition are from Lundstrom[153] and Koepke and Behrens[154] The diffusivity of K in chondritic melts (black square) is from Richter et al.[27]

5.2. Relative Volatilities of K and Rb Isotopes. The fact that the residual glass beads from the 1400 °C experiment show nonuniform chemical and isotopic profiles for K (Figure 3) suggests that diffusive transport in molten droplets played an important role during evaporation. As discussed in Section 5.1, the parameter that controls the extent to which evaporation is diffusion limited or not is the ratio of diffusion and evaporation time scale: $\tau_{Diff}/\tau_{Evap} = 3L$. We have adjusted the parameter L in order to fit the chemical profile of K in the 1400 °C Bas1400C15m experiment using eq 17, and we get values of 0.225 for line 1 analyses and 0.45 for line 2 analyses (Figure 3). Assuming a Rayleigh distillation behavior, we were able to constrain the β-exponent for K in the 1400 °C evaporation experiments using estimates of the bulk δ'^{41}K values. Equation 22 shows that diffusion-limited transport would decrease the extent of isotopic fractionation during evaporation of K in these experiments. Using the L value for K concentration and assuming that the ratio of the diffusivities of K is $D_i/D_j = (m_j/m_i)^{\zeta}$,[114,115] we can use eq 28 to correct the β-exponents calculated from the bulk isotopic compositions for this diffusive effect. Using eq 28, we indeed have

$$\beta^* \simeq \frac{\beta}{w(L)} - \left[1 - \frac{1}{w(L)}\right]\zeta \tag{58}$$

In the 1400 °C evaporation experiments, w is 0.91 for K line 1 analyses and 0.95 for K line 2 analyses (Figure 7). In the 1200 °C evaporation experiments, the lowest possible w value is ~0.998 for K (the data are consistent with no diffusion-limited evaporation and a w value of 1). No data are available on values of ζ for K in silicate melt, but as discussed by Watkins et al.,[116] the isotopic fractionation imparted by diffusion in silicate melt correlates with the ratio of the diffusivities between solute and solvent. Using the diffusion coefficients of Richter et al.[117] and the relationship of Watkins et al.,[116] we estimate that ζ must be ~0.07 for K. We thus revise the β-exponents in the 1400 °C

experiment from 0.45 to 0.47 for K based on line 1 analyses and from 0.45 to 0.49 for K based on line 2 analyses. In the 1200 °C experiments, which are not diffusion limited, the correction is negligible.

Using the corrected β^* values as well as ratios of diffusivities D_j/D_i and the L value relevant to K evaporation at 1400 °C, we were able to use eq 33 to reproduce the K isotopic profile measured by SIMS at 1400 °C (Figure 3B), supporting the view that the evaporation is indeed diffusion limited and that applying a correction to the β-exponent of K is justified.

In situ data are only available for Rb concentration but not isotopic fractionation, which was measured in bulk samples. For sample Bas1400C15m, the Rb content appears to decrease from the center to the rim (Figure 3E), possibly due to the diffusion-limited processes. We modeled the diffusion effect on Rb evaporation on the basis of its chemical profile. Due to the low precision in the measured concentrations and lack of in situ isotopic data for Rb, more work will be needed to ascertain the effect of diffusion on Rb evaporation kinetics and isotopic fractionation. Figure 3D shows that the Rb concentration gradient can be reasonably fit using a L value of 0.5 at 1400 °C. The weight function w is estimated to be 0.906 for Rb at 1400 °C, and the lowest possible w value is estimated to be ~0.912 at 1200 °C. Using the same method as for K, we estimate that ζ must be ~0.04 for Rb. We thus revise the β-exponent in the 1400 °C experiment from 0.44 to 0.49. At 1200 °C, evaporation of Rb is not diffusion limited and no correction is needed. The Na chemical profile for 1400 °C can also be reproduced using a L value of 0.5.

The results presented above show that the β-exponent of both K and Rb during evaporation from basaltic melt are consistent within uncertainty with the kinetic limit of 1/2 for the evaporation of monoatoms where the evaporation coefficients are independent of mass. We suggest that the average values of 0.5 for K (this study; Richter et al.;[27] Yu et al.[26]) and 0.49 for Rb

(this study) should be adopted in future modeling of evaporation from silicate liquids.

The values of L given above ($L = \nu R/D$) were obtained by fitting the chemical profiles in the samples. From our experiments, we can independently estimate the product νR. Indeed, the radius R is known by physical examination of the residues, and $\nu = J/C_{surface}$ in eq 6 can be calculated from the evaporation kinetic model in Section 5.3, which numerically outputs the instantaneous evaporation rates. The values of ν and R for all our experiments are compiled in Table 3. Knowing these values, we can calculate the D required to reproduce our chemical profiles by writing $D = \nu R/L$, where L is the value obtained by fitting the concentration profile data. To reproduce the K and Rb profiles at 1400 °C, we would need D_K and D_{Rb} to be $1.0-2.0 \times 10^{-9}$ and 1.05×10^{-9} m^2/s, respectively. The evaporation experiments performed at 1200 °C are not diffusion limited, so we can only estimate the lower limits for their diffusion coefficients. The D values at 1400 °C are plotted in a $\ln D$ vs $1/T$ Arrhenius diagram (Figure 9) together with previous estimates for silicate melts of various compositions from Zhang et al.[118] and Richter et al.[27] As shown, the value that we get for K agrees well with previous studies but the value for Rb is slightly higher. Potassium and rubidium are low-field strength elements that can migrate rapidly, regardless of the melt structure.[118−120] There is a small compositional effect on K and Rb diffusivity, and it mainly arises from the interactions between alkali elements. The diffusivity of heavy alkali elements (K, Rb, Cs) can be reduced when light alkali elements (Na, Li) are present in the melt. We evaluated this mixed alkali effect quantitatively using Ni's model.[119] We find that it could only shift the value of $\ln D_{Rb}$ by 0.6, which is insufficient to explain the slightly higher value observed in this study (Figure 9B). Further work is needed to re-evaluate the question of the diffusivities of alkali elements in silicate melts, notably for Rb.

5.3. Evaporation Kinetics of Na, K, and Rb. Figure 10 shows the measured evaporation rates in basalt melt in mole·cm^{-2}·s^{-1} at 1200 and 1400 °C for different time durations. As discussed in Section 3, for vacuum evaporation, the rate of evaporation is related to the equilibrium vapor pressure through the Hertz-Knudsen equation (eq 2; $J = \gamma P_{eq}/\sqrt{2\pi MRT}$), which
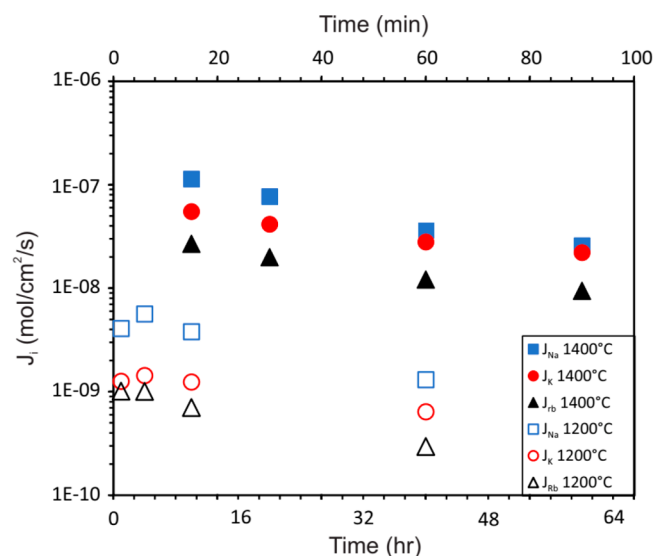
is in turn related to the concentration of the element at the liquid/vapor interface. When evaporation is limited by diffusion, the concentration at the liquid/vapor interface will be lower than the bulk concentration. If this is not taken into account and one uses the bulk concentration to calculate the equilibrium vapor pressure in the Hertz-Knudsen equation, it will result in an overestimation of the evaporation coefficient (assuming that the thermodynamic model used to calculate the activities of melt components is correct). There are two options to address this issue: (i) one can use the measured surface concentration or (ii) one can use the bulk concentration, which is better measured by introducing a diffusion-correction factor. Once the system has reached the quasi-steady state, the concentration of element i at the liquid/vapor interface will scale with the bulk concentration following the relationship $C_{surface}/C_{bulk} = \theta_1^2/3L$. Provided that the activity coefficient does not change dramatically across the molten bead, the equilibrium vapor pressure relevant to the melt/liquid interface P_{eq}^* is related to the equilibrium vapor pressure relevant to the bulk concentration P_{eq} by the same factor $P_{eq}^*/P_{eq} = \theta_1^2/3L$. The evaporation flux is therefore

$$J = \gamma P_{eq}^*/\sqrt{2\pi MRT} = \left(\frac{\theta_1^2}{3L}\right)\gamma P_{eq}/\sqrt{2\pi MRT} \tag{59}$$

where the diffusion-correction factor $\theta_1^2/3L$ can be calculated on the basis of chemical and isotopic diffusion profiles. In this study, the calculated diffusion correction factor at 1400 °C for K is 0.96 when using the profile measured along line 1 and 0.91 if we take the profile along line 2. These calculated diffusion correction factors are close to each other, and the effect on evaporation rate is minimal. The diffusion correction factor for Rb is estimated to be 0.91.

If the equilibrium vapor pressure is independently constrained, we can use eq 59 and combine our measured evaporation rates with the correction factors for diffusion to estimate evaporation coefficients γ. Different thermodynamic models have been used to calculate equilibrium vapor pressures and evaporation coefficients in silicate melts.[11,101,121,122] Ebel and Grossman[11] examined equilibrium condensation from solar gas enriched in dust, conditions under which liquid can be stable. They used two different thermodynamic models to calculate activities in the liquid: a CMAS model (Ca, Mg, Al, Si)[123] and the MELTS model.[85] Fedkin et al.,[101,124] constructed a model based on MELTS[85] to describe previous vacuum evaporation experiments, retrieve evaporation coefficients, and model evaporation/condensation processes during chondrule formation. Richter et al.[27] used the same thermodynamic models as Ebel and Grossman[11] to model their Na and K data. Alexander[121,122] used two different approaches to describe evaporation from chondritic liquids investigated in previous experiments:[26,113] one is the equilibrium reference (EQR) model combined with CMAS and the MELTS model, similar to the models mentioned above, and the other is the pure component reference (PCR) model. The latter one calculates the maximum evaporation rates of pure oxides and rescales this rate to the free evaporation rates measured in silicate melts. Unlike other models discussed above, the calculation of equilibrium vapor pressures from the silicate melt is not needed in the PCR model.

Below, we present the thermodynamic framework that we use for modeling Na, K, and Rb evaporation in the experiments. This framework is very similar to those previously used by Ebel and Grossman,[11] Alexander,[121,122] Fedkin et al.,[101,124] and Richter.[27]

Figure 10. Averaged evaporation rates in moles per cm^2 per second for different duration runs from the experiments at 1400 and 1200 °C.

Note that we do not examine the vapor speciation of these elements as numerous previous studies have shown through equilibrium thermodynamics calculations and measurements from Knudsen cell mass spectrometry that monatomic speciation dominates.[97,125−127] The evaporation reaction of K (or Rb) is written as

$$KAlSiO_{4(l)} \rightleftarrows K_{(g)} + 0.5Al_2O_{3(l)} + SiO_{2(l)} + 0.25O_{2(g)} \tag{R1}$$
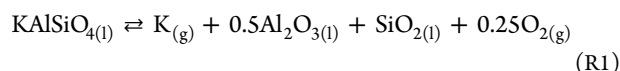
The MELTS model uses $KAlSiO_4$ as the K-bearing component. The equilibrium constant (K_1) of K evaporation reaction R1 is

$$K_1 = \frac{P_{K,eq}P_{O_2}^{1/4}(a_{Al_2O_3})^{1/2}a_{SiO_2}}{a_{KAlSiO_4}} \tag{60}$$

The activities of $KAlSiO_4$, Al_2O_3, and SiO_2 in the silicate liquid are given by the MELTS model.[85] The equilibrium constant for K_1 is calculated from the thermodynamic properties of these species.[128] In all our samples, the atomic ratio Al/(K + Rb) is always higher than 1, so using $KAlSiO_4$ as the K-bearing component is not violating any stoichiometry constraint. By rearranging eq 60, we obtain the equilibrium vapor pressure of K in the melt.

$$P_{K,eq} = \frac{1}{P_{O_2}^{1/4}}\frac{a_{KAlSiO_4}K_1}{(a_{Al_2O_3})^{1/2}a_{SiO_2}} \tag{61}$$

Many studies use $KO_{0.5}$ as the K-bearing component in the melt and report activity coefficients for this component.[1,126,129,130] Using eq 61 and the MELTS model, we can calculate the equilibrium vapor pressure for K(g), which we can then use to calculate the activity coefficient of $KO_{0.5}$, taking $KO_{0.5}$ as the solute species in the liquid melt. With this component, the evaporation reaction is written as

$$KO_{0.5(l)} \rightleftarrows K_{(g)} + 0.25O_{2(g)} \tag{R2}$$
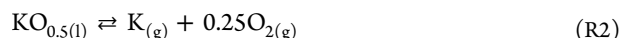
The virtue of using this component is that the vapor pressure becomes a simple function of the oxygen fugacity, but because $KAlSiO_4$ is a better model component of K-speciation in silicate melt, using $KO_{0.5}$ can lead to a more complex activity model that becomes more sensitive to the liquid composition. The equilibrium constant for reaction R2 is expressed as

$$K_2 = \frac{P_K P_{O_2}^{1/4}}{a_{KO_{0.5}}} \tag{62}$$

On the basis of the calculated vapor pressure for K from eq 61, we can derive the activity of $KO_{0.5}(l)$ in silicate melt

$$a_{KO_{0.5}} = \frac{P_K P_{O_2}^{1/4}}{K_2} = \frac{K_1}{K_2}\frac{a_{KAlSiO_4}}{(a_{Al_2O_3})^{1/2}a_{SiO_2}} = \Gamma_{KO_{0.5}}X_{KO_{0.5}} \tag{63}$$

where Γ is the activity coefficient that relates activity a to mole fraction X. Activity coefficients are usually denoted as γ, but this can be confusing as it is the same notation that is used in this contribution for evaporation coefficients; thus, we use the symbol Γ instead. The equilibrium vapor pressure of K can be expressed as

$$P_{K,eq} = \frac{K_2\Gamma_{KO_{0.5}}X_{KO_{0.5}}}{P_{O_2}^{1/4}} \tag{64}$$

A similar approach was applied for Na using the activity from MELTS and thermodynamic constants from thermodynamic data sets (e.g., JANAF[128]) to calculate the equilibrium vapor pressure. We first relate the Na vapor fugacity to the activity of $Na_2SiO_4(l)$ in the melt as given by the MELTS software through the reaction

$$Na_2SiO_{3(l)} \rightleftarrows 2Na(g) + SiO_2(l) + 0.5O_2(g) \tag{R3}$$
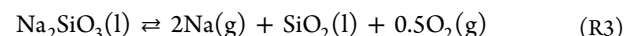
The equilibrium constant for reaction R3 is expressed as

$$K_3 = \frac{P_{Na}^2 P_{O_2}^{1/2}a_{SiO_2}}{a_{Na_2SiO_3}} \tag{65}$$

The activities of Na_2SiO_3 and SiO_2 are computed by MELTS. Accordingly, we can write the equilibrium vapor pressure of Na as

$$P_{Na,eq} = \frac{1}{P_{O_2}^{1/4}}\sqrt{\frac{a_{Na_2SiO_3}K_3}{a_{SiO_2}}} \tag{66}$$

where K_3 is the equilibrium constant for reaction R3 calculated from the JANAF table,[128] and $a_{Na_2SiO_3}$ and a_{SiO_2} are the activities computed by the MELTS software.[85] The activity of $NaO_{0.5}$ is also calculated following a similar procedure as $KO_{0.5}(l)$.

$$NaO_{0.5}(l) \rightleftarrows Na(g) + 0.25O_2(g) \tag{R4}$$
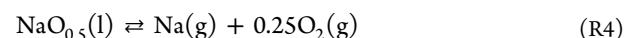
The equilibrium constant for reaction R4 is expressed as
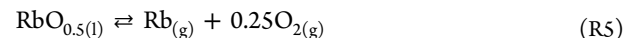
$$K_4 = \frac{P_{Na}P_{O_2}^{1/4}}{a_{NaO_{0.5}}} \tag{67}$$

Thus, the activity of $NaO_{0.5}$ is expressed as

$$a_{NaO_{0.5}} = \frac{P_{Na}P_{O_2}^{1/4}}{K_4} = \frac{1}{K_4}\sqrt{\frac{a_{Na_2SiO_3}K_3}{a_{SiO_2}}} = \Gamma_{NaO_{0.5}}X_{NaO_{0.5}} \tag{68}$$

The partial pressure of Na can also be expressed as

$$P_{Na,eq} = \frac{K_4\Gamma_{NaO_{0.5}}X_{NaO_{0.5}}}{P_{O_2}^{1/4}} \tag{69}$$

For Rb, the evaporation reaction is written as

$$RbO_{0.5(l)} \rightleftarrows Rb_{(g)} + 0.25O_{2(g)} \tag{R5}$$

Where the equilibrium constant is expressed as

$$K_5 = \frac{P_{Rb}P_{O_2}^{1/4}}{a_{RbO_{0.5}}} \tag{70}$$

The MELTS model does not incorporate Rb. We thus assume that the activity coefficients of $KO_{0.5}$ and $RbO_{0.5}$ are identical.

$$\Gamma_{RbO_{0.5}} = \Gamma_{KO_{0.5}} = \frac{K_1}{X_{KO_{0.5}}K_2}\frac{a_{KAlSiO_4}}{a_{Al_2O_3}^{1/2}a_{SiO_2}} \tag{71}$$

The equilibrium vapor pressure of Rb(g) is thus expressed as

$$P_{Rb,eq} = \frac{K_5 a_{RbO_{0.5}}}{P_{O_2}^{1/4}} = \frac{K_5\Gamma_{RbO_{0.5}}}{P_{O_2}^{1/4}}X_{RbO_{0.5}}$$

$$= \frac{K_1 K_5}{P_{O_2}^{1/4}K_2}\frac{a_{KAlSiO_4}}{a_{Al_2O_3}^{1/2}a_{SiO_2}}\frac{X_{RbO_{0.5}}}{X_{KO_{0.5}}} \tag{72}$$

As shown above, the equilibrium vapor pressure of alkalis is related to the oxygen fugacity (fO_2) or oxygen equilibrium vapor pressure (at the pressures considered here, $P_{O_2,eq} \simeq fO_2$). The Fe^{3+}/Fe_{total} ratio measured in the evaporation residues varies between 0.36 and 0.49, corresponding to an oxygen fugacity of IW +6.2 to +7.4.[85] Knowing the change in Fe^{3+}/Fe_{total} ratio and chemical composition before and after the experiments, we calculate O_2 evaporation rates of ~9.2×10^{-10} and ~3.7×10^{-8} mole·cm^{-2}·s^{-1} at 1200 and 1400 °C, respectively. The O_2 evaporation rate is related to the oxygen fugacity through the Hertz-Knudsen equation $J_{O_2} = \gamma_{O_2} P_{O_2,eq}/\sqrt{2\pi M_{O_2} RT}$. Using a reasonable evaporation coefficient for O_2 of 0.1 to 1,[27,88,89,91,92] we would predict O_2 evaporation rates at ~IW +6.8 of ~5.1×10^{-6} and ~5.4×10^{-5} mole·cm^{-2}·s^{-1} at 1200 and 1400 °C, respectively, which is much higher than the values that we measured at the same temperatures. To rephrase, the high measured Fe^{3+}/Fe_{total} ratio in the residues should have sustained a high escape flux of O_2 and a rapid reduction of Fe^{3+} into Fe^{2+}, which is not seen in the experiments. Most likely, the escape rate of oxygen was not limited by evaporation but by the kinetics of Fe reduction and transport in the melt, specifically the inward diffusion of Fe^{2+} and outward diffusion of Fe^{3+}. This hypothesis is supported by the slow kinetics of Fe reduction in silicate melts documented in gas-mixing furnace[131] and pistol cylinder[132,133] experiments. The high initial oxygen fugacity drove the rapid loss of O_2, which reduced Fe^{3+} into Fe^{2+} at the surface of the sample, but the slow diffusion of Fe^{3+} and Fe^{2+} [118] was unable to sustain this initial high escape rate of O_2. The Fe^{3+}/Fe_{total} ratio at the surface thus decreased until fO_2 was set at ~IW + 4 by the evaporation of alkali elements. A piece of evidence supporting this conclusion is the observation that the ratios of measured alkali to O_2 evaporation rates $(J_{Na} + J_K + J_{Rb})/J_{O_2}$ are ~3.7 ± 0.2 and 4.2 ± 0.3 at 1200 °C and ~4.5 ± 0.6 at 1400 °C. These values are close to the stoichiometric ratio of 4 expected for the vaporization reaction of alkali elements $AO_{0.5} \rightarrow A + 1/4 O_2$ (A stands for alkali element; reactions R2, R4, and R5) if the evaporation coefficient of A and O_2 are similar. We therefore adopted the fO_2 calculated from the dissociation of alkali element oxide from silicate melts. Accordingly, the partial pressure of oxygen can be calculated as

$$P_{O_2} = 0.25(P_{Na,eq} + P_{K,eq} + P_{Rb,eq}) \tag{73}$$

which can also be written as

$$P_{O_2} = 0.25\left(\frac{K_2 \Gamma_{KO_{0.5}}}{P_{O_2}^{1/4}} X_{NaO_{0.5}} + \frac{K_4 \Gamma_{NaO_{0.5}}}{P_{O_2}^{1/4}} X_{NaO_{0.5}} + \frac{K_5 \Gamma_{RbO_{0.5}}}{P_{O_2}^{1/4}} X_{RbO_{0.5}}\right) \tag{74}$$

We solve this equation for P_{O_2} and get

$$P_{O_2} = 0.25^{4/5}$$
$$(K_2 \Gamma_{KO_{0.5}} X_{KO_{0.5}} + K_4 \Gamma_{NaO_{0.5}} X_{NaO_{0.5}} + K_5 \Gamma_{RbO_{0.5}} X_{RbO_{0.5}})^{4/5} \tag{75}$$

On the basis of eqs 73−75, we calculate that the oxygen fugacity would have changed from IW + 3.7 to IW + 2.6 in the 1400 °C run and from IW + 4.6 to IW + 2.2 in the 1200 °C run. The calculated oxygen fugacities are similar to values reported by Fedkin et al.[101] (IW +4.2−3.4) and Alexander[121] (IW + 4.3−

3.6), who modeled earlier experiments[26] of free evaporation of alkali elements at 1450 °C from a chondritic liquid using a similar approach.

We can now reinject this relationship into eqs 64, 69, and 72 to calculate the equilibrium vapor pressures of all gas species $P_{K,eq}$, $P_{Na,eq}$, and $P_{Rb,eq}$.

$$P_{K,eq}$$
$$= \frac{K_2 \Gamma_{KO_{0.5}} X_{KO_{0.5}}}{0.25^{1/5}(K_2 \Gamma_{KO_{0.5}} X_{KO_{0.5}} + K_4 \Gamma_{NaO_{0.5}} X_{NaO_{0.5}} + K_5 \Gamma_{RbO_{0.5}} X_{RbO_{0.5}})^{1/5}} \tag{76}$$

$$P_{Na,eq}$$
$$= \frac{K_4 \Gamma_{NaO_{0.5}} X_{NaO_{0.5}}}{0.25^{1/5}(K_2 \Gamma_{KO_{0.5}} X_{KO_{0.5}} + K_4 \Gamma_{NaO_{0.5}} X_{NaO_{0.5}} + K_5 \Gamma_{RbO_{0.5}} X_{RbO_{0.5}})^{1/5}} \tag{77}$$

$$P_{Rb,eq}$$
$$= \frac{K_5 \Gamma_{RbO_{0.5}} X_{RbO_{0.5}}}{0.25^{1/5}(K_2 \Gamma_{KO_{0.5}} X_{KO_{0.5}} + K_4 \Gamma_{NaO_{0.5}} X_{NaO_{0.5}} + K_5 \Gamma_{RbO_{0.5}} X_{RbO_{0.5}})^{1/5}} \tag{78}$$

The free evaporation fluxes of K, Rb, and Na per unit time and unit surface area can then be calculated using eq 59 and the bulk molar fractions $X_{KO_{0.5}}$, $X_{RbO_{0.5}}$, and $X_{NaO_{0.5}}$. Because we use bulk rather than surface concentrations and some of the experiments were diffusion limited, we need to apply the diffusion correction factor described in Section 5.1.

$$J_K = \frac{\theta_{1,K}^2}{3L_K} \frac{\gamma_K \Gamma_{KO_{0.5}}}{\sqrt{2\pi M_K RT}} \frac{K_2 X_{KO_{0.5}}}{(fO_2)^{1/4}} = \frac{\theta_{1,K}^2}{3L_K} \frac{\gamma_K \Gamma_{KO_{0.5}}}{\sqrt{2\pi M_K RT}}$$
$$\frac{K_2 X_{KO_{0.5}}}{0.25^{1/5}(K_2 \Gamma_{KO_{0.5}} X_{KO_{0.5}} + K_4 \Gamma_{NaO_{0.5}} X_{NaO_{0.5}} + K_5 \Gamma_{RbO_{0.5}} X_{RbO_{0.5}})^{1/5}} \tag{79}$$

$$J_{Na} = \frac{\theta_{1,Na}^2}{3L_{Na}} \frac{\gamma_{Na} \Gamma_{NaO_{0.5}}}{\sqrt{2\pi M_{Na} RT}} \frac{K_4 X_{NaO_{0.5}}}{(fO_2)^{1/4}} = \frac{\theta_{1,Na}^2}{3L_{Na}} \frac{\gamma_{Na} \Gamma_{NaO_{0.5}}}{\sqrt{2\pi M_{Na} RT}}$$
$$\frac{K_4 X_{NaO_{0.5}}}{0.25^{1/5}(K_2 \Gamma_{KO_{0.5}} X_{KO_{0.5}} + K_4 \Gamma_{NaO_{0.5}} X_{NaO_{0.5}} + K_5 \Gamma_{RbO_{0.5}} X_{RbO_{0.5}})^{1/5}} \tag{80}$$

$$J_{Rb} = \frac{\theta_{1,Rb}^2}{3L_{Rb}} \frac{\gamma_{Rb} \Gamma_{RbO_{0.5}}}{\sqrt{2\pi M_{Rb} RT}} \frac{K_5 X_{RbO_{0.5}}}{(fO_2)^{1/4}} = \frac{\theta_{1,Rb}^2}{3L_{Rb}} \frac{\gamma_{Rb} \Gamma_{RbO_{0.5}}}{\sqrt{2\pi M_{Rb} RT}}$$
$$\frac{K_5 X_{RbO_{0.5}}}{0.25^{1/5}(K_2 \Gamma_{KO_{0.5}} X_{KO_{0.5}} + K_4 \Gamma_{NaO_{0.5}} X_{NaO_{0.5}} + K_5 \Gamma_{RbO_{0.5}} X_{RbO_{0.5}})^{1/5}} \tag{81}$$

The instantaneous evaporation rates (J_i) as described above cannot be directly measured from the experiments. The evaporation rates calculated from the concentration of the residues (Figure 10) reflect the time-integrated evaporation rate $\int_0^t J_i \, dt/t$. We model evaporation kinetics numerically following previous studies.[11,101,121,122] The activities of alkali elements, oxygen fugacity, and equilibrium vapor pressures were calculated at different time steps to estimate the instantaneous evaporation rate. By fitting the modeled fraction of remaining alkali versus time to the experimental results, we can retrieve the evaporation coefficients from the experiments.

We used the MELTS model[85] to calculate the activities of $KAlSiO_4$, Al_2O_3, SiO_2, and Na_2SiO_3 and the activity coefficients $\Gamma_{KO_{0.5}}$, $\Gamma_{NaO_{0.5}}$, and $\Gamma_{RbO_{0.5}}$ in the residual liquid. The activity
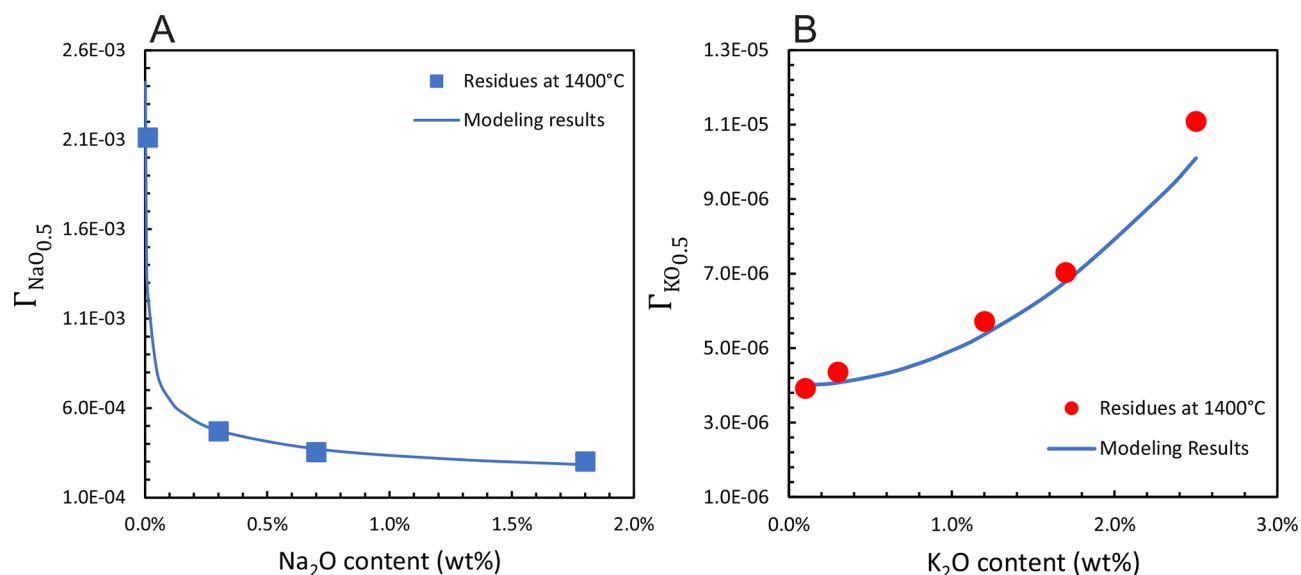
Figure 11. MELTS calculated activity coefficients for $NaO_{0.5}$ and $KO_{0.5}$ in evaporated residues of evolving compositions during evaporation at 1400 °C (the data points are the predicted activity coefficients for the measured melt residues). The sharp increase in the activity of $NaO_{0.5}$ is most likely an artifact from the use of MELTS outside of its application range.[121] For $KO_{0.5}$ and $NaO_{0.5}$, we have therefore used the activity coefficients calculated for a typical MORB composition and have applied these coefficients to all melts for calculating evaporation coefficients. As discussed in the text, this is largely inconsequential as the quantity that matters is the product $\gamma\Gamma$, which is well constrained from our experiments independently of uncertainties in the activity model.
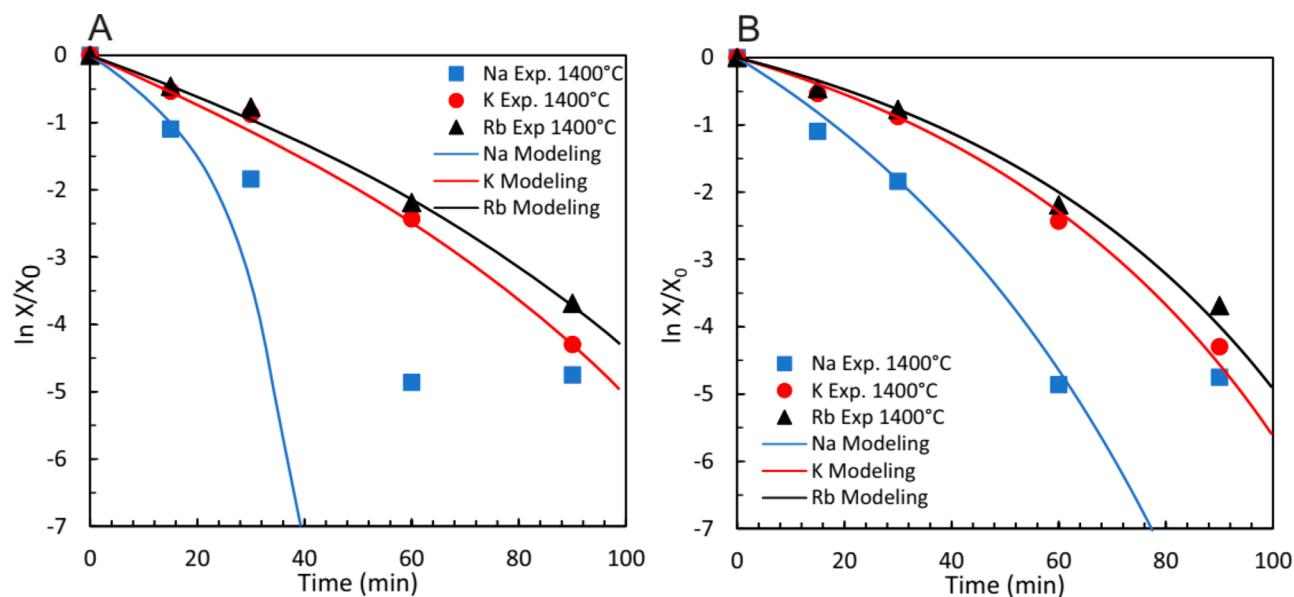
Figure 12. Modeled and measured fractions f of alkali elements (in natural log scale) evaporated at 1400 °C as a function of time (A) using the activity coefficients Γ calculated from MELTS and keeping the evaporation coefficient γ constant in Figure 11 and (B) with $\gamma\Gamma$ (Table 3) kept constant through the whole evaporation.

coefficient $\Gamma_{NaO_{0.5}}$ increases dramatically from 0.0003 to 0.002 when the Na concentration decreases from 1.8 to 0.3 wt %. The activity coefficient $\Gamma_{KO_{0.5}}$ decreases from 1.1×10^{-5} to 4.0×10^{-6} when the K concentration decreased from 2.3 to 0.1 wt % (Figure 11). As shown in Figure 12A, the numerical model based on MELTS cannot explain the experimental data for Na using the variable activity coefficient $\Gamma_{NaO_{0.5}}$ (Figure 11A), unless the Na evaporation coefficient (γ_{Na}) decreased as Na evaporation proceeded in a manner that balanced the apparent increase in $\Gamma_{NaO_{0.5}}$ with decreasing Na concentration. Alexander[121] argued that this behavior of the activity coefficient of Na in MELTS was

most likely incorrect, and we concur with this assessment. In Figure 12B, we model the evaporation trajectory for Na, K, and Rb as a function of time using a constant value for the product $\gamma_{Na}\Gamma_{NaO_{0.5}}$ (eq 80). The modeling results fit well with the experimental data. This means that the product of the evaporation and activity coefficients $\gamma\Gamma$ must be constant. If the activity of $NaO_{0.5}$ was indeed increasing with decreasing Na concentration, this would imply that the evaporation coefficient would have to vary inversely to maintain the product $\gamma_{Na}\Gamma_{NaO_{0.5}}$ at a constant value, which is highly implausible. Most likely, both γ and Γ remain approximately constant during the evaporation,

Table 2. Compiled Thermodynamic Quantities and Calculated Evaporation and Activity Coefficients

data source[a]	T (°C)	Na$_2$SiO$_3$ (l)	SiO$_2$ (l)	Na$_2$O (l)	Na (g)	O$_2$ (g)	ΔG for R3	K$_3$	ΔG for R4	K$_4$	$\Gamma_{NaO_{0.5}}$	γ_{Na}
1	1200	−1 897 300	−1 042 108	−631 061[b]	−143 555[b]	−339 548[b]	224 131	1.1×10^{-8}	87 089	8.16×10^{-4}	4.11×10^{-5}	0.08
2	1200	−1 900 181	−1 042 444	−631 061	−143 555	−339 548	226 676	9.2×10^{-9}	87 089	8.16×10^{-4}	3.70×10^{-5}	0.09
3	1200	−1 894 985	−1 042 444[c]	−628 472	−142 834	−339 601	224 069	1.1×10^{-8}	86 502	8.56×10^{-4}	4.12×10^{-5}	0.08
1	1400	−1 977 220	−1 072 774	−684 147[b]	−181 197[b]	−391 541[b]	220 299	1.3×10^{-7}	62 992	1.08×10^{-2}	1.94×10^{-4}	0.13
2	1400	−1 980 936	−1 072 757	−684 147	−181 197	−391 541	224 032	1.0×10^{-7}	62 992	1.08×10^{-2}	1.70×10^{-4}	0.15
3	1400	−1 975 807	−1 072 757[c]	−681 626	−180 480	−391 537	221 423	1.2×10^{-7}	62 448	1.12×10^{-2}	1.87×10^{-4}	0.14

	T (°C)	KAlSiO$_4$ (l)	K$_2$O(cr)[e]	SiO$_2$ (l)	Al$_2$O$_3$ (l)	K (g)	O$_2$ (g)	ΔG for R1	K$_1$	ΔG for R2	K$_2$	$\Gamma_{KO_{0.5}}$	γ_K
1	1200	−2 478 695	−616 539[b]	−1 042 108	−1 840 448	−171 672[b]	−339 548[b]	416 187	1.7×10^{-15}	51 710	1.47×10^{-2}	1.11×10^{-6}	0.06
2	1200	−2 478 695[d]	−616 539	−1 042 444	−1 844 916	−171 672	−339 548	411 046	2.7×10^{-15}	51 710	1.47×10^{-2}	1.37×10^{-6}	0.05
3	1200	−2 478 695	−614 649	−1 042 444[c]	−1 844 916[c]	−171 534	−339 601	412 936	2.3×10^{-15}	50 890	1.57×10^{-2}	1.27×10^{-6}	0.05
1	1400	−2 562 230	−669 941[b]	−1 072 774	−1 895 135	−210 646[b]	−391 541[b]	413 836	1.2×10^{-13}	26 439	1.49×10^{-1}	8.18×10^{-6}	0.14
2	1400	−2 562 230[d]	−669 941	−1 072 757	−1 897 765	−210 646	−391 541	411 239	1.4×10^{-13}	26 439	1.49×10^{-1}	8.98×10^{-6}	0.12
3	1400	−2 562 230	−668 097	−1 072 757[c]	−1 897 765[c]	−210 517	−391 537	413 083	1.3×10^{-13}	25 647	1.58×10^{-1}	8.41×10^{-6}	0.13

	T (°C)	Rb$_2$O (l)	Rb (g)	O$_2$ (g)	ΔG for R5	K$_5$	$\Gamma_{RbO_{0.5}}$	γ_{Rb}
2	1200	−648 947[d]	−194 156	−339 601	45 417	2.45×10^{-2}	1.37×10^{-6}	0.07
3	1200	−648 947	−194 186	−339 548	45 401	2.46×10^{-2}	1.27×10^{-6}	0.07
2	1400	−710 289[d]	−235 083	−391 541	22 176	2.03×10^{-1}	8.98×10^{-6}	0.17
3	1400	−710 289	−235 116	−391 537	22 144	2.04×10^{-1}	8.41×10^{-6}	0.18

[a]Data sources: (1) Berman;[123] (2) JANAF table;[128] (3) Knacke et al.[134] [b]Thermodynamic data are not included in Berman,[123] and we used JANAF[128] instead. [c]Thermodynamic data are not included in Knacke et al.,[134] and we used JANAF[128] instead. [d]Thermodynamic data are not included in the JANAF table,[128] and we used Knacke et al.[134] instead. [e]The Gibbs free energy of crystalline KO$_{0.5}$ was used because this quantity is unknown for KO$_{0.5}$ liquid (also see Alexander[121]).

and the spurious behavior of Na is due to the fact that the MELTS model is applied outside its range of applicability. Indeed, MELTS is best suited to model terrestrial magmas. In the calculation, we have therefore adopted constant activity coefficients for a normal MORB composition[82] at 1200 and 1400 °C for $KAlSiO_4$ and Na_2SiO_3. For the other species, we use the activities given by the MELTS model using the actual concentrations because these fall in a range that is similar to terrestrial MORBs as we used a synthetic N-MORB composition for these elements. At 1200 °C, we use constant activity coefficients of 4.12×10^{-5} and 1.27×10^{-6} for $NaO_{0.5}$ and $KO_{0.5}-RbO_{0.5}$, respectively. At 1400 °C, we use constant activity coefficients of 1.87×10^{-4} and 8.41×10^{-6} for $NaO_{0.5}$ and $KO_{0.5}-RbO_{0.5}$, respectively. The calculated activity and evaporation coefficients are summarized in Table 4. We should note again that the evaporation coefficients calculated in such a manner are extremely sensitive to the quality of thermodynamic data and models used.

The thermodynamic data for the chemical compounds are from the JANAF database[128] and Knacke et al.[134] The thermodynamic properties of the minerals in MELTS are mostly from Berman[123] and were later updated by Ghiorso and Sack.[85] The thermodynamic data for chemical components and equilibrium constants for evaporation reactions R1, R2, R3, R4, and R5 are listed in Table 2. We have carefully examined the effect of the thermodynamic quantities from the different databases on the calculated evaporation coefficients. The results are consistent, and the effect on the calculated evaporation coefficients is small.

We obtained best-fit values for γ_{Na}, γ_K, and γ_{Rb} at 1200 °C of 0.078, 0.054, and 0.07 respectively. The best-fit values of γ_{Na}, γ_K, and γ_{Rb} at 1400 °C are 0.14, 0.132, and 0.17, respectively. As discussed above, the activity coefficients of Na, K, and Rb are uncertain. The product of the activity coefficients of those elements in the melt and their evaporation coefficients may be more robustly constrained.[29] Indeed, it is the product $\gamma\Gamma$ that influences the evaporation rate in eqs 79−81. At 1200 °C, we obtain for $\gamma_{Na}\Gamma_{NaO_{0.5}}$, $\gamma_K\Gamma_{KO_{0.5}}$, and $\gamma_{Rb}\Gamma_{RbO_{0.5}}$ values of 3.2×10^{-6}, 6.9×10^{-8}, and 8.4×10^{-8}, respectively. At 1400 °C, we obtain for $\gamma_{Na}\Gamma_{NaO_{0.5}}$, $\gamma_K\Gamma_{KO_{0.5}}$, and $\gamma_{Rb}\Gamma_{RbO_{0.5}}$ values of 2.62×10^{-5}, 1.11×10^{-6}, and 1.44×10^{-6}, respectively.

Evaporation coefficients from the literature cover a large range of values from 0.07 to 0.3 for both K and Na. For comparison, we have calculated the product $\gamma\Gamma$ for previous evaporation experiments. The experiments of Yu et al.[26] yield $\gamma_{Na}\Gamma_{NaO_{0.5}} = 2.95 \times 10^{-5}$ and $\gamma_K\Gamma_{KO_{0.5}} = 1.56 \times 10^{-6}$ for evaporation of chondritic composition at 1450 °C. The experiments of Richter et al.[27] yield $\gamma_{Na}\Gamma_{NaO_{0.5}} = 2.96 \times 10^{-5}$ and $\gamma_{Na}\Gamma_{NaO_{0.5}} = 1.10 \times 10^{-6}$ for evaporation of chondritic composition at 1470 °C. In Figure 13, we plot the natural logarithm of $\gamma\Gamma$ as a function of $1/T$ from our experiments as well as those of Yu et al.,[26] Richter et al.,[27] and Sossi et al.[29] As shown, this plot reveals linear relationships between these two quantities. The equations governing the best-fit lines are $\ln(\gamma_{Na}\Gamma_{NaO_{0.5}}) = -22239/T + 2.4979$ for Na, $\ln(\gamma_K\Gamma_{KO_{0.5}}) = -29265/T + 3.4593$ for K, and $\ln(\gamma_{Rb}\Gamma_{RbO_{0.5}}) = -35020/T + 7.4795$ for Rb with T in Kelvin.

In order to compare our model with previous studies, we also used MELTS to calculate the $NaO_{0.5}$ and $KO_{0.5}$ activity coefficients and estimated the evaporation coefficients for the experimental results reported by Yu et al.[26] and Richter et al.[27] For Na, we get values of 0.11 and 0.10 in these two studies. For
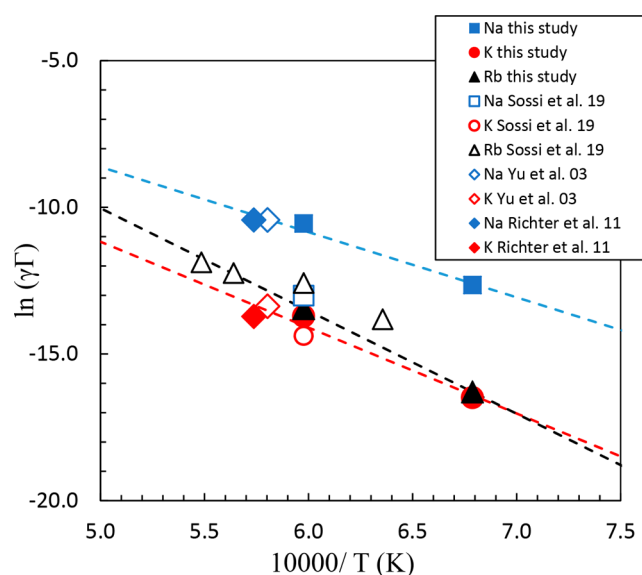
Figure 13. Product of activity coefficients times evaporation coefficients in natural log scale for Na, K, and Rb derived from our experimental results and previous experiments by Yu et al.,[26] Richter et al.,[27] and Sossi et al.[29] The $\gamma\Gamma$ values originally given by Sossi et al.[29] were incorrect, possibly due to an error in unit conversion. We recalculated $\gamma\Gamma$ from their experimental results, and these revised estimates are plotted here.

K, we get values of 0.13 and 0.08 in these two studies. The calculated evaporation coefficients are similar to those calculated from our experiments (0.08−0.14 for $NaO_{0.5}$ and 0.05−0.13 for $KO_{0.5}$). They also agree with values reported in previous studies with values of 0.26 and 0.13 for Na and K given by Fedkin et al.;[101] 0.12 and 0.12 for Na and K given by Alexander;[121] 0.06 and 0.07 given by Richter et al.[27] (Table 4). However, as discussed before, the activity coefficients from MELTS may not be correct, and the calculated "evaporation coefficients" could be inaccurate. The products of activity coefficients and evaporation coefficients are more robust for constraining evaporation kinetics.

We also compare our evaporation kinetics with evaporation experiments performed at 1300−1550 °C and oxygen fugacities of ∼IW to IW + 3 in a 1-bar gas mixing furnace by Sossi et al.[29] Note that Sossi et al.[29] arbitrarily fixed time zero by introducing a "lag time" for interpreting the kinetics of Rb evaporation from some of their experiments, the criterion being the goodness of fit of the molar fraction in the residues (X/X_0) and time, a procedure that can affect the results. The $\gamma\Gamma$ values for Na, K, and Rb from Sossi et al.[29] are all much higher (by factors of 1000) than data from the vacuum experiments (this study, Yu et al.,[26] Richter et al.[27]). We recalculated $\gamma\Gamma$ from their experiments, and the results are similar to this study (Figure 13), suggesting that the higher values reported by Sossi et al.[29] may be due to errors in unit conversions.

5.4. Evaporation Trajectories of Na−K−Rb. The evaporation trajectories for Na−K−Rb are shown in Figures 14 and 15. In our experiments, Na evaporates faster than K, which is consistent with most previous studies.[26−28,32] The relative volatilities of alkali elements are computed by dividing the evaporation rate from the Hertz-Knudsen equation:

$$J_{Na}/J_K = \frac{\gamma_{Na}P_{Na,eq}}{\gamma_K P_{K,eq}} \sqrt{\frac{M_K}{M_{Na}}}$$

$$(82)$$

Table 3. Calculated Parameters for Na, K, and Rb Evaporation and Evaluation of the Degree of Diffusion-Limited Transport in the Experiments[a]

this study	temp (°C)	R (cm)	diffusion correction factor $\theta_1^2/3L$	ν (cm/s)	D (cm^2/s)	L
Na	1400	0.15	0.91	6.6×10^{-5}	1.98×10^{-5}	0.5
K line 1	1400	0.15	0.96	3.0×10^{-5}	2.0×10^{-5}	0.225
K_line 2	1400	0.15	0.91	3.0×10^{-5}	1.0×10^{-5}	0.45
Rb	1400	0.15	0.91	3.5×10^{-5}	1.1×10^{-5}	0.5
Na	1200	0.15	>0.99	1.0×10^{-6}	$>3.0 \times 10^{-6}$	<0.05
K	1200	0.15	>0.99	3.0×10^{-7}	$>1.2 \times 10^{-6}$	<0.0375
Rb	1200	0.15	>0.98	4.5×10^{-7}	$>6.0 \times 10^{-7}$	<0.1125

[a]$L = \nu R/D$; see the text for details.

$P_{i,eq}$ is a function of equilibrium constant, oxygen fugacity, and molar fraction as expressed in eqs 76, 77, and 78. Considering these dependencies, we can rewrite eq 82 as

$$J_{Na}/J_K = \frac{dN_{NaO_{0.5}}}{dN_{KO_{0.5}}} = \frac{K_4 \gamma_{Na} \Gamma_{NaO_{0.5}} X_{NaO_{0.5}}}{K_2 \gamma_K \Gamma_{KO_{0.5}} X_{KO_{0.5}}} \sqrt{\frac{M_K}{M_{Na}}} \quad (83)$$

which can be rearranged and integrated to yield

$$\ln\left(\frac{X_{NaO_{0.5}}}{X_{NaO_{0.5},0}}\right) = \frac{K_4 \gamma_{Na} \Gamma_{NaO_{0.5}} \sqrt{M_K}}{K_2 \gamma_K \Gamma_{KO_{0.5}} \sqrt{M_{Na}}} \ln\left(\frac{X_{KO_{0.5}}}{X_{KO_{0.5},0}}\right) \quad (84)$$

At a given temperature and provided that the evaporation and activity coefficients do not change dramatically during evaporation, the quantity that describes the relative volatilities of Na and K should remain constant

$$\varphi_K^{Na} = \frac{\ln\left(\frac{X_{NaO_{0.5}}}{X_{NaO_{0.5},0}}\right)}{\ln\left(\frac{X_{KO_{0.5}}}{X_{KO_{0.5},0}}\right)} = \frac{K_4 \gamma_{Na} \Gamma_{NaO_{0.5}}}{K_2 \gamma_K \Gamma_{KO_{0.5}}} \sqrt{\frac{M_K}{M_{Na}}} \quad (85)$$

A similar relationship was previously used to model Mg and Si evaporation.[92] At 1400 °C, we can reproduce the data with $\varphi_K^{Na} = 1.6$, while at 1200 °C, we calculate $\varphi_K^{Na} = 3.6$. At both temperatures in our experiments, Na is more volatile than K. Na and K are evaporating as monatomic; thus, $f O_2$ will not affect the relative flux for K and Na. The difference between the 1200 and 1400 °C runs is thus primarily a direct temperature effect on the thermodynamic parameters in eq 85. Shimaoka et al.,[28] Yu et al.,[26] Richter et al.,[27] and Gellissen et al.[32] also found that Na evaporated faster than K in their evaporation experiments (Figure 14). Gellissen et al.[32] used a synthetic mixture of SiO_2–Al_2O_3, Na_2O, K_2O, and MnO as starting material, while Shimaoka et al.,[28] Yu et al.,[26] Richter et al.[27] examined chondritic compositions. The relative volatilities of Na and K in our experiments are however very different from those reported by Kreutzberger et al.,[33] Gibson and Hubbard,[30] and Sossi et al.,[29] who used different starting compositions compared to our terrestrial N-MORB composition doped with Na, K, and Rb or the chondritic compositions used by Shimaoka et al.,[28] Yu et al.,[26] and Richter et al.[27] Kreutzberger et al.[33] used a mixture of 75 mol % diopside/25 mol % anorthite doped with 1 wt % each of Na_2CO_3, K_2CO_3, Rb_2CO_3, and Cs_2CO_3 as starting composition and ran their experiments at a low pressure of $<10^{-3}$ mbar at a temperature of 1400 °C. Gibson and Hubbard[30] used 14163 lunar soils (61% glass, 28% breccia, and 10% of plagioclase and pyroxene) in a vacuum at a temperature of 1050 °C. Sossi et al.[29] used an anorthite/diopside eutectic composition with the addition of 15 wt % each of forsterite and Fe_2O_3. They carried out evaporation experiments at 1400

°C, and several oxygen fugacities were investigated. Their run products showed both higher and lower volatility of Na relative to K. Many parameters can explain the different behaviors of Na and K in those experiments, most notably differences in activities in melts of different compositions[29,30,33] and temperature.[30] However, for chondritic and basaltic compositions under vacuum conditions, all experiments point to the fact that Na evaporates much faster than K (Figure 14; this study; Richter et al.;[27] Yu et al.;[26] Shimaoka et al.;[28] Gellissen et al.[32]).

The parameters γ_{Na}, γ_K, $\Gamma_{NaO_{0.5}}$, $\Gamma_{KO_{0.5}}$, K_3, and K_5 all have some temperature dependence, and we can approximate eq 85 as $\varphi_K^{Na} \simeq a e^{-b/T}$ with a and b as two fit parameters. While evaporation kinetics of individual alkali elements depends on oxygen fugacity, albeit weakly, this dependence is eliminated when taking the ratio of two alkali elements. We have measured φ_K^{Na} at 1200 and 1400 °C and have used the data of Richter et al.,[27] Yu et al.,[26] and Shimaoka et al.[28] to calculate φ_K^{Na} in chondritic compositions for temperatures ranging between 1100 and 1500 °C. In Figure 16A, we plot $\ln(\varphi_K^{Na})$ vs T. As shown, the basaltic and chondritic evaporation experiments all plot on the same line, whose fit yields $\varphi_K^{Na} \simeq 0.0476 e^{6301/T}$ with T in Kelvin.

The evaporation trajectories for K and Rb are very close to the 1:1 line (Figure 15), which shows that they have similar evaporative behavior, consistent with the results of Shimaoka et al.[28] and Gibson and Hubbard.[30] We nevertheless find that Rb is more rapidly lost than K and the departure from the 1:1 line is greater at 1200 than at 1400 °C. At 1200 °C, we can reproduce the data with a ratio of $\varphi_K^{Rb} = \frac{\gamma_{Rb} K_4 \Gamma_{RbO_{0.5}}}{\gamma_K K_5 \Gamma_{KO_{0.5}}} \sqrt{\frac{M_K}{M_{Rb}}} = 1.28$, while at 1400 °C, we calculate $\varphi_K^{Rb} = 1.15$. Shimaoka et al.[28] carried out vacuum evaporation of alkalis at temperatures between 1200 and 1400 °C using powdered matrix material of Murchison (CM2) chondrite as the starting material. The samples were partially molten with olivine phenocrysts present. They found that Rb and K had similar volatilities, consistent with our results. One of their data points at 1200 °C however departed from the trend. Gibson and Hubbard[30] and Gibson et al.[31] carried out vacuum evaporation experiments using powdered lunar rocks and soils, including 12022 ilmenite basalts and soils from Apollo 14 and 16. Their results suggest that K and Rb have similar volatilities between 1200 and 1400 °C (purple triangles in Figure 15), but Rb evaporates much faster than K at lower temperature (950 to 1050 °C, blue triangles and circles in Figure 15). The evaporation experiments carried out for ilmenite basalt at 1200 to 1400 °C define a similar φ_K^{Rb} value as this study of around 1.19. However, evaporation experiments on lunar soil 14163 at 1050 °C define a φ_K^{Rb} value of 1.28, and evaporation experiments on lunar soil 61221 at 1000 °C define a φ_K^{Rb} value of 1.37. These results suggest that Rb tends to evaporate faster than K at lower temperature. A faster evaporation rate of Rb relative

Table 4. Evaporation and Activity Coefficients of Alkali Elements in Silicate Melts and a Comparison with Previous Studies

sample	T (°C)	P (bar)	γ_{Na}	γ_{K}	γ_{Rb}	$\Gamma_{NaO_{0.5}}$	$\Gamma_{KO_{0.5}}$	$\Gamma_{RbO_{0.5}}$	$\gamma_{Na}\Gamma_{NaO_{0.5}}$	$\gamma_{K}\Gamma_{KO_{0.5}}$	$\gamma_{Rb}\Gamma_{RbO_{0.5}}$	source
Bas1400C	1400	$<10^{-9}$	0.14 ± 0.03	0.132 ± 0.1	0.17 ± 0.05	1.87×10^{-4}	8.41×10^{-6}	8.41×10^{-6}	2.62×10^{-5}	1.11×10^{-6}	1.44×10^{-6}	1
Bas1200C	1200	$<10^{-9}$	0.078 ± 0.02	0.054 ± 0.02	0.07 ± 0.02	4.12×10^{-5}	1.27×10^{-6}	1.27×10^{-6}	3.20×10^{-6}	6.90×10^{-8}	8.40×10^{-8}	1
IIAB1	1470	$<10^{-9}$	0.10 ± 0.01	0.08 ± 0.02		2.9×10^{-4}	1.4×10^{-5}		2.96×10^{-5}	1.10×10^{-6}		2, 1[a]
IIAB1	1470	$<10^{-9}$	0.071 ± 0.013	0.061 ± 0.014								2
C1	1450	10^{-5}	0.11 ± 0.01	0.13 ± 0.02		2.6×10^{-4}	1.2×10^{-5}		2.95×10^{-5}	1.56×10^{-6}		3, 1[a]
C1	1450	10^{-5}	0.13 ± 0.02	0.26 ± 0.05								3, 4[a]
C1	1450	10^{-5}	0.12	0.12		$\sim3.5 \times 10^{-4}$	$\sim3.2 \times 10^{-5}$		$\sim4.20 \times 10^{-5}$	3.84×10^{-6}		3, 5[a]
FCMAS	1300	1									1.00×10^{-6}	6, 1[a]
FCMAS	1400	1							2.23×10^{-6}	5.69×10^{-7}	3.44×10^{-6}	6, 1[a]
FCMAS	1500	1									4.83×10^{-6}	6, 1[a]
FCMAS	1550	1									6.95×10^{-6}	6, 1[a]

[a]The values reported are reanalyses of previously published data by us or other publications: (1) this study; (2) Richter et al.,[27] (3) Yu et al.,[26] (4) Fedkin et al.,[101] (5) Alexander;[121] (6) Sossi et al.[29]

to K at low temperature was also reported by Smales et al.[135] during an experiment of volatilization/thermal ionization of several chondrites. As with K and Na, we evaluate the temperature dependence of K and Rb relative evaporations by plotting $\ln \varphi_K^{Rb}$ vs T using our data and the previous results of Gibson and Hubbard,[30] Gibson et al.,[31] and Shimaoka et al.[28] (Figure 16B). We find a linear relationship between the two quantities. Using our well-constrained data alone and considering the fact that evaporation at 1400 °C was slightly affected by diffusion, we obtain a relationship of $\varphi_K^{Rb} \simeq 0.52 e^{1334/T}$ with T in Kelvin. Incorporating the results of Gibson and Hubbard,[30] Gibson et al.,[31] and Shimaoka,[28] we obtain a relationship of $\varphi_K^{Rb} \simeq 0.54 e^{1154/T}$. The compositions investigated thus far cover a large range of compositions (chondritic, basaltic, and lunar soil), and some of them are partially molten; however, we still find a good correlation between $\ln \varphi_K^{Rb}$ and $1/T$ from 1400 down to 950 °C.

5.5. Theoretical Exploration of the Parameter Space and Possible Application to Vesta. The theoretical framework that we have developed to describe the evaporation of minor components from liquid spheres allows us to explore the parameter space and evaluate how changes in temperature, sphere size, and time would affect chemical and isotopic fractionations. In quasi-steady state, the main factors affecting chemical and isotopic profiles are time and $L = \nu R/D$, which is a function of temperature as both ν and D depend on T. For ν_K (cm/s), we can use the parameters that we have derived in Section 5.1 to rewrite eq 6 as

$$\nu_K = J_K/C_K \sim \frac{A}{f O_2^{1/4} \sqrt{T}} e^{-B/RT} \tag{86}$$

where the $f O_2$ is the oxygen fugacity in bar, $A = 1.23 \times 10^{10}$ cm/s, and $B = 464.885$ kJ. A similar equation can be written for Rb with $A = 3.60 \times 10^9$ and $B = 445.921$ kJ. When element transport in the molten sphere is not set by advection, diffusion can influence the rate of evaporation. Its temperature dependence takes the form

$$D = D_0 \exp\left(-\frac{E_a}{RT}\right) \tag{87}$$

where D is the diffusion coefficient (cm²/s), D_0 is the Arrhenius pre-exponent (cm²/s), and E_a is the activation energy (kJ/mol).

We have used this formalism to calculate how the K/Rb ratio would be fractionated during volatilization. The motivation for doing so is that Vesta sampled by HED meteorites is very depleted in moderately volatile elements and its K/Rb ratio is very distinct from other less depleted planetary bodies, begging the question of the context needed to fractionate K and Rb during planetary formation. We apply our model to subliquidus temperatures, bearing in mind that our experiments were all performed above the liquidus and further work is needed to study evaporation from partially crystallized systems.

As pointed out by Lodders[136] and Sossi and Fegley,[137] the degree of depletion of alkali elements in Vesta (from the most to the least depleted) is Cs > Rb > K > Na, which follows equilibrium vapor pressures. If loss had been mediated through transport through an atmosphere, atomic mass would have greatly influenced the escape efficiency. Most likely, Vesta was never able to sustain a bound atmosphere, and elements released by vaporization at its surface would have been lost directly to space. This view is corroborated by consideration of Vesta's
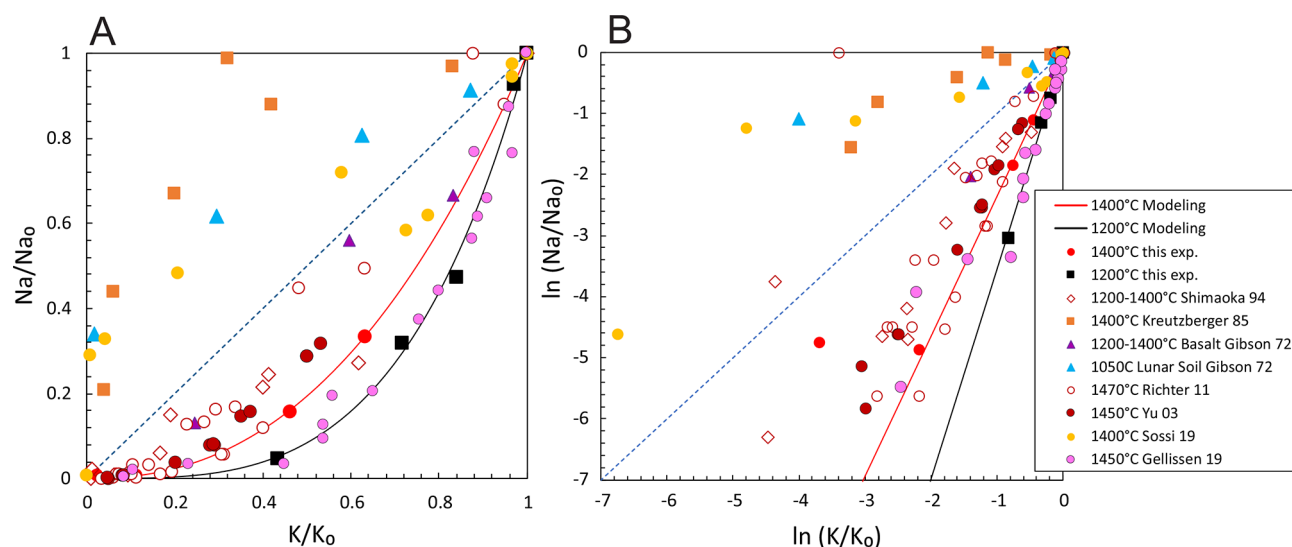
Figure 14. Evaporation trajectories for Na and K in this study with data compiled from the literature:[26−32] (A) in a linear scale; (B) in a natural logarithmic scale.
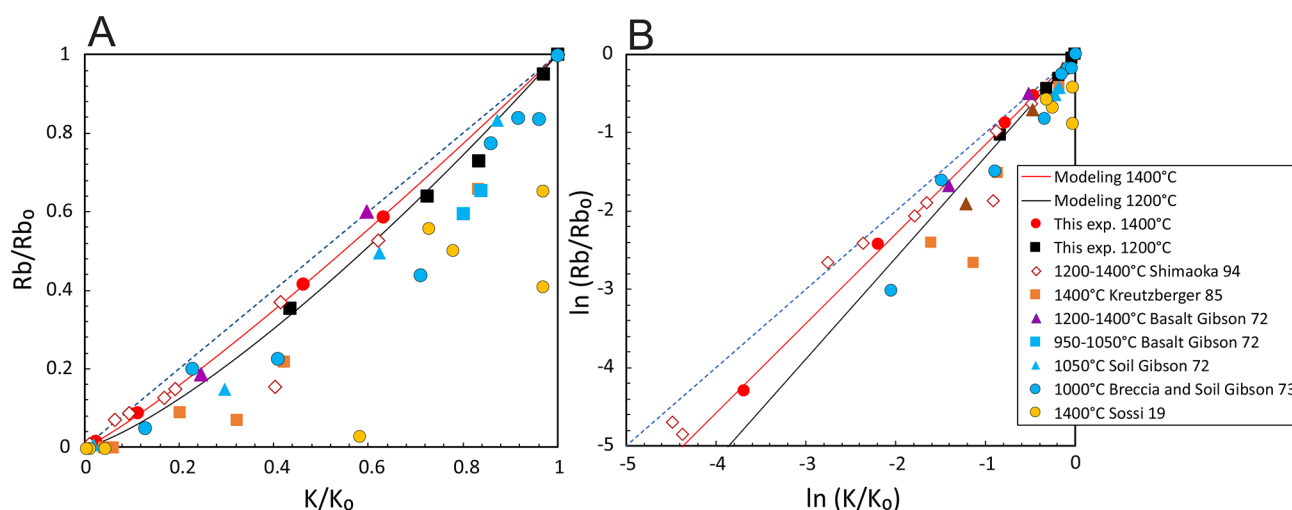
Figure 15. Evaporation trajectories of Rb and K with data compiled from the literature:[28−31,33] (A) in a linear scale; (B) in a natural logarithmic scale.

small radius (262 km). The critical radius for a planetesimal to retain an atmosphere is given by Young et al.:[138]

$$ r_c = \frac{3}{4} \sqrt{\frac{2k_b T}{\pi m_{gas} \rho G}} \tag{88} $$

where k_b is Boltzmann constant, T is temperature (around 1473 K for basalt liquidus), ρ is the rock density ($\sim$3500 kg/m^3), m_{gas} is molar weight, and G is the gravitational constant. The critical radii for sustaining atmospheres of Na, K, and Rb are 900, 749, and 507 km, respectively. These critical radii are all higher than Vesta's radius of 262 km, meaning that atoms released by evaporation would have thermal velocities exceeding the escape velocity. Regardless of whether the loss of K and Rb took place on Vesta or its building blocks, the experiments and formalism described here are applicable.

Two scenarios have been proposed to explain the depletion in MVEs, including K and Rb, in Vesta:

(i) 4-Vesta could have inherited its depletion directly from a depleted source (i.e., chondrules[139]) without involving evaporation. Recently, Tian et al.[52] found a shift of

$\sim$+0.36‰ toward heavy δ^{41}K in HED meteorites compared to Earth and suggested this could be a signature from a chondrule-rich precursor. Chondrules have δ^{41}K values that vary between −15.5‰ and +11.9‰.[62,140−142] However, the K/Rb ratios in either bulk chondrites or chondrules are always smaller than 2,[143,144] so other mechanisms must be at play.

(ii) Another possibility is that K and Rb were lost due to volcanic/magma degassing, where Cl-bearing volcanic gases could form compounds such as KCl or RbCl.[145] A linear correlation for K content and Cl isotopic composition in HED meteorites indeed suggests that volcanic degassing could be involved in the K depletion of Vesta.[146] However, the thermodynamic calculation from Tian et al.[52] indicates that Zn and Cl are much more volatile than K during volcanic degassing, and their calculation suggests that Zn or Cl will be almost completely removed before K starts to be lost, which is inconsistent with observations.[68]

Following the study of Tian et al.,[52] we evaluate the evaporation of millimeter to centimeter (droplet) sized objects
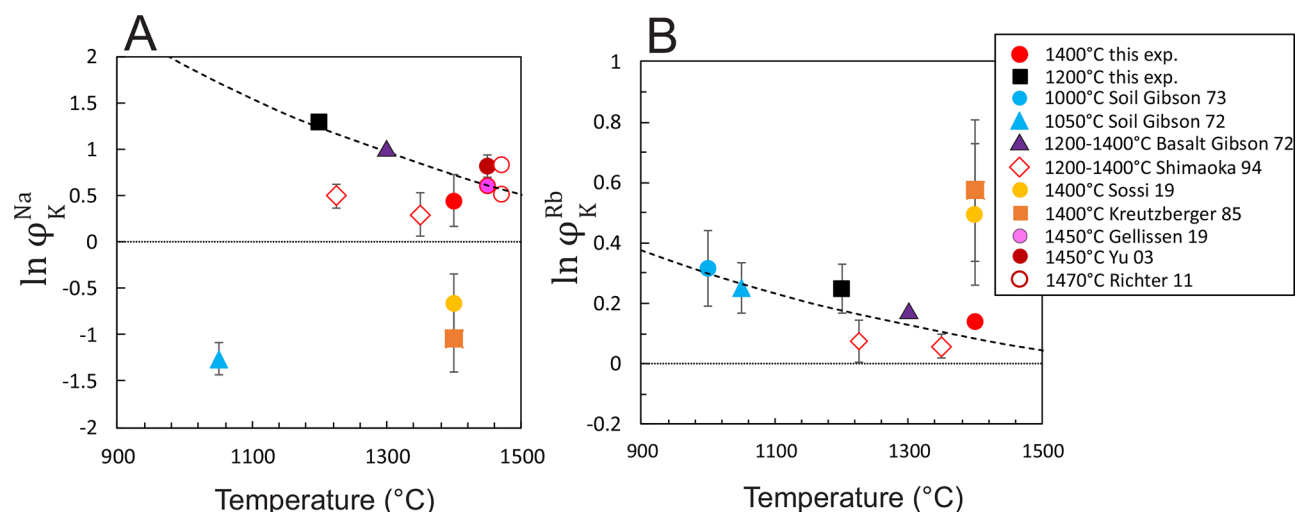
Figure 16. Relative volatilities (expressed as $\varphi_j^i = (\gamma_i K_i \Gamma_i \sqrt{M_j})/(\gamma_j K_j \Gamma_j \sqrt{M_i})$; see Section 5.4) of Na/K (A) and Rb/K (B) as a function of temperature. (A) The dashed line is a linear fit of $\ln \varphi_K^{Na}$ vs $1/T$ from the data of this study and Richter et al.[27] (B) The dashed line is a linear fit for Rb and K from data of this study, Shimaoka et al.,[28] Gibson et al.,[31] and Gibson and Hubbard.[30] The data from Sossi et al.[29] and Kreutzberger et al.[33] are also plotted for comparison, but they are not used in the fits.
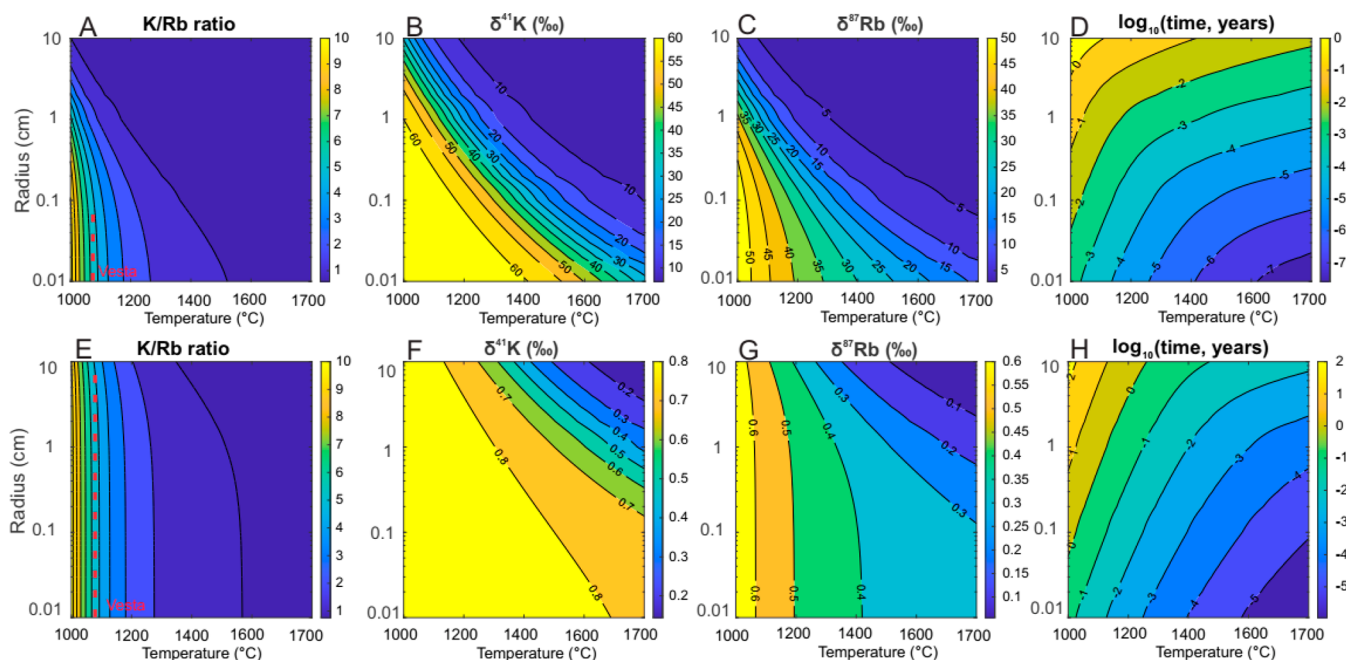
Figure 17. Color contour plot showing the K/Rb ratio (normalized to starting composition), the $\delta^{41}K$ and $\delta^{87}Rb$ isotopic compositions (relative to the starting composition), and the time scale for evaporating 94% of K under vacuum conditions (A−D) and at $S = 0.988$ saturation degree (E−H) as a function of temperature and sphere size. The ∼6 times larger K/Rb ratio relative to H chondrites inferred for requires evaporation at low temperature (A and E) and its relatively moderate isotopic fractionation of $\delta^{41}K = 0.84‰$ and $\delta^{87}Rb = 0.6‰$ excludes evaporation in the vacuum (B and C) and requires evaporation in medium at $S = 0.988$ saturation (F and G). If evaporation took place from chondrule-size objects (0.01−1 cm), the time needed to achieve 94% loss of K is 0.1 to 10 years (H).

as a possible explanation for the depletion in K and Rb in 4-Vesta. It is worth noting that the evaporation of droplet-size objects described here is not necessarily related to chondrule formation. Chondrules can be highly depleted in MVEs, but they lack systematic isotopic fractionation expected from free evaporation.[62,140,141] They could be produced by nebular shocks, radiative heating, lightning, or planetesimals collision, which involve very different thermal history and astrophysical conditions (see review from Connolly and Jones[147] and references therein). The mechanism for chondrule formation

remains enigmatic, and addressing their origin is beyond the scope of this study.

The K/Rb fractionation, K and Rb depletions, $\delta^{41}K$ and $\delta^{87}Rb$ isotopic composition of HED meteorites are all important observations that any model of MVE depletion in Vesta must explain, and none of the models proposed thus far can readily account for these observations. Here, we take an agnostic approach with regard to the astronomical setting of K and Rb loss, and we investigate the temperature−saturation−size conditions under which the chemical and isotopic characteristics

of Vesta can be reproduced. We limit ourselves to evaporation from small bodies where advective transport inside liquid droplets is negligible. If advection takes place, our formalism can still be applied by using effective diffusivities that comprise an advective component and by reducing the β-exponent to account for such transport.

As discussed by Toplis et al.,[148] H-chondrites provide the best model composition for bulk Vesta and we use their compositions to quantify the degree of K depletion ($0.058\times$ H-chondrite[68]) and K/Rb fractionation ($6\times$ H-chondrite[68]). We use estimates of the bulk silicate Earth to quantify $\delta^{41}K$ ($0.84\%o$ relative to BSE[52]) and $\delta^{87}Rb$ ($0.67-1.63\%o$ relative to BSE[66]) values in HED meteorites because available data for H chondrites show a lot of dispersion.[60]

The K/Rb, $\delta^{41}K$, and $\delta^{87}Rb$ values of the residues were calculated for 94% K lost (similar to the depletion seen in 4-Vesta relative to H chondrites) with an oxygen fugacity near the IW buffer. The redox condition applied here is estimated on the basis of highly fractionated Mn/Na ratios in HED meteorites, which are sensitive to fO_2 during evaporation.[149,150] In Figure 17A−D, we show the results assuming that evaporation took place under vacuum. As shown, at high temperature (>1200 °C), Rb has a similar volatility as K, resulting in a K/Rb weight ratio of less than 2. However, when the temperature is below 1100 °C, Rb tends to evaporate faster than K, resulting in an elevated K/Rb ratio that can explain the ratio measured in a HED meteorite of ∼6. The sphere size can also affect the K/Rb ratio. When evaporation becomes diffusion limited at higher temperature, the K/Rb ratio in the residue decreases because Rb diffuses more slowly than K due to its higher mass and larger ionic radius. This is the opposite of what is observed. The fractionated K/Rb ratio of $6\times$ H-chondrite in Vesta can be reproduced by evaporation of spherical objects spanning a wide range of sizes for temperatures around 1050 °C. A limitation of our calculation is that at this temperature the system would be partially crystallized, which would have several effects. It would enrich the residual melt in alkali elements, thereby increasing their evaporation rates. At the same time, the liquid SiO_2 and Al_2O_3 contents would also increase, resulting in a smaller NBO/T, thereby reducing evaporation rates.[32,151] Additionally, the crystalline phase could float at the surface, slowing down the evaporation. A combination of these effects could change the calculated evaporation rates and affect the calculated time scale shown in Figure 15D,H. Due to the lack of robust data to anchor the kinetics of evaporation at low T in subliquidus systems, we have decided not to take these complications into account in the present contribution.

An important issue with this free evaporation model is however that, under all conceivable conditions, the residue left after 94% loss of K has highly fractionated $\delta^{41}K$ ($69\%o$) and $\delta^{87}Rb$ ($46\%o$) values. The only way to reduce this fractionation during vacuum evaporation is if the rate-limiting step becomes diffusion in the melt at high temperature. This cannot however explain the elevated K/Rb ratio of Vesta, and another explanation must be sought.

As discussed by Richter et al.[36] and Dauphas et al.,[5] isotopic fractionation during evaporation can be dampened if the evaporation does not take place in the vacuum but rather in a partially saturated medium. The degree of isotopic fractionation in such a case is

$$\Delta_i^{v-l} = \Delta_{eq}^{v-l} + (1 - S_i)\Delta_{kin,i}^{v-l} \tag{89}$$

where S_i is the degree of undersaturation of the vapor species i ($S_i = 0$ for vacuum free evaporation). Δ_{eq}^{v-l} is the equilibrium isotope fractionation between vapor and melt, which is estimated using ab initio data from Zeng et al.[46] $\Delta_{kin,i}^{v-l}$ is the kinetic isotope fractionation expressed as ν_j/ν_i in eq 28. The results of Tian et al.[52] on K isotopic fractionation in HED meteorites ($0.84\%o$ relative to BSE) can be explained with an S value of 0.988 if evaporation is nondiffusion limited. We therefore modeled the evaporation kinetic at a saturation degree of 0.988, which yields a calculated $\delta^{87}Rb$ value of ∼$0.6\%o$. There are only two data points for $\delta^{85}Rb$ in HED meteorites, which span a large range from $0.67\%o$ and $1.63\%o$.[66] More measurements are needed to better constrain the bulk Rb isotopic composition of HED meteorites (Vesta), but the modeled fractionation is consistent with the available data.

If K and Rb are lost in such saturated medium, this would dramatically affect the kinetics of evaporation as the evaporation flux becomes

$$J_i = \frac{n_i\gamma_i(P_{i,eq} - P_i)}{\sqrt{2\pi M_i RT}} = \frac{n_i\gamma_i(1 - S_i)P_{i,eq}}{\sqrt{2\pi M_i RT}} \tag{90}$$

We calculated the time scale for reaching 94% depletion of K under such conditions, which is shown in Figure 17D, H. The elevated K/Rb ratio of Vesta requires evaporation to take place at a relatively low temperature of 1050 °C. At a saturation level of 0.988 and this temperature, the time required to evaporate 94% of K is 0.1 to 10 years depending on the sphere radius. The evaporation from droplet-size objects can account for the depletions in K and Rb and the elevated K/Rb ratio of Vesta. The calculated time scale is larger than the heating time scales invoked for chondrules of ∼10^{-3} years,[124,152] so the setting for this evaporation would have been very different compared to chondrule formation. Specifically, it would have involved prolonged heating in a medium that maintained near saturation conditions.

6. CONCLUSIONS

We have performed vacuum evaporation experiments of the alkali elements Na, K, and Rb from a synthetic basalt composition at 1200 and 1400 °C. We measured (i) the degree of loss of Na, K, and Rb in the experimental run products, (ii) chemical concentration profiles for all the residues, (iii) Fe redox states by Mössbauer, (iv) $\delta^{41}K$ in situ by SIMS, and (v) $\delta^{87}Rb$ in bulk residues by MC-ICPMS. We find that the residues from the 1200 °C experiments have uniform chemical and $\delta^{41}K$ isotopic compositions, whereas those at 1400 °C show clear chemical and isotopic zoning. The reason for this zoning is diffusion-limited evaporation at the higher temperatures. We have derived analytical equations that allow us to calculate how diffusive transport affects the evaporation rate and isotopic fractionation. We find that the order of volatilities is Na > Rb > K for our experimental conditions. Equilibrium thermodynamics and previous studies are combined to quantify the product of activity and evaporation coefficients of Na, K, and Rb in silicate melts. Our K and Rb isotopic analyses show that the residues follow Rayleigh distillations consistent with the relative evaporation rates of the different isotopes of K and Rb being proportional to the square root ratio of their isotopic masses. These new insights are applied to understanding the origin of moderately volatile element depletion in Vesta. We conclude that the great depletion in K and Rb, the high fractionation K/Rb ratio, and elevated $\delta^{41}K$ and $\delta^{87}Rb$ values of Vesta can be

explained as the result of protracted (0.1−10 yr) evaporation in a near-saturated (98.8%) medium at a low temperature of droplet-size objects. More work is however needed to ascertain this conclusion and test whether temperature is the main driver behind K/Rb fractionation in Vesta.

■ ASSOCIATED CONTENT

ⓈⒾ Supporting Information

The Supporting Information is available free of charge at https://pubs.acs.org/doi/10.1021/acsearthspace-chem.0c00263.

> Theoretical derivation for the diffusion-limited evaporation; backscatter electron images; chemical composition analysis; Mössbauer spectra; Fe redox states; comparison of analytical and numerical methods for solving the differential equation for diffusion-limited evaporation in a sphere; physical properties of the sample residues; isotopic and elemental profiles, backscattered electron images, and Na, K, and Rb concentration profiles; measured elemental concentrations (PDF)

■ AUTHOR INFORMATION

Corresponding Author

Zhe J. Zhang − *Origins Laboratory and Department of the Geophysical Sciences and Enrico Fermi Institute, The University of Chicago, Chicago, Illinois 60637, United States;* ⓞ orcid.org/0000-0001-8323-7967; Email: zhez@uchicago.edu

Authors

Nicole Xike Nie − *Origins Laboratory and Department of the Geophysical Sciences and Enrico Fermi Institute, The University of Chicago, Chicago, Illinois 60637, United States; Earth & Planets Laboratory, Carnegie Institution for Science, Washington, D.C. 20015, United States*

Ruslan A. Mendybaev − *Department of the Geophysical Sciences and Enrico Fermi Institute, The University of Chicago, Chicago, Illinois 60637, United States*

Ming-Chang Liu − *Department of Earth, Planetary and Space Sciences, UCLA, Los Angeles, California 90095, United States*

Justin Jingya Hu − *Origins Laboratory and Department of the Geophysical Sciences and Enrico Fermi Institute, The University of Chicago, Chicago, Illinois 60637, United States*

Timo Hopp − *Origins Laboratory and Department of the Geophysical Sciences and Enrico Fermi Institute, The University of Chicago, Chicago, Illinois 60637, United States*

Esen E. Alp − *Advanced Photon Source, Argonne National Laboratory, Lemont, Illinois 60439, United States*

Barbara Lavina − *Advanced Photon Source, Argonne National Laboratory, Lemont, Illinois 60439, United States*

Emma S. Bullock − *Earth & Planets Laboratory, Carnegie Institution for Science, Washington, D.C. 20015, United States*

Kevin D. McKeegan − *Department of Earth, Planetary and Space Sciences, UCLA, Los Angeles, California 90095, United States*

Nicolas Dauphas − *Origins Laboratory and Department of the Geophysical Sciences and Enrico Fermi Institute, The University of Chicago, Chicago, Illinois 60637, United States*

Complete contact information is available at:

https://pubs.acs.org/10.1021/acsearthspacechem.0c00263

Author Contributions

∇N.X.N. and R.A.M. contributed equally to this work. Z.Z., N.X.N., N.D., and R.A.M. conceived the study. Z.Z., R.A.M., and N.X.N. conducted the evaporation experiments. N.Z.N. and Z.Z. measured the Rb isotopic composition. N.X.N. and E.S.B. performed the EMPA analyses. M.-C.L., Z.Z., and K.D.M. conducted the in situ K isotopic analyses. E.E.A. and B.L. performed the Mössbauer measurements. Z.Z., N.D., and J.J.H. modeled the evaporation kinetics and derived the equations for diffusion-limited evaporation. Z.Z. and N.D. simulated K and Rb evaporation from small planetary bodies. T.H. contributed to the discussion of K and Rb depletions in the planetary bodies. Z.Z. and N.D. wrote the first draft of the manuscript, which was subsequently edited by all coauthors.

Notes

The authors declare no competing financial interest.

■ ACKNOWLEDGMENTS

■ REFERENCES

(1) Wood, B. J.; Smythe, D. J.; Harrison, T. The condensation temperatures of the elements: A reappraisal. *Am. Mineral.* **2019**, *104* (6), 844−856.

(2) Lodders, K. Solar System Abundances and Condensation Temperatures of the Elements. *Astrophys. J.* **2003**, *591* (2), 1220−1247.

(3) Davis, A. M. Volatile evolution and loss. In *Meteorites and the early solar system II*; University of Arizona Press: Tucson, 2006; Vol. *1*, pp 295−307.

(4) Braukmüller, N.; Wombacher, F.; Hezel, D. C.; Escoube, R.; Münker, C. The chemical composition of carbonaceous chondrites: Implications for volatile element depletion, complementality and alteration. *Geochim. Cosmochim. Acta* **2018**, *239*, 17−48.

(5) Dauphas, N.; Poitrasson, F.; Burkhardt, C.; Kobayashi, H.; Kurosawa, K. Planetary and meteoritic Mg/Si and δ30Si variations inherited from solar nebula chemistry. *Earth Planet. Sci. Lett.* **2015**, *427*, 236−248.

(6) Cassen, P. Models for the fractionation of moderately volatile elements in the solar nebula. *Meteoritics & Planetary Science* **1996**, *31* (6), 793−806.

(7) Grossman, L. Condensation in the primitive solar nebula. *Geochim. Cosmochim. Acta* **1972**, *36* (5), 597−619.

(8) Grossman, L.; Larimer, J. W. Early chemical history of the solar system. *Rev. Geophys.* **1974**, *12* (1), 71−101.

(9) Cassen, P. Nebular thermal evolution and the properties of primitive planetary materials. *Meteorit. Planet. Sci.* **2001**, *36* (5), 671−700.

(10) Petaev, M. I.; Wood, J. A. The condensation with partial isolation (CWPI) model of condensation in the solar nebula. *Meteorit. Planet. Sci.* **1998**, *33* (5), 1123−1137.

(11) Ebel, D. S.; Grossman, L. Condensation in dust-enriched systems. *Geochim. Cosmochim. Acta* **2000**, *64* (2), 339−366.

(12) Humayun, M.; Cassen, P. Processes determining the volatile abundances of the meteorites and terrestrial planets. In *Origin of the Earth Moon*; University of Arizona Press: Tucson, 2000; pp 3−23.

(13) Morbidelli, A.; Libourel, G.; Palme, H.; Jacobson, S. A.; Rubie, D. C. Subsolar Al/Si and Mg/Si ratios of non-carbonaceous chondrites

reveal planetesimal formation during early condensation in the protoplanetary disk. *Earth Planet. Sci. Lett.* **2020**, *538*, 116220.

(14) Mittlefehldt, D. W. Volatile degassing of basaltic achondrite parent bodies: Evidence from alkali elements and phosphorus. *Geochim. Cosmochim. Acta* **1987**, *51* (2), 267−278.

(15) Charnoz, S.; Michaut, C. Evolution of the protolunar disk: Dynamics, cooling timescale and implantation of volatiles onto the Earth. *Icarus* **2015**, *260*, 440−463.

(16) Canup, R. M.; Visscher, C.; Salmon, J.; Fegley, B., Jr Lunar volatile depletion due to incomplete accretion within an impact-generated disk. *Nat. Geosci.* **2015**, *8* (12), 918−921.

(17) Nie, N. X.; Dauphas, N. Vapor Drainage in the Protolunar Disk as the Cause for the Depletion in Volatile Elements of the Moon. *Astrophys. J., Lett.* **2019**, *884* (2), L48.

(18) Lock, S. J.; Stewart, S. T.; Petaev, M. I.; Leinhardt, Z.; Mace, M. T.; Jacobsen, S. B.; Cuk, M. The Origin of the Moon Within a Terrestrial Synestia. *J. Geophys. Res.: Planets* **2018**, *123* (4), 910−951.

(19) Dhaliwal, J. K.; Day, J. M. D.; Moynier, F. Volatile element loss during planetary magma ocean phases. *Icarus* **2018**, *300*, 249−260.

(20) Hin, R. C.; Coath, C. D.; Carter, P. J.; Nimmo, F.; Lai, Y.-J.; von Strandmann, P. A. E. P.; Willbold, M.; Leinhardt, Z. M.; Walter, M. J.; Elliott, T. Magnesium isotope evidence that accretional vapour loss shapes planetary compositions. *Nature* **2017**, *549* (7673), 511−515.

(21) Halliday, A. N.; Porcelli, D. In search of lost planets − the paleocosmochemistry of the inner solar system. *Earth Planet. Sci. Lett.* **2001**, *192* (4), 545−559.

(22) Norris, C. A.; Wood, B. J. Earth's volatile contents established by melting and vaporization. *Nature* **2017**, *549* (7673), 507−510.

(23) Tera, F.; Eugster, O.; Burnett, D. S.; Wasserburg, G. J. Comparative study of Li, Na, K, Rb, Cs, Ca, Sr and Ba abundances in achondrites and in Apollo 11 lunar samples. *Proceedings of the Apollo 11 Lunar Science Conference.* 1970; Vol. 2, pp 1637−1657,

(24) McDonough, W. F.; Sun, S. S.; Ringwood, A. E.; Jagoutz, E.; Hofmann, A. W. Potassium, rubidium, and cesium in the Earth and Moon and the evolution of the mantle of the Earth. *Geochim. Cosmochim. Acta* **1992**, *56* (3), 1001−1012.

(25) Wasson, J. T.; Chou, C. L. Fractionation of moderately volatile elements in ordinary chondrites. *Meteoritics* **1974**, *9* (1), 69−84.

(26) Yu, Y.; Hewins, R. H.; Wang, J. Experimental study of evaporation and isotopic mass fractionation of potassium in silicate melts. *Geochim. Cosmochim. Acta* **2003**, *67* (4), 773−786.

(27) Richter, F. M.; Mendybaev, R. A.; Christensen, J. N.; Ebel, D.; Gaffney, A. Laboratory experiments bearing on the origin and evolution of olivine-rich chondrules. *Meteoritics & Planetary Science* **2011**, *46* (8), 1152−1178.

(28) Shimaoka, T. K.; Miyano, N.; Baba, T.; Yamamoto, K.; Nakamura, N. Volatilization of alkali metals from the heated Murchison (CM2) meteorite. *Proc. NIPR Symp. Antarct. Meteorites* **1994**, *7*, 164−177.

(29) Sossi, P. A.; Klemme, S.; O'Neill, H. S. C.; Berndt, J.; Moynier, F. Evaporation of moderately volatile elements from silicate melts: experiments and theory. *Geochim. Cosmochim. Acta* **2019**, *260*, 204−231.

(30) Gibson, E. K.; Hubbard, N. J. Thermal volatilization studies on lunar samples. In *Proceedings of the Third Lunar Science Conference*, Houston, Texas, January 10−13, 1972; p 2003.

(31) Gibson, E. K.; Hubbard, N. J.; Wiesmann, H.; Bansal, B. M.; Moore, G. W. How to lose Rb, K, and change the K/Rb ratio: An experimental study. In *Proceedings of the Lunar Science Conference*, Houston, Texas, 1973; Vol. 4, pp 1263−1273.

(32) Gellissen, M.; Holzheid, A.; Kegler, P.; Palme, H. Heating experiments relevant to the depletion of Na, K and Mn in the Earth and other planetary bodies. *Chem. Erde* **2019**, *79* (4), 125540.

(33) Kreutzberger, M. E.; Drake, M. J.; Jones, J. H. Origin of the Earth's Moon: Constraints from alkali volatile trace elements. *Geochim. Cosmochim. Acta* **1986**, *50* (1), 91−98.

(34) Tsuchiyama, A.; Nagahara, H.; Kushiro, I. Volatilization of sodium from silicate melt spheres and its application to the formation of chondrules. *Geochim. Cosmochim. Acta* **1981**, *45* (8), 1357−1367.

(35) Richter, F. M. Timescales determining the degree of kinetic isotope fractionation by evaporation and condensation. *Geochim. Cosmochim. Acta* **2004**, *68* (23), 4971−4992.

(36) Richter, F. M.; Davis, A. M.; Ebel, D. S.; Hashimoto, A. Elemental and isotopic fractionation of Type B calcium-, aluminum-rich inclusions: experiments, theoretical considerations, and constraints on their thermal evolution. *Geochim. Cosmochim. Acta* **2002**, *66* (3), 521−540.

(37) Bourdon, B.; Fitoussi, C. Isotope Fractionation during Condensation and Evaporation during Planet Formation Processes. *ACS Earth and Space Chemistry* **2020**, *4* (8), 1408−1423.

(38) Wang, K.; Jacobsen, S. B. Potassium isotopic evidence for a high-energy giant impact origin of the Moon. *Nature* **2016**, *538* (7626), 487−490.

(39) Li, S.; Li, W.; Beard, B. L.; Raymo, M. E.; Wang, X.; Chen, Y.; Chen, J. K isotopes as a tracer for continental weathering and geological K cycling. *Proc. Natl. Acad. Sci. U. S. A.* **2019**, *116* (18), 8740−8745.

(40) Tuller-Ross, B.; Marty, B.; Chen, H.; Kelley, K. A.; Lee, H.; Wang, K. Potassium isotope systematics of oceanic basalts. *Geochim. Cosmochim. Acta* **2019**, *259*, 144−154.

(41) Santiago Ramos, D. P.; Morgan, L. E.; Lloyd, N. S.; Higgins, J. A. Reverse weathering in marine sediments and the geochemical cycle of potassium in seawater: Insights from the K isotopic composition (41K/39K) of deep-sea pore-fluids. *Geochim. Cosmochim. Acta* **2018**, *236*, 99−120.

(42) Parendo, C. A.; Jacobsen, S. B.; Wang, K. K isotopes as a tracer of seafloor hydrothermal alteration. *Proc. Natl. Acad. Sci. U. S. A.* **2017**, *114* (8), 1827−1831.

(43) Humayun, M.; Clayton, R. N. Potassium isotope cosmochemistry: Genetic implications of volatile element depletion. *Geochim. Cosmochim. Acta* **1995**, *59* (10), 2131−2148.

(44) Humayun, M.; Clayton, R. N. Precise determination of the isotopic composition of potassium: Application to terrestrial rocks and lunar soils. *Geochim. Cosmochim. Acta* **1995**, *59* (10), 2115−2130.

(45) Taylor, S.; Delaney, J.; Ma, P.; Herzog, G. F.; Engrand, C. Isotopic fractionation of iron, potassium, and oxygen in stony cosmic spherules: Implications for heating histories and sources. *Geochim. Cosmochim. Acta* **2005**, *69* (10), 2647−2662.

(46) Zeng, H.; Rozsa, V. F.; Nie, N. X.; Zhang, Z.; Pham, T. A.; Galli, G.; Dauphas, N. Ab Initio Calculation of Equilibrium Isotopic Fractionations of Potassium and Rubidium in Minerals and Water. *ACS Earth Space Chemistry* **2019**, *3* (11), 2601−2612.

(47) Teng, F.-Z.; Hu, Y.; Ma, J.-L.; Wei, G.-J.; Rudnick, R. L. Potassium isotope fractionation during continental weathering and implications for global K isotopic balance. *Geochim. Cosmochim. Acta* **2020**, *278*, 261.

(48) Liu, H.; Wang, K.; Sun, W.-D.; Xiao, Y.; Xue, Y.-Y.; Tuller-Ross, B. Extremely light K in subducted low-T altered oceanic crust: Implications for K recycling in subduction zone. *Geochim. Cosmochim. Acta* **2020**, *277*, 206.

(49) Huang, T.-Y.; Teng, F.-Z.; Rudnick, R. L.; Chen, X.-Y.; Hu, Y.; Liu, Y.-S.; Wu, F.-Y. Heterogeneous potassium isotopic composition of the upper continental crust. *Geochim. Cosmochim. Acta* **2020**, *278*, 122−136.

(50) Santiago Ramos, D. P.; Coogan, L. A.; Murphy, J. G.; Higgins, J. A. Low-temperature oceanic crust alteration and the isotopic budgets of potassium and magnesium in seawater. *Earth Planet. Sci. Lett.* **2020**, *541*, 116290.

(51) Tian, Z.; Jolliff, B. L.; Korotev, R. L.; Fegley, B.; Lodders, K.; Day, J. M. D.; Chen, H.; Wang, K. Potassium isotopic composition of the Moon. *Geochim. Cosmochim. Acta* **2020**, *280*, 263.

(52) Tian, Z.; Chen, H.; Fegley, B., Jr.; Lodders, K.; Barrat, J.-A.; Day, J. M. D.; Wang, K. Potassium isotopic compositions of howardite-eucrite-diogenite meteorites. *Geochim. Cosmochim. Acta* **2019**, *266*, 611−632.

(53) Sun, Y.; Teng, F.-Z.; Hu, Y.; Chen, X.-Y.; Pang, K.-N. Tracing subducted oceanic slabs in the mantle by using potassium isotopes. *Geochim. Cosmochim. Acta* **2020**, *278*, 353.

(54) Chen, H.; Liu, X.-M.; Wang, K. Potassium isotope fractionation during chemical weathering of basalts. *Earth Planet. Sci. Lett.* **2020**, *539*, 116192.

(55) Herzog, G. F.; Alexander, C. M. O. D.; Berger, E. L.; Delaney, J. S.; Glass, B. P. Potassium isotope abundances in Australasian tektites and microtektites. *Meteorit. Planet. Sci.* **2008**, *43* (10), 1641−1657.

(56) Li, W.; Kwon, K. D.; Li, S.; Beard, B. L. Potassium isotope fractionation between K-salts and saturated aqueous solutions at room temperature: Laboratory experiments and theoretical calculations. *Geochim. Cosmochim. Acta* **2017**, *214*, 1−13.

(57) Chen, H.; Meshik, A. P.; Pravdivtseva, O. V.; Day, J. M. D.; Wang, K. Potassium isotope fractionation during high-temperature evaporation determined from the Trinity nuclear test. *Chem. Geol.* **2019**, *522*, 84−92.

(58) Wang, K.; Close, H. G.; Tuller-Ross, B.; Chen, H. Global Average Potassium Isotope Composition of Modern Seawater. *ACS Earth and Space Chemistry* **2020**, *4*, 1010.

(59) Zhao, C.; Lodders, K.; Bloom, H.; Chen, H.; Tian, Z.; Koefoed, P.; Pető, M. K.; Wang, K. Potassium isotopic compositions of enstatite meteorites. *Meteorit. Planet. Sci.* **2020**, *55*, 1404.

(60) Bloom, H.; Lodders, K.; Chen, H.; Zhao, C.; Tian, Z.; Koefoed, P.; Pető, M. K.; Jiang, Y.; Wang, K. Potassium isotope compositions of carbonaceous and ordinary chondrites: implications on the origin of volatile depletion in the early solar system. *Geochim. Cosmochim. Acta* **2020**, *277*, 111.

(61) Li, Y.; Wang, W.; Wu, Z.; Huang, S. First-principles investigation of equilibrium K isotope fractionation among K-bearing minerals. *Geochim. Cosmochim. Acta* **2019**, *264*, 30−42.

(62) Alexander, C. M. O. D.; Grossman, J. N. Alkali elemental and potassium isotopic compositions of Semarkona chondrules. *Meteorit. Planet. Sci.* **2005**, *40* (4), 541−556.

(63) Jiang, Y.; Chen, H.; Fegley, B.; Lodders, K.; Hsu, W.; Jacobsen, S. B.; Wang, K. Implications of K, Cu and Zn isotopes for the formation of tektites. *Geochim. Cosmochim. Acta* **2019**, *259*, 170−187.

(64) Hu, Y.; Teng, F.-Z.; Plank, T.; Chauvel, C. Potassium isotopic heterogeneity in subducting oceanic plates. *Science Advances* **2020**, *6* (49), eabb2472.

(65) Wang, K.; Peucker-Ehrenbrink, B.; Chen, H.; Lee, H.; Hasenmueller, E. A. Dissolved potassium isotopic composition of major world rivers. *Geochim. Cosmochim. Acta* **2021**, *294*, 145−159.

(66) Pringle, E. A.; Moynier, F. Rubidium isotopic composition of the Earth, meteorites, and the Moon: Evidence for the origin of volatile loss during planetary accretion. *Earth Planet. Sci. Lett.* **2017**, *473*, 62−70.

(67) Nebel, O.; Mezger, K.; van Westrenen, W. Rubidium isotopes in primitive chondrites: Constraints on Earth's volatile element depletion and lead isotope evolution. *Earth Planet. Sci. Lett.* **2011**, *305* (3−4), 309−316.

(68) Kitts, K.; Lodders, K. Survey and evaluation of eucrite bulk compositions. *Meteorit. Planet. Sci.* **1998**, *33* (S4), A197−A213.

(69) Dauphas, N.; Janney, P. E.; Mendybaev, R. A.; Wadhwa, M.; Richter, F. M.; Davis, A. M.; van Zuilen, M.; Hines, R.; Foley, C. N. Chromatographic Separation and Multicollection-ICPMS Analysis of Iron. Investigating Mass-Dependent and -Independent Isotope Effects. *Anal. Chem.* **2004**, *76* (19), 5855−5863.

(70) Davis, A. M.; Hashimoto, A.; Clayton, R. N.; Mayeda, T. K. Isotope mass fractionation during evaporation of Mg 2 Si0 4. *Nature* **1990**, *347* (6294), 655−658.

(71) Wang, J.; Davis, A. M.; Clayton, R. N.; Hashimoto, A. Evaporation of single crystal forsterite: Evaporation kinetics, magnesium isotope fractionation, and implications of mass-dependent isotopic fractionation of a diffusion-controlled reservoir. *Geochim. Cosmochim. Acta* **1999**, *63* (6), 953−966.

(72) Tsuchiyama, A.; Tachibana, S.; Takahashi, T. Evaporation of forsterite in the primordial solar nebula; rates and accompanied isotopic fractionation. *Geochim. Cosmochim. Acta* **1999**, *63* (16), 2451−2466.

(73) Kendall, B. R. F. Isotopic composition of potassium. *Nature* **1960**, *186* (4720), 225−226.

(74) Garner, E. L.; Machlan, L. A.; Barnes, I. L. The isotopic composition of lithium, potassium, and rubidium in some Apollo 11, 12, 14, 15, and 16 samples. In *Proceedings of the Sixth Lunar Science Conference*, Houston, Texas, March 17−21, 1975; pp 1845−1855.

(75) Humayun, M.; Koeberl, C. Potassium isotopic composition of Australasian tektites. *Meteorit. Planet. Sci.* **2004**, *39* (9), 1509−1516.

(76) Church, S. E.; Tilton, G. R.; Wright, J. E.; Lee-Hu, C. N. Volatile element depletion and K-39/K-41 fractionation in lunar soils. In *Proceedings of the Seventh Lunar Science Conference*, Houston, Texas, March 15−19, 1976; pp423−439.

(77) Wulf, A. V.; Palme, H.; Jochum, K. P. Fractionation of volatile elements in the early solar system: evidence from heating experiments on primitive meteorites. *Planet. Space Sci.* **1995**, *43* (3−4), 451−468.

(78) Young, E. D.; Nagahara, H.; Mysen, B. O.; Audet, D. M. Non-Rayleigh oxygen isotope fractionation by mineral evaporation: theory and experiments in the system SiO2. *Geochim. Cosmochim. Acta* **1998**, *62* (18), 3109−3116.

(79) Galy, A.; Young, E. D.; Ash, R. D.; Keith, O.; Nions, R. The Formation of Chondrules at High Gas Pressures in the Solar Nebula. *Science* **2000**, *290* (5497), 1751.

(80) Ozawa, K.; Nagahara, H. Chemical and isotopic fractionations by evaporation and their cosmochemical implications. *Geochim. Cosmochim. Acta* **2001**, *65* (13), 2171−2199.

(81) Sossi, P. A.; Moynier, F.; Treilles, R.; Mokhtari, M.; Wang, X.; Siebert, J. An experimentally-determined general formalism for evaporation and isotope fractionation of Cu and Zn from silicate melts between 1300 - 1500 °C and 1 bar. *Geochim. Cosmochim. Acta* **2020**, *288*, 316.

(82) Gale, A.; Dalton, C. A.; Langmuir, C. H.; Su, Y.; Schilling, J.-G. The mean composition of ocean ridge basalts. *Geochem., Geophys., Geosyst.* **2013**, *14* (3), 489−518.

(83) Mendybaev, R. A.; Beckett, J. R.; Stolper, E.; Grossman, L. Measurement of oxygen fugacities under reducing conditions: Non-Nernstian behavior of Y2O3-doped zirconia oxygen sensors. *Geochim. Cosmochim. Acta* **1998**, *62* (18), 3131−3139.

(84) Asimow, P. D.; Ghiorso, M. S. Algorithmic modifications extending MELTS to calculate subsolidus phase relations. *Am. Mineral.* **1998**, *83* (9−10), 1127−1132.

(85) Ghiorso, M. S.; Sack, R. O. Chemical mass transfer in magmatic processes IV. A revised and internally consistent thermodynamic model for the interpolation and extrapolation of liquid-solid equilibria in magmatic systems at elevated temperatures and pressures. *Contrib. Mineral. Petrol.* **1995**, *119* (2−3), 197−212.

(86) Hashimoto, A. Evaporation kinetics of forsterite and implications for the early solar nebula. *Nature* **1990**, *347* (6288), 53−55.

(87) Knight, K. B.; Kita, N. T.; Mendybaev, R. A.; Richter, F. M.; Davis, A. M.; Valley, J. W. Silicon isotopic fractionation of CAI-like vacuum evaporation residues. *Geochim. Cosmochim. Acta* **2009**, *73* (20), 6390−6401.

(88) Mendybaev, R. A.; Richter, F. M.; Georg, R. B.; Janney, P. E.; Spicuzza, M. J.; Davis, A. M.; Valley, J. W. Experimental evaporation of Mg-and Si-rich melts: implications for the origin and evolution of FUN CAIs. *Geochim. Cosmochim. Acta* **2013**, *123*, 368−384.

(89) Mendybaev, R. A.; Williams, C. D.; Spicuzza, M. J.; Richter, F. M.; Valley, J. W.; Fedkin, A. V.; Wadhwa, M. Thermal and chemical evolution in the early Solar System as recorded by FUN CAIs: Part II−Laboratory evaporation of potential CMS-1 precursor material. *Geochim. Cosmochim. Acta* **2017**, *201*, 49−64.

(90) Zhang, J.; Huang, S.; Davis, A. M.; Dauphas, N.; Hashimoto, A.; Jacobsen, S. B. Calcium and titanium isotopic fractionations during evaporation. *Geochim. Cosmochim. Acta* **2014**, *140*, 365−380.

(91) Richter, F. M.; Janney, P. E.; Mendybaev, R. A.; Davis, A. M.; Wadhwa, M. Elemental and isotopic fractionation of Type B CAI-like liquids by evaporation. *Geochim. Cosmochim. Acta* **2007**, *71* (22), 5544−5564.

(92) Mendybaev, R. A.; Kamibayashi, M.; Teng, F.-Z.; Savage, P. S.; Georg, R. B.; Richter, F. M.; Tachibana, S. Experiments quantifying elemental and isotopic fractionations during evaporation of CAI-like melts in low-pressure hydrogen and in vacuum: Constraints on thermal processing of CAIs in the protoplanetary disk. *Geochim. Cosmochim. Acta* **2021**, *292*, 557−576.

(93) Hertz, H. Ueber den Druck des gesättigten Quecksilberdampfes. *Ann. Phys.* **1882**, *253* (10), 193−200.

(94) Knudsen, M. Die Gesetze der Molekularströmung und der inneren Reibungsströmung der Gase durch Röhren. *Ann. Phys.* **1909**, *333* (1), 75−130.

(95) Langmuir, I. The evaporation, condensation and reflection of molecules and the mechanism of adsorption. *Phys. Rev.* **1916**, *8* (2), 149.

(96) Ryś, M. *Investigation of thermodynamic properties of alkali metals in oxide systems relevant to coal slags.* Ph.D. dissertation, Rheinisch-Westfälischen Technischen Hochschule Aachen, Aachen, Germany, 2007.

(97) De Maria, G.; Piacente, V. Vaporization Study of Selected Lunar Samples. In *Lunar and Planetary Science Conference*, Houston, Texas, March 5−8, 1973.

(98) Fraser, D.; Rammensee, W. Determination of the mixing properties of granitic and other aluminosilicate melts by Knudsen cell mass spectrometry. In *Magmatic Processes: Physicochemical Principles*; Geochemical Society: University Park, PA, 1987; pp 401−410.

(99) Lopatin, S. I.; Shugurov, S. M.; Stolyarova, V. L. Thermodynamic properties of silicate glasses and melts. III. The Rb2O-B2O3-SiO2 system. *Russ. J. Gen. Chem.* **2007**, *77* (3), 997−1001.

(100) Visscher, C.; Fegley, B. Chemistry of impact-generated silicate melt-vapor debris disks. *Astrophys. J., Lett.* **2013**, *767* (1), L12.

(101) Fedkin, A. V.; Grossman, L.; Ghiorso, M. S. Vapor pressures and evaporation coefficients for melts of ferromagnesian chondrule-like compositions. *Geochim. Cosmochim. Acta* **2006**, *70* (1), 206−223.

(102) Jacobson, N.; Ingersoll, N.; Myers, D. Vaporization coefficients of SiO2 and MgO. *J. Eur. Ceram. Soc.* **2017**, *37* (5), 2245−2252.

(103) Ogasawara, Y.; Hadi, T. S.; Maeda, M. Rates of evaporation in a vacuum in liquid Ni−Ti alloys. *ISIJ Int.* **1998**, *38* (8), 789−793.

(104) Smith, P.; Ward, R. G. The evaporation of liquid iron alloys under vacuum. *Can. Metall. Q.* **1966**, *5* (2), 77−92.

(105) Safarian, J.; Engh, T. A. Vacuum evaporation of pure metals. *Metall. Mater. Trans. A* **2013**, *44* (2), 747−753.

(106) Mendybaev, R. A.; Shornikov, S. I.; Jacobson, N. S.; Kowalski, B. Thermodynamics and Evaporation Kinetics of CAI-Like Melts. In *51st Lunar and Planetary Science Conference*, March 16−20, 2020; abstract no. 2168.

(107) Kohlweiler, E. Anreicherung der leichteren Isotopen des Jods. *Z. Phys. Chem.* **1920**, *95U* (1), 95−125.

(108) Mulliken, R. S.; Harkins, W. D. The separation of isotopes. Theory of resolution of isotopic mixtures by diffusion and similar processes. Experimental separation of mercury by evaporation in a vacuum. *J. Am. Chem. Soc.* **1922**, *44* (1), 37−65.

(109) Ludwig, K. R. *User's Manual for Isoplot 3.00: A Geochronological Toolkit for Microsoft Excel*; Berkeley Geochronology Center Special Publication; 2003; No. 4, p 70.

(110) McIntyre, G. A.; Brooks, C.; Compston, W.; Turek, A. The statistical assessment of Rb-Sr isochrons. *Journal of Geophysical Research* **1966**, *71* (22), 5459−5468.

(111) Young, E. D. Assessing the implications of K isotope cosmochemistry for evaporation in the preplanetary solar nebula. *Earth Planet. Sci. Lett.* **2000**, *183* (1), 321−333.

(112) Crank, J. *The mathematics of diffusion*; Oxford University Press: Oxford, 1979.

(113) Hashimoto, A. Evaporation metamorphism in the early solar nebula - evaporation experiments on the melt FeO-MgO-SiO$_2$-CaO-Al$_2$O$_3$ and chemical fractionations of primitive materials. *Geochem. J.* **1983**, *17* (3), 111−145.

(114) Richter, F. M.; Liang, Y.; Minarik, W. G. Multicomponent diffusion and convection in molten MgO-Al2O3-SiO2. *Geochim. Cosmochim. Acta* **1998**, *62* (11), 1985−1991.

(115) Bearman, R. J.; Jolly, D. L. Mass dependence of the self diffusion coefficients in two equimolar binary liquid Lennard-Jones systems determined through molecular dynamics simulation. *Mol. Phys.* **1981**, *44* (3), 665−675.

(116) Watkins, J. M.; DePaolo, D. J.; Watson, E. B. Kinetic fractionation of non-traditional stable isotopes by diffusion and crystal growth reactions. *Rev. Mineral. Geochem.* **2017**, *82* (1), 85−125.

(117) Richter, F. M.; Davis, A. M.; DePaolo, D. J.; Watson, E. B. Isotope fractionation by chemical diffusion between molten basalt and rhyolite. *Geochim. Cosmochim. Acta* **2003**, *67* (20), 3905−3923.

(118) Zhang, Y.; Ni, H.; Chen, Y. Diffusion data in silicate melts. *Rev. Mineral. Geochem.* **2010**, *72* (1), 311−408.

(119) Ni, H. Compositional dependence of alkali diffusivity in silicate melts: Mixed alkali effect and pseudo-alkali effect. *Am. Mineral.* **2012**, *97* (1), 70−79.

(120) Mungall, J. E. Empirical models relating viscosity and tracer diffusion in magmatic silicate melts. *Geochim. Cosmochim. Acta* **2002**, *66* (1), 125−143.

(121) Alexander, C. M. O. D. Application of MELTS to kinetic evaporation models of FeO-bearing silicate melts. *Meteorit. Planet. Sci.* **2002**, *37* (2), 245−256.

(122) Alexander, C. M. O. D. Exploration of quantitative kinetic models for the evaporation of silicate melts in vacuum and in hydrogen. *Meteorit. Planet. Sci.* **2001**, *36* (2), 255−283.

(123) Berman, R. G. Internally-consistent thermodynamic data for minerals in the system Na2O-K2O-CaO-MgO-FeO-Fe2O3-Al2O3-SiO2-TiO2-H2O-CO2. *J. Petrol.* **1988**, *29* (2), 445−522.

(124) Fedkin, A. V.; Grossman, L.; Ciesla, F. J.; Simon, S. B. Mineralogical and isotopic constraints on chondrule formation from shock wave thermal histories. *Geochim. Cosmochim. Acta* **2012**, *87*, 81−116.

(125) De Maria, G.; Balducci, G.; Guido, M.; Piacente, V. Mass spectrometric investigation of the vaporization process of Apollo 12 lunar samples. In *Proceedings of the Second Lunar Science Conference*, January 11−14, 1971; Vol. 2, p 1367.

(126) Chastel, R.; Bergman, C.; Rogez, J.; Mathieu, J. C. Excess thermodynamic functions in ternary Na2O— K2O— SiO2 melts by Knudsen cell mass spectrometry. *Chem. Geol.* **1987**, *62* (1−2), 19−29.

(127) Rammensee, W.; Fraser, D. G. Determination of activities in silicate melts by Knudsen cell mass spectrometry—I. The system NaAlSi$_3$O$_8$-KAlSi$_3$O$_8$. *Geochim. Cosmochim. Acta* **1982**, *46* (11), 2269−2278.

(128) Chase, M. W., Jr. *NIST-JANAF thermochemical tables*, Fourth ed.; American Chemical Society; American Institute of Physics for the National Institute of Standards and Technology: Washington, DC; New York, 1998.

(129) Borisov, A. A. Influence of SiO2 and Al2O3 on the activity coefficients of alkalis in melts: An experimental study. *Petrology* **2009**, *17* (6), 579−590.

(130) Wu, P.; Eriksson, G.; Pelton, A. D. Optimization of the thermodynamic properties and phase diagrams of the Na2O−SiO2 and K2O−SiO2 systems. *J. Am. Ceram. Soc.* **1993**, *76* (8), 2059−2064.

(131) Gaillard, F.; Schmidt, B.; Mackwell, S.; McCammon, C. Rate of hydrogen−iron redox exchange in silicate melts and glasses. *Geochim. Cosmochim. Acta* **2003**, *67* (13), 2427−2441.

(132) Dunn, T. Oxygen diffusion in three silicate melts along the join diopside-anorthite. *Geochim. Cosmochim. Acta* **1982**, *46* (11), 2293−2299.

(133) Wendlandt, R. F. Oxygen diffusion in basalt and andesite melts: experimental results and discussion of chemical versus tracer diffusion. *Contrib. Mineral. Petrol.* **1991**, *108* (4), 463−471.

(134) Knacke, O.; Kubaschewski, O.; Hesselmann, K. *Thermochemical Properties of Inorganic Substances*, 2nd ed.; Springer, 1991.

(135) Smales, A. A.; Hughes, T. C.; Mapper, D.; McInnes, C. A. J.; Webster, R. K. The determination of rubidium and caesium in stony meteorites by neutron activation analysis and by mass spectrometry. *Geochim. Cosmochim. Acta* **1964**, *28* (2), 209−233.

(136) Lodders, K. Retention of alkali elements during planetary accretion and differentiation. *Meteoritics* **1994**, *29*, 492−493.

(137) Sossi, P. A.; Fegley, B. Thermodynamics of element volatility and its application to planetary processes. *Rev. Mineral. Geochem.* **2018**, *84* (1), 393−459.

(138) Young, E. D.; Shahar, A.; Nimmo, F.; Schlichting, H. E.; Schauble, E. A.; Tang, H.; Labidi, J. Near-equilibrium isotope fractionation during planetesimal evaporation. *Icarus* **2019**, *323*, 1−15.

(139) Morgan, J. W.; Higuchi, H.; Takahashi, H.; Hertogen, J. A "chondritic" eucrite parent body: inference from trace elements. *Geochim. Cosmochim. Acta* **1978**, *42* (1), 27−38.

(140) Alexander, C. M. O. D.; Grossman, J. N.; Wang, J.; Zanda, B.; Bourot-Denise, M.; Hewins, R. H. The lack of potassium-isotopic fractionation in Bishunpur chondrules. *Meteoritics & Planetary Science* **2000**, *35* (4), 859−868.

(141) Koefoed, P.; Pravdivtseva, O.; Chen, H.; Gerritzen, C.; Thiemens, M. M.; Wang, K. Potassium isotope systematics of the LL4 chondrite Hamlet: Implications for chondrule formation and alteration. *Meteorit. Planet. Sci.* **2020**, *55*, 1.

(142) Jiang, Y.; Koefoed, P.; Pravdivtseva, O.; Chen, H.; Li, C.-H.; Huang, F.; Qin, L.-P.; Liu, J.; Wang, K. Early solar system aqueous activity: K isotope evidence from Allende. *Meteorit. Planet. Sci.* **2020**; DOI: 10.1111/maps.13588.

(143) Matsuda, H.; Nakamura, N.; Noda, S. Alkali (Rb/K) abundances in Allende barred-olivine chondrules: Implications for the melting conditions of chondrules. *Meteoritics* **1990**, *25* (2), 137−143.

(144) Alexander, C. M. O. D. Trace element contents of chondrule rims and interchondrule matrix in ordinary chondrites. *Geochim. Cosmochim. Acta* **1995**, *59* (15), 3247−3266.

(145) Schaefer, L.; Fegley, B. A thermodynamic model of high temperature lava vaporization on Io. *Icarus* **2004**, *169* (1), 216−241.

(146) Sarafian, A. R.; John, T.; Roszjar, J.; Whitehouse, M. J. Chlorine and hydrogen degassing in Vesta's magma ocean. *Earth Planet. Sci. Lett.* **2017**, *459*, 311−319.

(147) Connolly, H. C.; Jones, R. H. Chondrules: The canonical and noncanonical views. *Journal of Geophysical Research: Planets* **2016**, *121* (10), 1885−1899.

(148) Toplis, M. J.; Mizzon, H.; Monnereau, M.; Forni, O.; McSween, H. Y.; Mittlefehldt, D. W.; McCoy, T. J.; Prettyman, T. H.; De Sanctis, M. C.; Raymond, C. A. Chondritic models of 4 Vesta: Implications for geochemical and geophysical properties. *Meteoritics & Planetary Science* **2013**, *48* (11), 2300−2315.

(149) Mahan, B.; Moynier, F.; Siebert, J.; Gueguen, B.; Agranier, A.; Pringle, E. A.; Bollard, J.; Connelly, J. N.; Bizzarro, M. Volatile element evolution of chondrules through time. *Proc. Natl. Acad. Sci. U. S. A.* **2018**, *115* (34), 8547−8552.

(150) O'Neill, H. S. C.; Palme, H. Collisional erosion and the non-chondritic composition of the terrestrial planets. *Philos. Trans. R. Soc., A* **2008**, *366* (1883), 4205−4238.

(151) Collinet, M.; Grove, T. L. Formation of primitive achondrites by partial melting of alkali-undepleted planetesimals in the inner solar system. *Geochim. Cosmochim. Acta* **2020**, *277*, 358.

(152) Ciesla, F. J.; Hood, L. L. The Nebular Shock Wave Model for Chondrule Formation: Shock Processing in a Particle−Gas Suspension. *Icarus* **2002**, *158* (2), 281−293.

(153) Lundstrom, C. C. An experimental investigation of the diffusive infiltration of alkalis into partially molten peridotite: Implications for mantle melting processes. *Geochem., Geophys., Geosyst.* **2003**, *4* (9), 1.

(154) Koepke, J.; Behrens, H. Trace element diffusion in andesitic melts: An application of synchrotron X-ray fluorescence analysis. *Geochim. Cosmochim. Acta* **2001**, *65* (9), 1481−1498.